Hygrothermal Effects on Fracture Toughness of Flax Fiber Reinforced Epoxy

Master's Thesis Report

Luca Alexander Baak

Faculty of Aerospace Engineering - Delft University of Technology

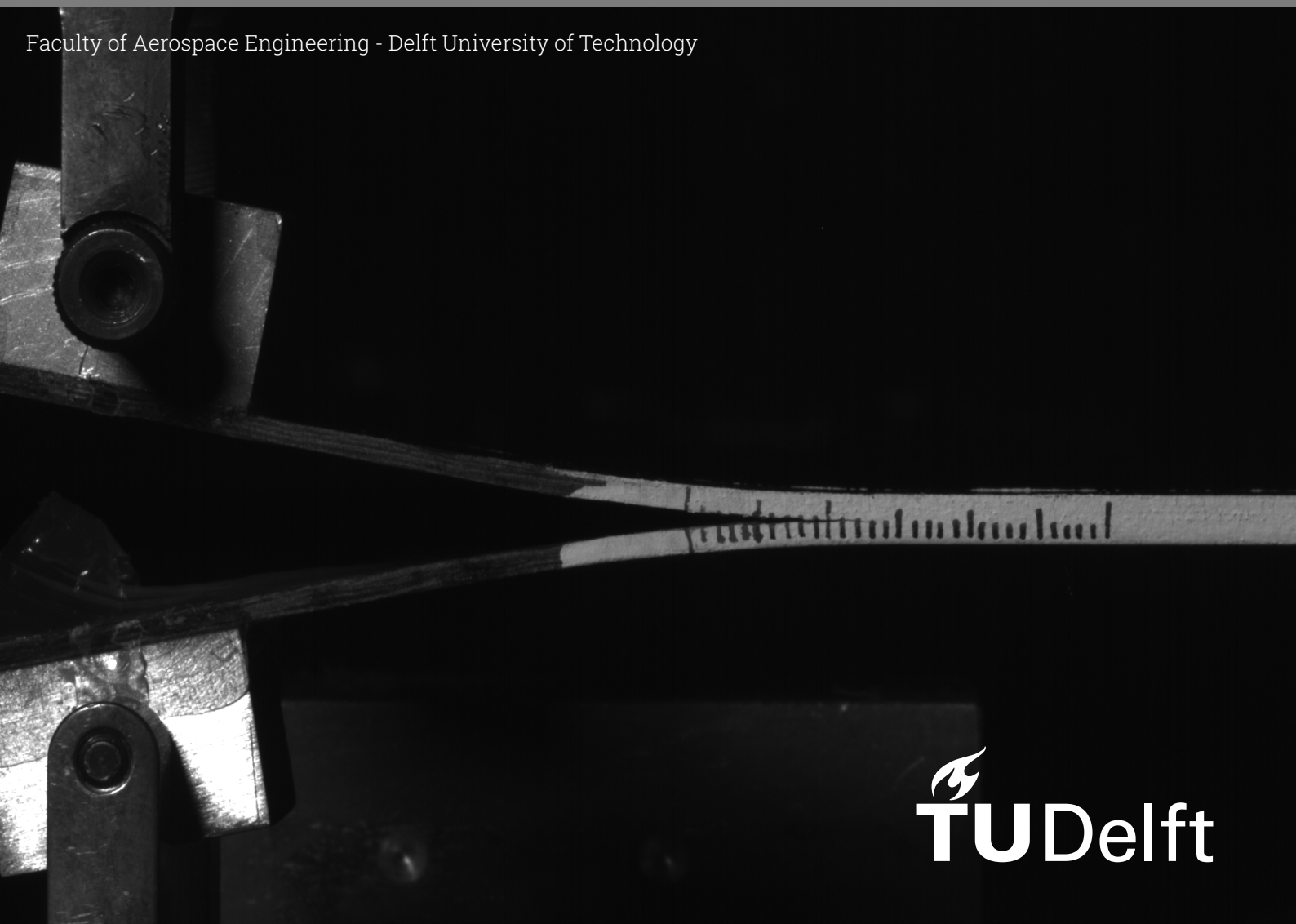

TU Delft

Hygrothermal Effects on Fracture Toughness of Flax Fiber Reinforced Epoxy

by

Luca Alexander Baak

to obtain the degree of Master of Science
at the Delft University of Technology,
to be defended publicly on Wednesday, December 11th, 2024 at 14:00.

Faculty:	Faculty of Aerospace Engineering, TU Delft	
Student number:	5621739	
Project duration:	February 2024 – December 2024	
Thesis committee:	Dr.ir. J.A. Pascoe	Supervisor
	Dr. Y. Mosleh	Supervisor
	Dr.ir. O.K. Bergsma	Chair
	Dr. K. Masania	External

Cover: Mode I Fatigue testing of Flax Fiber Epoxy DCB specimen

An electronic version of this thesis is available at http://repository.tudelft.nl/.

TU Delft

Preface

I would like to extend my gratitude to my supervisors Yasmine and John-Alan for their invaluable support and guidance throughout my thesis. Our weekly meetings were of immense help and played an invaluable role in the completion of my thesis.

Furthermore, I would like to thank everyone else who contributed to this project. I am grateful to the technical staff at DASML for their support during the experimental campaign and to the Damage Management & Certification research group for always being available for questions, especially Francisco, Valentin, and Wenjie. I also extend my thanks to my fellow MSc students, Christian and Matej, for their assistance with specimen weight measurements during times when I was unavailable.

Finally, I would like to thank my friends, family, and loved ones, whose support and encouragement have been invaluable throughout this journey and the years leading up to it. I could not have achieved this without you.

Luca Alexander Baak
Delft, December 2024

Abstract

This thesis investigates the effects of hygrothermal aging on the mode I and mode II fracture toughness of flax fiber-reinforced polymer composites (FFRP) under quasi-static (QS) and fatigue (F) loading conditions. A key motivation for this study is the potential of FFRP to replace synthetic fiber composites, as FFRP offers competitive mechanical properties while being biodegradable and less energy-intensive to produce. However, one of the main limitations of flax fibers is their susceptibility to environmental conditions such as temperature and humidity.

Delamination is a common failure mode in composites, and conducting fracture testing under mode I and mode II conditions is crucial for designing durable components. Double Cantilever Beam (DCB) and End-Loaded Split (ELS) specimens were manufactured for mode I and mode II tests, respectively. Subsequently, hygrothermal aging was simulated by subjecting the specimens to one or two cycles of humidification and drying at elevated temperatures within a climate chamber. Quasi-static testing was performed on unaged, 1-cycle aged, and 2-cycle aged specimens, while fatigue testing was conducted exclusively on unaged and 1-cycle aged specimens.

Testing resulted in significant plastic deformation of the specimens, this was attributed to their insufficient stiffness. This invalidated the assumption of Linear Elastic Fracture Mechanics (LEFM). To better capture these effects, the analysis was conducted using the J-integral, based on non-linear fracture mechanics. While the J-integral cannot account for all observed effects, it provides for a more realistic approximation for comparative evaluation of fracture toughness between aging states.

The results reveal that in mode I QS testing, the initiation fracture toughness on average improved by 19% after one aging cycle, with no further increase observed after a second cycle, while mode II QS fracture toughness was insensitive to aging. In mode I fatigue testing, a reduction in delamination growth resistance was observed after one aging cycle. Mode II fatigue testing exhibited substantial variability within aging states, making it challenging to determine the influence of aging, although a reduction in variability was noted after aging. The increase in QS initiation fracture toughness is likely due to the plasticization of fibers and matrix.

These results indicate that aging does not have a straightforward effect on fracture toughness, as its impact varies between modes and regions of crack growth. These findings provide valuable insights for the design of FFRP and other biofiber composites, contributing to the development of more sustainable materials.

Contents

List of Figures

List of Tables

Nomenclature

Abbreviations

Abbreviation	Definition
4ENF	Four-point End-Notched Flexure
A1	Indication for 1-cycle aged specimens
A2	Indication for 2-cycle aged specimens
ANOVA	Analysis of Variance
ASTM	American Society for Testing and Materials
C-ELS	Calibrated-End Loaded Split
CBTE	Corrected beam theory using effective crack length
CNT	Carbon Nano Tubes
DASML	Delft Aerospace Structures and Materials Laboratory
DCB	Double Cantilever Beam
DEMO	TU Delft division for mechanical and electronic support
DIC	Digital Image Correlation
DMTA	Dynamic Mechanical Thermal Analysis
DSC	Differential Scanning calorimetry
ECM	Experimental Compliance Method
ECT	Edge Crack Torsion
ELS	End-Loaded Split
ENF	End-Notched Flexure
F	Fatigue
F1	Mode I fatigue
F2	Mode II fatigue
FDG	Fatigue Delamination Growth
FEP	Fluorinated Ethylene Propylene
FFRP	Flax Fiber Reinforced Polymer
FPZ	Fracture Process Zone
FRP	Fiber Reinforced Polymer
FRPC	Fiber Reinforced Polymer Composite
GFRP	Glass Fiber Reinforced Polymer
ISO	Internation Organization for Standardization
LEFM	Linear Elastic Fracture Mechanics
MCC	Modified Compliance Calibration
MP	Megapixel
NFRC	Natural Fiber Reinforced Composite
NPC	Non-Precracked
ONF	Over-Notched Flexure
PC	Precracked
PW	Plain Weave
QS	Quasi-Static
QS1	Quasi-Static mode I
QS2	Quasi-Static mode II
R-curve	Resistance curve
RH	Relative Humidity
SBT	Simple Beam Theory
SCB	Split Cantilever Beam
SEM	Scanning Electron Microscopy

Abbreviation	Definition
SERR	Strain Energy Release Rate
U	Indication for unaged specimens

Symbols

Symbol	Definition	Unit
A_1	MCC calibration parameter	[-]
a	Delamination length	$[m]$
a_0	Initial delamination length	$[m]$
a_i	i^{th} delamination length	$[m]$
b	Specimen width	$[m]$
C	Compliance	$[m/N]$
C_i	Compliance corresponding to i^{th} delamination length	$[m/N]$
da	Differential increase in delamination length	$[m]$
dU	Change in strain energy	$[Nm]$
da/dN	Crack growth rate	$[m/cycle]$
e	Total insert length	$[m]$
$E_{0.2\%}$	Young's modulus at 0.2% strain	$[N/m^2]$
E_{11}	Young's modulus along fiber direction	$[N/m^2]$
F	Large displacement correction factor	[-]
G	Strain Energy Release Rate	$[N/m]$
G_{12}	shear modulus	$[N/m^2]$
G_{IC}	Interlaminar fracture toughness mode I	$[N/m]$
G_{IIC}	Interlaminar fracture toughness mode II	$[N/m]$
h	Specimen thickness	$[m]$
J	J-integral, a measure of energy per unit fracture surface area	$[N/m]$
J_{max}	Maximum J-integral value during fatigue test	$[N/m]$
J_I	J-integral for mode I loading	$[N/m]$
J_{II}	J-integral for mode II loading	$[N/m]$
L_f	Free length of specimen between load application point and the clamp	$[m]$
L_S	Distance between the section S-S' and the clamp tool	$[m]$
l_1	Distance between the center of the load application point and specimen mid-plane	$[m]$
l_2	Distance between the center of the load application point and the edge of the load block	$[m]$
M	Moisture evolution	[-]
N	Number of cycles	[cycles]
N_{corr}	Load block correction factor	[-]
P	Applied load	$[N]$
P_c	Critical force	$[N]$
P_{max}	Maximum applied load	$[N]$
R	Displacement ratio in fatigue test ($R = \delta_{\text{min}}/\delta_{\text{max}}$)	[-]
S_a	Arithmetical mean height	$[\mu m]$
V_f	Fiber volume fraction	[-]
W_i	Mass of specimen at measured time	$[kg]$
W_0	Initial mass of specimen	$[kg]$
δ	Displacement	$[m]$
θ'_g	Rotation angle at distance L_s from clamp tool	$[rad]$
θ_p	Rotation angle of at load application point	$[rad]$
σ_{UTS}	Ultimate tensile strength	$[N/m^2]$

1

Introduction

In today's world, there is a growing importance on the use of sustainable and eco-friendly materials. This is driven by a growing awareness towards climate change, environmental pollution, and the depletion of natural resources [1, 2]. The field of composites has seen significant advancement in developing materials with superior strength-to-weight ratios for aerospace, automotive, marine, and civil engineering industries. However, the production of these synthetic fiber-reinforced polymers (FRPs) requires high energy and the use of non-renewable resources. Furthermore, synthetic FRPs are difficult to recycle [3]. For these reasons, biofibers such as flax have gained attention for their attractive environmental footprint, biodegradability, and specific mechanical properties comparable to those of glass fiber reinforced polymers (GFRPs) [4].

One of the main disadvantages of these biofibers limiting widespread adoption is their susceptibility to in-service environmental conditions, like temperature and humidity [5–8]. Therefore, research on the hygrothermal aging effects on biofibers is of utmost importance. Hygrothermal aging refers to the changes a material undergoes when exposed to various levels of temperature and humidity. This process may lead to changes within the individual fibers, matrix, and fiber-matrix interface. Most research on hygrothermal effects has been into the tensile properties and has observed significant degradation effects. Hygrothermal effects on fracture toughness have not yet been thoroughly investigated within current literature, despite the promising performance of flax fiber composites in terms of fracture toughness compared to glass fibers [9].

Fracture toughness is a critical parameter in the design of durable composite components. It describes the ability of a material to resist crack propagation. In the real world, composites are subjected to complex loading conditions, that can lead to initial delaminations and growth of cracks. Testing the fracture toughness under various loading modes, like tensile opening and shearing conditions, helps predict the lifetime and reliability of the composite material. Despite the importance of this parameter, the hygrothermal effects on fracture toughness have not yet been considered for flax fibers. This study aims to understand the hygrothermal effects on the fracture toughness of flax fiber reinforced polymer composites (FFRP) under both modes I & II in quasi-static and fatigue loading conditions.

The thesis is organized as follows. Chapter 2 presents a literature review, providing essential background information on flax fibers, fracture toughness, and hygrothermal effects. Chapter 3 defines the scope of the research, outlining the problem statement and research questions. Chapter 4 details the methodology for specimen manufacturing, testing, and analysis. In Chapter 5, the results are presented and discussed. Finally, in Chapter 6, the conclusions are discussed with recommendations for future work.

2

Literature Review

This chapter provides a review of the relevant aspects of hygrothermal effects on the fracture toughness of flax fiber-reinforced composites. First flax fibers will be presented in more detail, followed by an explanation of fracture toughness, common testing methods, and values found in literature. Lastly, the effects of hygrothermal aging will be presented on natural and synthetic fiber composites

2.1. Flax Fibers

Flax fibers are among the most commonly used biofibers in the world and are the oldest known fiber to be utilized by humans, over 34,000 years ago. They were discovered in a cave in the Republic of Georgia and may have been used for ropes, baskets, or garments [10, 11]. They come from a plant called Linum usitatissimum L. which belongs to a group of plants called Linaceae. Usitatissimum meaning most useful as it is the only species in the family with agricultural importance [12]. Flax fibers are used in various sectors like textile (linen), automotive, paper, etc. and in 2022 the total Flax fiber market was estimated to be worth $1.14 billion [13]. Of which about 10% of the Flax Linen market is used for technical products, 60% in fashion and 30% for home products, according to the Alliance of European Flax-Linen and Hemp [14].

Due to growing environmental awareness, plant fibers like flax fibers have gained significant interest as reinforcement material for composites. The environmental benefits in combination with their specific strength and -modulus make them a possible replacement for synthetic fibers, like glass fibers [15–17]. One of the main limitations of these fibers is their susceptibility to environmental parameters such as temperature and relative humidity, changing their mechanical properties and dimensional stability due to moisture absorption/desorption, which can cause internal cracks in the material [18–20]. Figure 2.1 shows a schematic overview of the internal structure of flax fiber, from the stem to the individual cellulose macrofibrils. The production of flax composite fabrics begins with about a 100-day growth stage, after which the plants are harvested and retted to facilitate the extraction of the fibers by decomposing the pectin. Next, the fibers are separated from the stem during the scutching and hackling process, which leaves individual technical fibers. These technical fibers have a diameter between $100\text{-}200\,\mu\mathrm{m}$ and can be in length up to $1\,\mathrm{m}$. Elementary fibers have a diameter between $10\text{-}40\,\mu\mathrm{m}$ and $20\text{-}40\,\mathrm{mm}$ in length [21]. Elementary fibers contain a primary cell wall and a secondary wall consisting of three layers namely, S_1, S_2 & S_3, primarily made up of cellulose $(77.1 \pm 0.5\%)$, hemicelluloses $(12.7 \pm 0.6\%)$, and lignin $(2.1 \pm 0.7\%)$. Other minor parts of the plant are extractives like pectin, starch, and other organic components $(6.9 \pm 0.1\%)$. Finally, the plant also contains inorganic components, generally named ash $(1.2 \pm 0.1\%)$ [22].

Cellulose is the primary structural component, providing strength and rigidity. It forms a fibrous, crystalline structure that allows plants to stand upright and grow tall. It can be divided into crystalline cellulose 43.9% and non-crystalline cellulose 33.2% [22]. The crystalline regions are hydrophobic, while the non-crystalline regions have an increased free volume, making them more vulnerable to water absorption [23]. Hemicellulose is a filler material within the cell walls surrounding the cellulose fibers. It helps

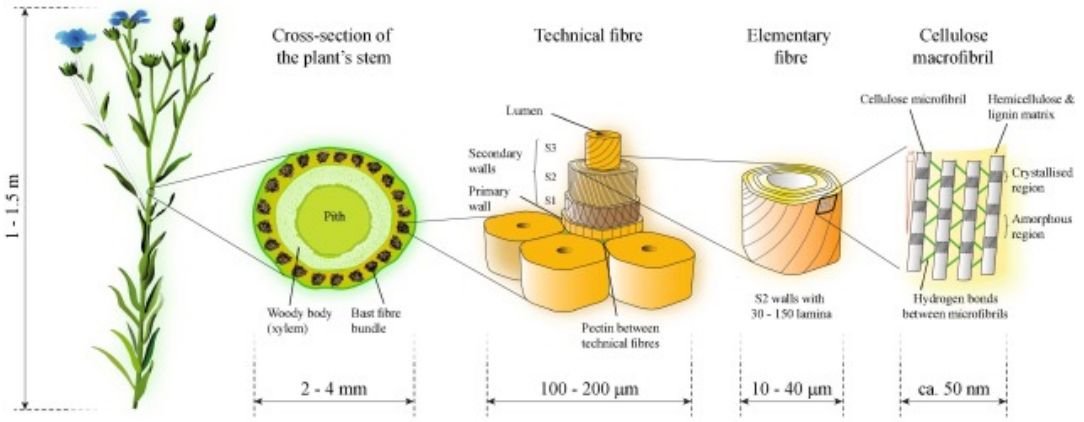

Figure 2.1: Multiscale schematic of flax fiber architecture, illustrating its structural hierarchy and key components [21].

bind the cellulose fibers together, contributing to the overall flexibility and resilience of the structure. Hemicellulose has a less compact structure compared to cellulose, making it more hydrophilic. Furthermore, hemicellulose is more prone to thermal degradation [24]. Lignin has an amorphous structure and is found in the remaining spaces of the cell wall and between the cells, giving further rigidity to the plant [25]. The structure of flax fiber and other biofibers can be considered a biocomposite, with lignin and hemicellulose being the matrix with cellulose fibers as reinforcement [18, 26]. The thick middle layer S_2 is the most important and determines the mechanical properties and is composed of helically wound cellular microfibrils formed from long-chain cellulose molecules. The angle of these fibrils is called the microfibrillar angle and determines much of the stiffness of the fibers.

Flax and other biofibers exhibit greater variability in mechanical properties compared to synthetic fibers. This scatter is largely attributed to the natural growth process, which is subject to changing meteorological conditions [27]. Additional factors influencing mechanical properties include damage accumulated during processing, the presence of defects such as kink bands within the fibers [28], and fiber diameter, as tensile strength at break has been shown to decrease with increasing fiber diameter [29].

Figure 2.10a shows a typical force-displacement curve for an elementary flax fiber tested in tension at a rate of 1 mm/min. The bi-linear behavior is evident, with two distinct linear regions, which is hypothesized to result from the re-orientation of the microfibrillar angle during loading [30].

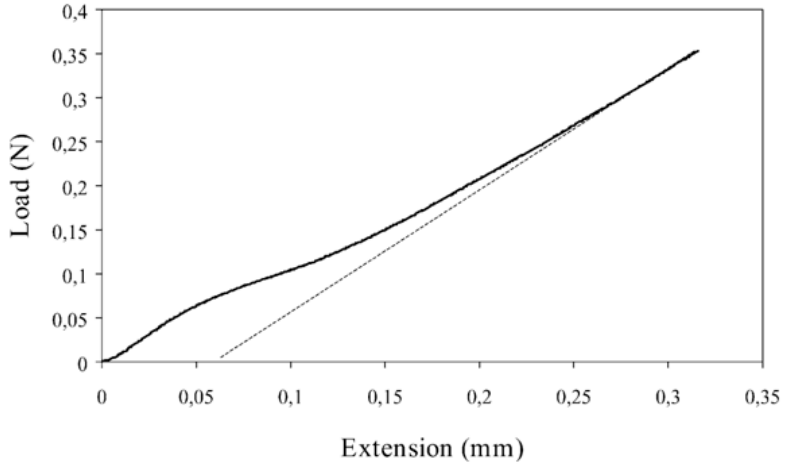

Figure 2.2: Typical bi-linear load-displacement curve for an elementary flax fiber [30].

To improve performance of technical fibers bundles can be twisted, so the yarns become more tightly configured improving the tensile strength [31, 32]. Further enhancements can be made by using various fiber treatments that increase the ratio of cellulose compared to hemicellulose, pectin, and lignin,

reducing the hydrophilic nature of flax fibers [18, 31, 33].

2.2. Fracture Toughness

Delamination growth in composite structures is one of the most critical, life-limiting failure modes [34, 35]. Fracture toughness is therefore a key material property in determining the durability and damage tolerance of fiber-reinforced polymers, as it enables predictions of a component's residual strength. This section will first describe the fundamental mechanics of fracture toughness, followed by an in-depth investigation of the fracture toughness of flax fibers, specifically focusing on mode I and mode II fracture modes under quasi-static and fatigue loading conditions.

2.2.1. Mechanics of Fracture Toughness

Due to anisotropic behavior and heterogeneity, fracture mechanics in FRP composites is a complicated phenomenon. Fracture toughness is usually denoted as the critical strain energy release rate G_C $[J/m^2]$, which is the energy required to propagate a crack per unit area of the crack surface. The value for fracture toughness is dependent on the mode of delamination which can be classified in mode I (G_{IC}), tensile opening mode, mode II (G_{IIC}), in-plane shear mode, and mode III (G_{IIIC}), out of plane shear. Figure 2.3 shows a visual representation of these modes. For a full picture on fracture toughness, these modes need to be mixed, as multiple modes can be present at once in real-life applications.

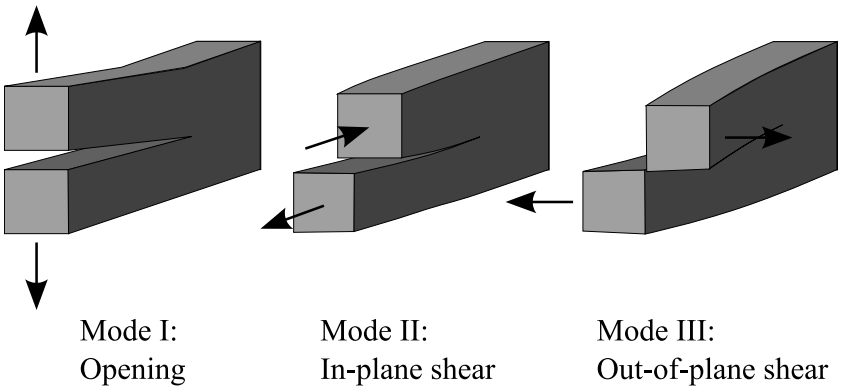

Figure 2.3: Illustration of mode I (tensile opening), mode II (in-plane shear), and mode III (out-of-plane shear) fracture mechanisms.

The fracture toughness of composites can be measured using various standardized testing methods. Standards have been established by the International Organization for Standardization (ISO) and the American Society for Testing and Materials (ASTM). Mode I testing is most commonly conducted using ASTM D5528 or ISO 15024, which employ double cantilever beam (DCB) specimens [36]. For mode II, ASTM D7905 recommends the use of end-notched flexure (ENF) specimens [37], whereas ISO 15114 suggests using calibrated end-loaded split (C-ELS) specimens [38]. Mode III testing is commonly performed using edge crack torsion (ECT) and split cantilever beam (SCB) specimens [39]. These tests have not been standardized due to difficulties in introducing pure mode III loading [40]. All specimens are manufactured with an initial delamination, often introduced through the insertion of a non-adhesive film in the mid-plane of the specimen, to act as a delamination starter. In the real world, delamination can be initiated through flaws in the material introduced during the manufacturing process, like voids and porosity. But also during service through damages such as impact [41, 42], and hygrothermal conditions [43]. The main damage mechanisms for composites are matrix cracking, fiber breakage, debonding, and fiber pullout. Fracture toughness can be affected by many factors such as fiber orientation [44], matrix properties [45], fiber volume fraction and fiber-matrix interface [46, 47], which can significantly influence the fracture toughness of the material.

Crack growth can be influenced by intrinsic and extrinsic mechanisms, as shown in figure 2.4 where intrinsic mechanisms occur in front of the crack front and are related to the material's inherent properties like matrix and fiber-matrix interface. Extrinsic mechanisms occur behind the crack front, impeding crack evolution through mechanisms such as fiber bridging, pullout, and crack deflection [48, 49].

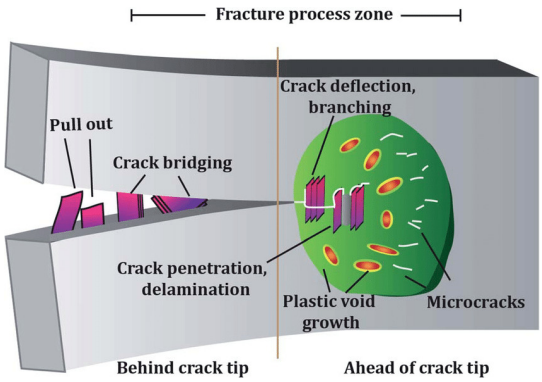

Figure 2.4: Schematic illustration of intrinsic and extrinsic toughening mechanisms in FRPC [50].

2.2.2. Parameters Affecting Fracture Toughness

Composites exhibit complex fracture behavior, and it is therefore important to understand the parameters affecting it. This section will go over the most important aspects pertaining to fracture behavior. Like matrix type, fiber-matrix adhesion, fiber bridging, fiber orientation. Environmental effects also play a role but will be discussed later in section 2.3.2

Matrix Type

The chosen matrix of a composite system has a significant effect on its fracture toughness. Research on the impact of various matrices on the fracture toughness showed that matrices with higher toughness generally show an increase in interlaminar fracture toughness [51, 52]. Typically, thermoset composites exhibit a lower toughness compared to thermoplastic due to the cross-linking limiting the plastic deformation and ability to absorb energy during fracture [53]. One way to reinforce the fracture toughness is through the addition of fillers like carbon nanotubes (CNT), resulting in crack-bridging and a pull-out mechanism [54]. The choice of matrix also influences fiber-matrix adhesion, which is discussed further below.

Fiber Matrix Adhesion

The effect of fiber surface texture and the adhesion characteristics with the polymer matrix are important contributors to fracture toughness. Strong adhesion allows the fibers to carry more load and leads to better load distribution. Various studies have experimented with fiber treatments, reporting significant increases up to 2.5 times for mode I in GFRP [55]. Biofiber composites generally have weaker fiber-matrix adhesion due to the hydrophilic nature of the fibers and the hydrophobic nature of epoxy [56]. Surface treatments of fibers have shown similar trends in increasing fracture toughens [57, 58]. In a study by V. Prasad et al. coating flax fibers with nano-TiO_2 and embedding in epoxy resin shows a 37% gain in 0.4 wt% TiO_2 for mode I and a 24% gain in mode II for 0.6 wt%, as can be seen in figures 2.5 a & b

Fiber Bridging

Fiber bridging is a phenomenon where fibers from adjacent plies span across the crack plane behind the crack front. This creates additional resistance, as these fibers transfer loads between neighboring plies, requiring a greater force to propagate the crack. Fiber bridging is often attributed to the nesting of adjacent fiber layers during the curing process, as illustrated in Figure 2.6 a & b [59].

The extent and influence of fiber bridging depend on several factors, including the type of fiber, fiber-matrix adhesion, laminate thickness, fiber orientation, loading conditions, and environmental factors [59, 60]. If the fiber-matrix interface is too strong, the fibers may break once the crack opens, as shown in Figure 2.6c, preventing the development of fiber bridging. In contrast, as shown in Figure 2.6d, a weaker fiber-matrix interface can allow fiber bridging to occur but may result in excessive fiber pullout, reducing energy absorption. Therefore, an optimal balance is necessary: the interface must be strong enough to ensure effective load transfer and prevent premature fiber pullout, yet not so strong that it leads to fiber breakage, which would negate the beneficial effects of fiber bridging.

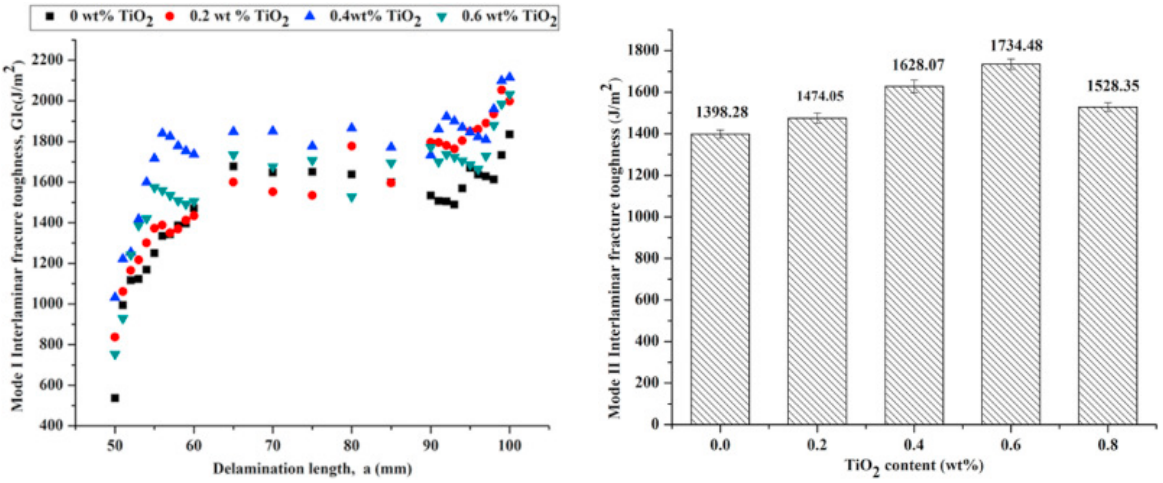

(a) Mode I R-curve

(b) Mode II initiation values

Figure 2.5: Mode I & II fracture toughness comparison of untreated-baseline and nano TiO_2 flax fiber coated samples at varying wt% [57].

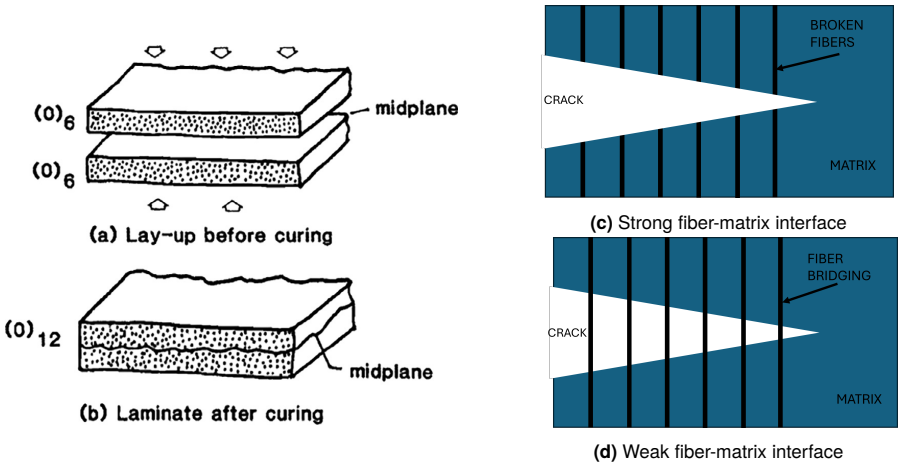

(c) Strong fiber-matrix interface

(d) Weak fiber-matrix interface

Figure 2.6: Origin of fiber bridging due to nesting (a & b) and due to effect of fiber-matrix interface (c & d) [59].

The effects of fiber bridging can be seen clearly in a crack growth resistance curve (R-curve), as can be seen in Figure 2.5a. As the crack grows larger the fracture toughness will increase as more and more fibers span the crack and absorb energy delaying crack growth. At a certain point the curve flattens, indicating that the fiber bridging zone remains constant, meaning that at the crack tip the same number of new bridging fibers are created as are broken or pulled out when the opening displacement becomes too large.

In a study by Yao et al. [61], a similar fiber bridging effect was observed on the Paris relation for mode I fatigue delamination growth in composites. Figure 2.7 illustrates how, for the same $\sqrt{\Delta G}$, the crack growth per cycle is faster when fibers are cut than when fiber bridging is present.

Fiber Orientation

Currently, standardized fracture toughness tests exist for unidirectional FRP composites. ASTM and ISO standards for mode I & II interlaminar fracture toughness state test laminates shall be made of unidirectional (UD) plies with delamination growth occurring in the 0 °direction [38, 62]. However, full-scale composite structures typically consist of varying fiber orientations and research has shown that this affects the delamination growth rate as it changes mechanisms like fiber bridging and crack migration [63]. Figure 2.8 shows the difference in fiber bridging between 0//0 interface and 0//90 interface.

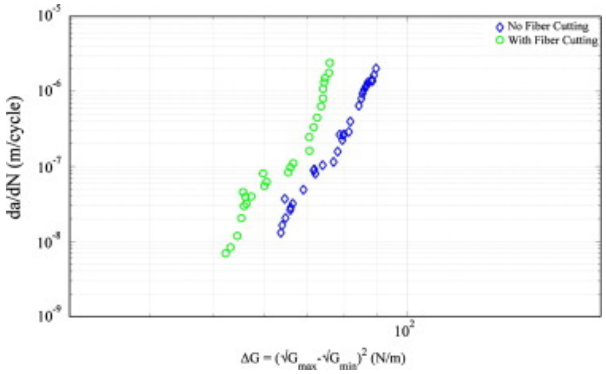

Figure 2.7: Fatigue delamination growth in specimens with and without fiber bridging [61].

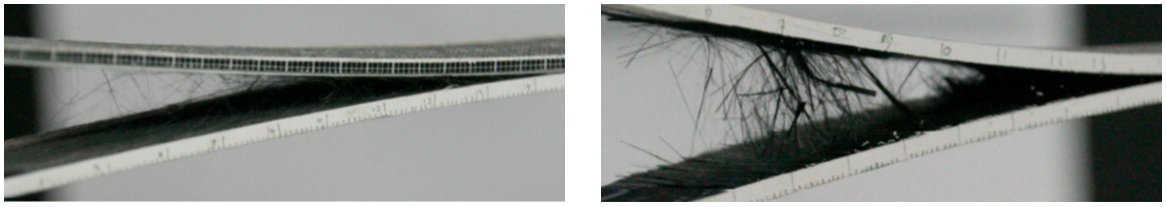

(a) 0//0 interface **(b)** 0//90 interface

Figure 2.8: Effect of fiber orientation on fiber bridging in mode I fracture toughness testing [63].

Reinforcements

The type of reinforcement fibers, such as glass, carbon, or flax, can significantly influence the fracture toughness of composite materials. Additionally, the type of fiber plies, such as UD or plain weave (PW), can also affect performance. Toughness can be further enhanced by stitching through the thickness of the laminate. Figure 2.9 compares glass UD and various flax fibers, including UD, PW, and stitched versus unstitched configurations. Flax fibers demonstrate favorable interlaminar fracture toughness (G_{Ic}) values compared to glass/epoxy composites, as shown in studies by Ravandi et al. (2016) and Saidane et al. (2019) [9, 64]. This improved toughness is largely attributed to the shorter, irregular geometry of natural fibers, which promotes enhanced fiber bridging between neighboring layers [65].

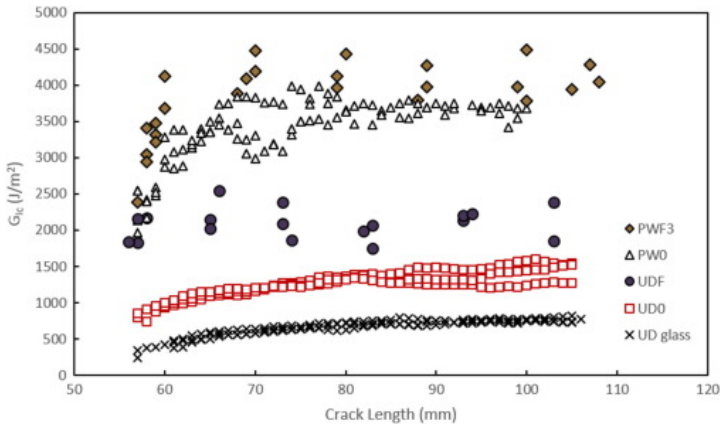

Figure 2.9: Comparison mode I fracture toughness, UD glass, UD0 - flax unstitched, UDF - flax stitched, PW0 - unstitched, PWF3 flax stitched [9].

Loading Rate

There have been many studies on the effect of loading rate on the fracture toughness of FRPs. Jacob et al. [66] reviewed a lot of work published on this topic and concluded that there is no clear consensus on the influence of loading rate on the fracture toughness. Some general conclusion that can be made are that the rate sensitivity of the polymer matrix can play a role in the fracture toughness and that

different failure modes may occur at different loading rates. Both ASTM and ISO standards for mode I fracture toughness specify loading rates between 1-5 mm/min. ISO 15114 for mode II ELS specifies a loading rate of 1 mm/min.

2.2.3. Mode I

Mode I interlaminar fracture toughness is most commonly evaluated using the standard test methods outlined in ASTM D5528 and ISO 15024. These standards specify a quasi-static testing procedure for determining both non-pre-cracked (NPC) and pre-cracked (PC) fracture toughness. For flax fiber composites, these methods have been employed across numerous studies to assess fracture toughness properties.

A study by Saadati et al. [65] provides an example of mode I fracture toughness evaluation for unidirectional (UD) flax fiber composites (g/m^2) in an M21/IMA epoxy matrix. The results indicate fracture toughness values of 574 J/m^2 at crack initiation and 903 J/m^2 during crack propagation. Figure 2.10 shows a typical load-displacement and corresponding R-curve from these tests. The load-displacement curve demonstrates a linear elastic response up to approximately 95% of the maximum load, followed by a gradual load drop, which is characteristic of stable crack growth in fiber-reinforced composites. The R-curve, derived from the force-displacement data, further illustrates the crack propagation behavior, showing a region of stable fracture toughness after the delamination length reaches roughly 60 mm.

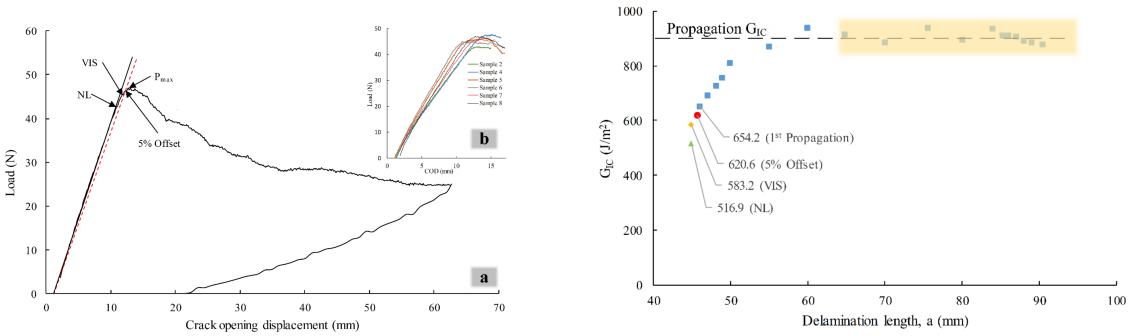

(a) Force displacement response

(b) R-curve

Figure 2.10: Mode I fracture toughness testing of flax epoxy [65].

The findings from similar studies on unidirectional flax fibers are summarized in Table 2.1. While these studies provide valuable insights into the approximate quasi-static fracture toughness properties of flax fiber composites, no research to date has examined fatigue delamination growth in flax fibers. This gap highlights an area for further investigation to fully understand the long-term performance and durability of flax fiber composites under cyclic loading conditions.

Table 2.1: Mode I fracture toughness study results for UD flax epoxy composites, following ASTM D5528.

Study	**Saadati** [65]	**Ravandi** [9]	**Li** [67]	**Yu** [68]	**Bensadoun** [69]	**Bensadoun** [69]
Reinforcement	UD $200\,\mathrm{g/m^2}$	UD $100\,\mathrm{g/m^2}$	UD $200\,\mathrm{g/m^2}$	UD $180\,\mathrm{g/m^2}$	UD $200\,\mathrm{g/m^2}$ $[90,0]_{2s}$	Quasi-UD $300\,\mathrm{g/m^2}$ $[90,0]_s$
Matrix	M21/IMA	Epolam 5015	E51/ MeTHPA	Techstorm 481/486	Epikote 828/ DCH-99	Epikote 828/ DCH-99
h [mm]	4	4	≈ 7.8	4.4	4-5	4-5
V_f [%]	41	40	60	60	40	40
$G_{Ic\_init}[N/m]$	574	771	≈ 1000	N/A	496	777
$G_{Ic\_prop}[N/m]$	903	1250	1400	1285	663	995

2.2.4. Mode II

In mode II fracture toughness testing, there is less consensus on the optimal testing method. Four primary test configurations are commonly employed: end-notched flexure (ENF), over-notched flexure (ONF), end-loaded split (ELS), and a 4-point bending ENF setup [70]. Each method offers unique advantages and challenges, and the choice of method often depends on the loading conditions being studied.

In existing studies on mode II fracture toughness of flax fibers, summarized in Table 2.2, all reported values have been obtained using ENF specimens in accordance with ASTM D7905, which provides a standardized approach for mode II testing in composites. To the best of the author's knowledge, no research has yet explored the fatigue delamination behavior of flax fibers under mode II loading conditions. This gap underscores a potential area for further study, as understanding fatigue behavior is critical for assessing the long-term durability of flax fiber composites in practical applications.

Table 2.2: Mode II fracture toughness study results for flax composites, following ASTM D7905.

Study	**Saadati** [65]	**Bensad-oun** [69]	**Bensad-oun** [69]	**Rajend-ran** [71]	**Bensad-oun** [69]	**Prasad** [56]
Reinforcement	UD $200\,\mathrm{g/m^2}$	UD $200\,\mathrm{g/m^2}$ $[90,0]_{2s}$	Quasi-UD $300\,\mathrm{g/m^2}$ $[90,0]_s$	2x2 fabric $200\,\mathrm{g/m^2}$	Various fabrics 150-$400\,\mathrm{g/m^2}$	4H satin weave $200\,\mathrm{g/m^2}$
Matrix	M21/IMA	Epikote 828/ DCH-99	Epikote 828/ DCH-99	1006 Epoxy	Epikote 828/ DCH-99	Epofine 556/ Finehard 1926
h [mm]	4	4-5	4-5	4.8	4-5	4.2
V_f **[%]**	41	40	40	44	40	28
$G_{IIc\_init}[N/m]$	612	728	1533	962 (CC)	1315-1872	1405

Only initiation values are reported for mode II fracture toughness in ENF specimens, as crack growth in these specimens is often unstable [65, 72]. The ELS testing method, in contrast, provides the advantage of stable crack propagation but requires a more complex fixture with variability introduced by clamping forces. To address this, ISO 15114 includes a calibrated procedure for end-loaded split testing that compensates for clamping variability [38].

Both the 4-point ENF (4ENF) and over-notched flexure (ONF) methods allow for stable crack growth; however, both involve loading over the crack itself, which can introduce additional friction between the crack surfaces [70]. This frictional interaction may affect the accuracy of mode II fracture toughness measurements, presenting a challenge in achieving consistent and reliable results across studies.

2.3. Hygrothermal Effects

Moisture absorption in composite materials induces mechanical and physicochemical changes across multiple components, including the polymer matrix [5], the fiber/matrix interface [6, 7], and the fibers themselves. Biofibers, in particular, are highly susceptible to water absorption due to their unique fiber architecture and chemical composition, making them significantly more vulnerable to moisture compared to synthetic fibers [8].

It is therefore essential to study the hygrothermal behavior of biofiber composites, which involves subjecting samples to controlled aging under specific temperature and humidity conditions. This approach provides insight into how prolonged environmental exposure influences the mechanical properties of these materials, ultimately impacting their durability and performance. Understanding the hygrothermal effects is critical for predicting the long-term behavior of biofiber composites in real-world applications, where they may encounter varying environmental conditions.

2.3.1. Mechanisms of Hygrothermal Aging in NFRC

Numerous studies have investigated the hygrothermal aging of composites reinforced with both synthetic and natural fibers. While synthetic fibers are significantly less susceptible to aging than natural fibers, the composite as a whole is not immune to degradation. Reported aging mechanisms in the literature include matrix swelling, plasticization, matrix cracking, and debonding at the fiber-matrix interface [8, 73].

In natural fiber-reinforced composites (NFRC), the hydrophilic nature of the fibers plays a substantial role in the aging process. Figure 2.11 provides a schematic representation of water absorption through capillary action along the fibers and illustrates the multi-stage effects of moisture uptake on the composite [8]. These effects can lead to progressive degradation in mechanical performance, highlighting the importance of understanding hygrothermal behavior in NFRCs for predicting their long-term durability.

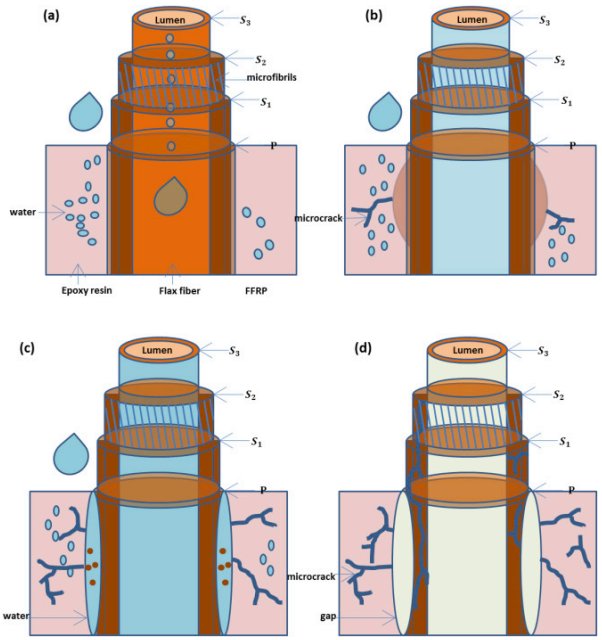

Figure 2.11: Illustration of hygrothermal aging mechanisms in flax fiber-reinforced polymers [8].

(a) Physical mechanisms, plasticizing and swelling (Reversible)

- Illustrated in figure 2.11(a) water penetrates the structure by diffusing into the matrix with the help of the capillarity of the fibers at the fiber-matrix interface. The hydrophilic nature of the fibers facilitates the transport through the lumens inside the fibers. Resulting in the binding of water molecules with hemicellulose and non-crystalline cellulose, leading to swelling of the fibers and eventually inducing cracks in the surrounding matrix.

(b) Damage mechanism, propagation of damage (Mostly irreversible)

- Figure 2.11(b) shows how water is absorbed in different cell walls of the fiber. A variance of swelling at different locations alters the microfibrillar angle and more matrix cracking, leading to changes in mechanical properties.

(c) Chemical mechanism (Irreversible)

- The continued aging due to moisture results in the leaching of various components such as pectins, hemicelluloses, and less crystallized regions of cellulose leading to fiber-matrix disbonding as can be seen in figure 2.11(c).

(d) Physical change (Irreversible)

- After prolonged exposure to moisture and subsequent drying, the fiber shrink and leave a gap as illustrated in figure 2.11(d). These gaps are locations of fiber-matrix disbonding and are weak points in the material.

To the author's best knowledge, no research has been conducted on the hygrothermal effects specifically related to the fracture toughness of flax fiber composites. This section will therefore focus on reviewing the hygrothermal effects on various mechanical properties of biocomposites, examining how moisture and thermal exposure impact mechanical properties. Understanding these effects is essential for evaluating the potential impact of hygrothermal aging on the fracture toughness of flax fiber composites.

In a study by Perruchoud [74], the in-service mechanical properties of flax fiber-reinforced polymer (FFRP) and glass fiber-reinforced polymer (GFRP) composites were compared under various environmental conditions using quasi-static tensile tests. The study examined cross-ply, fiber-dominated laminates, and angle-ply, matrix-dominated laminates, with results summarized in Table 2.3. For FFRP, in-service temperature and moisture conditions significantly affected the ultimate tensile strength and Young's modulus in both cross-ply and angle-ply laminates. Notably, higher humidity conditions led to increased ductility. In contrast, GFRP showed no significant changes in response to relative humidity (RH). For cross-ply GFRP laminates, the ultimate strength was dependent only on temperature, whereas angle-ply GFRP laminates exhibited significant changes in stiffness. Since these tests were conducted under consistent settings using the same epoxy matrix but different fiber reinforcements, it can be concluded that in-service temperature and humidity have a substantial impact on the mechanical performance of flax fiber composites. This study indicates that the epoxy matrix is primarily affected by temperature, while the flax fiber reinforcement is more sensitive to variations in both humidity and temperature.

Table 2.3: Ultimate tensile strength and Young's modulus of GFRP & FFRP tested at various temperatures and relative humidity [74].

Composite	**Property**	**20 °C / 50% RH**	**-20 °C / 50% RH**	**50 °C / 50% RH**	**20 °C / 90% RH**	**50 °C / 90% RH**
FFRP Angle-ply $[0/90/0]_s$	σ_{UTS}	225 MPa	230 MPa	200 MPa	260 MPa	215 MPa
	$E_{0.2\%}$	17 GPa	20 GPa	15 GPa	11 GPa	8 GPa
FFRP Cross-ply $[(+45/-45)_2]_s$	σ_{UTS}	55 MPa	80 MPa	No failure reached	52 MPa	No failure reached
	$E_{0.2\%}$	5.6 GPa	6.3 GPa	4.1 GPa	4.1 GPa	3.3 GPa
GFRP Angle-ply $[0/90/0]$	σ_{UTS}	630 MPa	720 MPa	-	590 MPa	550 MPa
	$E_{0.2\%}$	39 GPa	40 GPa	-	38 GPa	37 GPa
GFRP Cross-ply $[+45/-45]_s$	σ_{UTS}	94 MPa	107 MPa	72 MPa	90 MPa	70 MPa
	$E_{0.2\%}$	14 GPa	16 GPa	14 GPa	12 GPa	12 GPa

Li and Xue [8] studied the hygrothermal effects after immersion in water on the tensile properties of flax-reinforced epoxy and found similar trends as Perruchoud for immersion aging at lower temperatures. For specimens tested after immersion it was reported that the tensile strength at first slightly increases after which the tensile strength for 23 °C stabilized, slightly decreased for 37.8 °C, and considerably decreased for those aged at 60 °C. The effect of drying the specimens after aging was also studied and shown in Figure 2.12. Here it can be seen that aging at 23 °C only leads to a permanently reduced stiffness after 4 weeks of immersion time. For 38.7 °C, the stiffness starts to permanently decrease earlier, and the tensile strength also is affected after about 9 weeks. For aging at 60 °C the effects are much more serious and irreversible after 1 week of immersion. This was attributed toward, splitting and peeling of fibers and chemical degradation of the flax fibers.

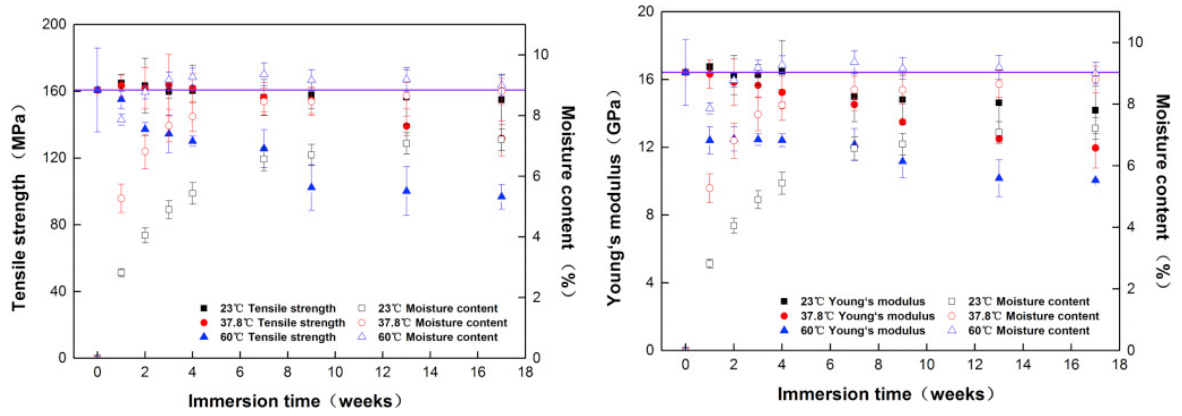

(a) Tensile strength [MPa] **(b)** Young's modulus [GPa]

Figure 2.12: Effect of hygrothermal aging and subsequent drying on tensile properties of unidirectional FFRP [8].

Van Schoors et al. [75] investigated the effects of cyclic hygrothermal aging on flax fiber bundles and unidirectional flax/epoxy composites. Samples were exposed to alternating humidity conditions, cycling between 3.5 days at 55°C/90% RH and 3.5 days at 55°C/40% RH, for a duration of up to one year. As shown in Figures 2.13a and 2.13b, tensile strength and strain at break remain relatively constant up to week 26. However, after one year of cycling, the tensile strength shows a reduction of approximately 12%, while strain at break decreases by around 20%. Figure 2.13c reports the stiffness as E_1 and E_2, corresponding to the initial and post-inflection point stiffness in the bilinear response of FFRP. Initially, both stiffness values decrease up to week 4, after which they stabilize, showing reductions of 8% for E_1 and 12% for E_2. These results highlight that while flax/epoxy composites maintain a degree of mechanical stability during the first six months of cyclic hygrothermal exposure, prolonged aging gradually impacts their tensile strength, ductility, and stiffness. This behavior underscores the importance of considering long-term environmental effects when assessing the durability and performance of flax fiber composites in applications exposed to fluctuating humidity and temperature.

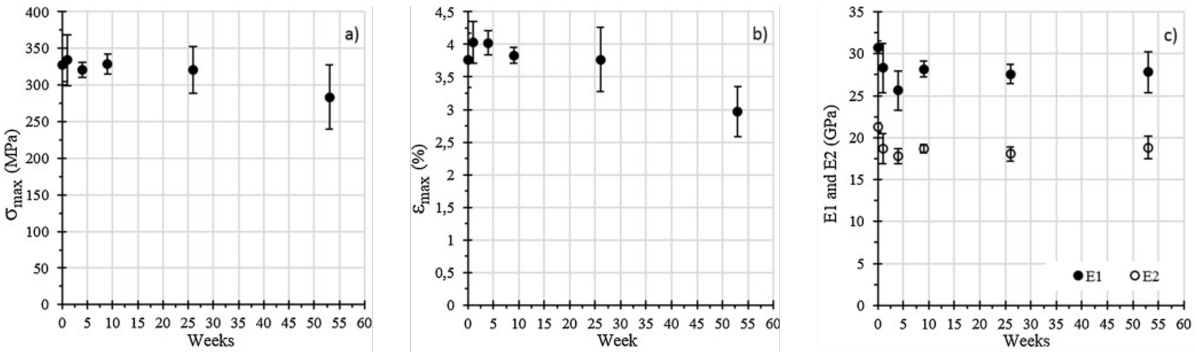

Figure 2.13: Impact of hygrothermal aging duration on tensile strength, strain at break, and Young's modulus of FFRP [75].

Calabrese et al. [76] investigated the effects of alternating salt fog humidity and drying cycles on the toughness of flax fiber-reinforced composites (FFRCs). Flax/epoxy specimens were exposed to 10 days

of salt fog at 35 °C, followed by an 18-day drying period at 22 °C and 50% relative humidity (RH), for up to three cycles. Mechanical properties were evaluated through three-point bending tests following ASTM D790. As shown in Figure 2.14a, this aging process led to a reduction in stiffness, with the material exhibiting increased ductility due to plasticization and softening of both the epoxy matrix and flax fibers. Figures 2.14b and 2.14c further illustrate how the drying phases partially restore the flexural modulus and strength after each cycle. These findings suggest that while exposure to humidity weakens and softens the material, the drying phases help to recover some of the mechanical properties, though the material remains more ductile than in its unaged state. This increase in ductility enhances the material's toughness, which is a measure of its ability to absorb energy prior to fracture. Toughness is commonly calculated as the area under the stress-strain curve, representing the total energy absorbed during deformation before failure. These results indicate that the cyclical exposure to humidity and drying not only affects the material's stiffness and strength but also modifies its energy absorption capacity, potentially offering improved toughness under certain environmental conditions.

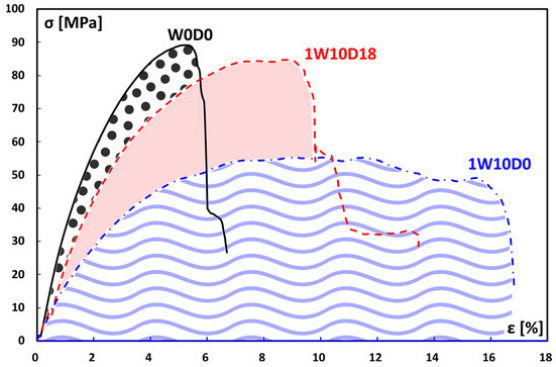

(a) Toughness stress-strain curves of:
Unaged (W0D0)
Aged not dried (1W10D0)
Aged and dried (1W10D18)

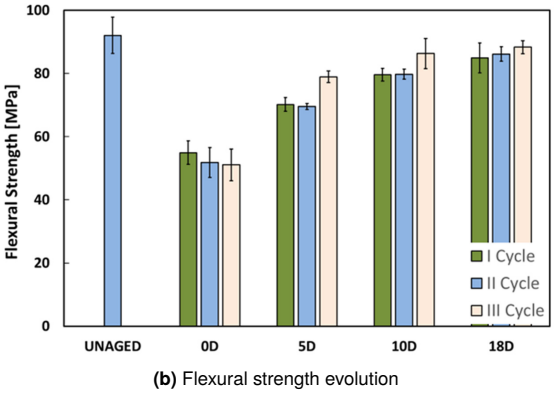

(b) Flexural strength evolution

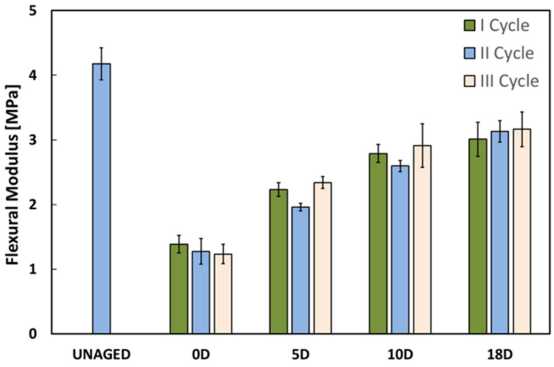

(c) Flexural modulus evolution

Figure 2.14: Effects of salt fog humidity and drying cycles on the toughness of FFRC [76].

2.3.2. Hygrothermal Effects on Fracture Toughness

While biofibers, such as flax, are gaining attention for their potential as sustainable reinforcements in composite materials, there is a distinct lack of research on the hygrothermal effects on their fracture toughness. Most existing literature has focused on synthetic fibers, like carbon and glass, to investigate hygrothermal aging effects. These studies provide valuable insights into how temperature and moisture influence fracture toughness, serving as a basis for understanding how similar conditions might affect biofiber composites. It is important to remember that in synthetic composites, moisture mainly affects the resin and not the fibers.

Research performed by Khan et al. [43] on the effects of hygrothermal aging on fracture toughness of carbon/epoxy composites. Samples were aged at 70 °C and 85% RH. The specimens were tested in mode I and mixed mode I & II according to ASTM D5528 and ASTM D 6671. For both tests, a reduction in fracture toughness was observed after aging, as shown in figure 2.15. However, statistically, the difference was considered insignificant for mode I and inconclusive for mixed mode I & II. For both

tests, fractography using Scanning Electron Microscopy (SEM) did confirm an enhancement of matrix ductility due to plasticization of the matrix after aging.

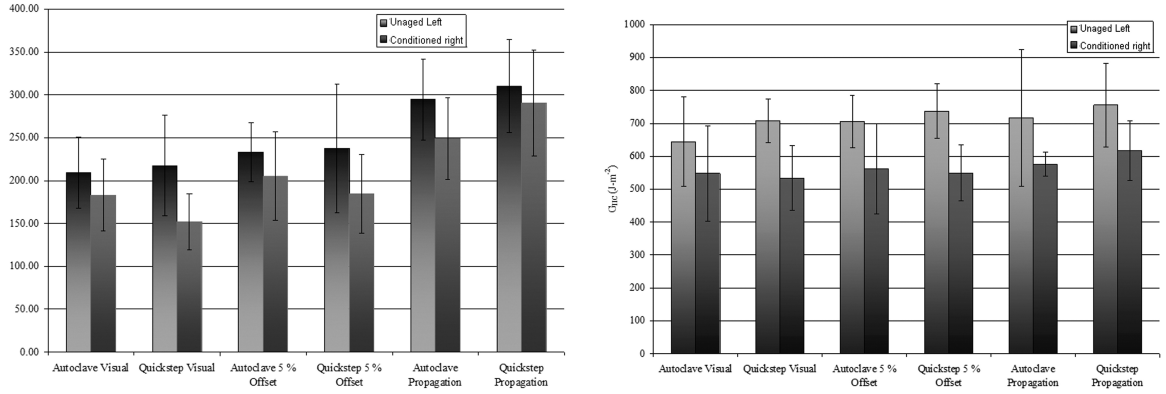

(a) Mode I

(b) Mixed mode I & II

Figure 2.15: Effect of hygrothermal aging on the mode I & mixed mode I & II fracture toughness of carbon/epoxy [43].

Russell and Street [77] reported a decrease in mode I and mode II fracture initiation toughness for graphite/epoxy samples with increasing temperature, but found no dependence on moisture content, as can be seen in Figure 2.16. The samples were aged at 75 °C and 100% RH. Propagation values, however, improved with increasing temperature, which was attributed to an increase in fiber bridge length with temperature. Pure epoxy was also tested using a Single Edge Notched (SEN) specimen, where fracture toughness increased with rising temperature. The authors attributed this contrasting response, between pure epoxy and composite samples, to residual stresses in the matrix surrounding the fibers, as well as to the fibers constraining the plastic damage zone size at the crack tip.

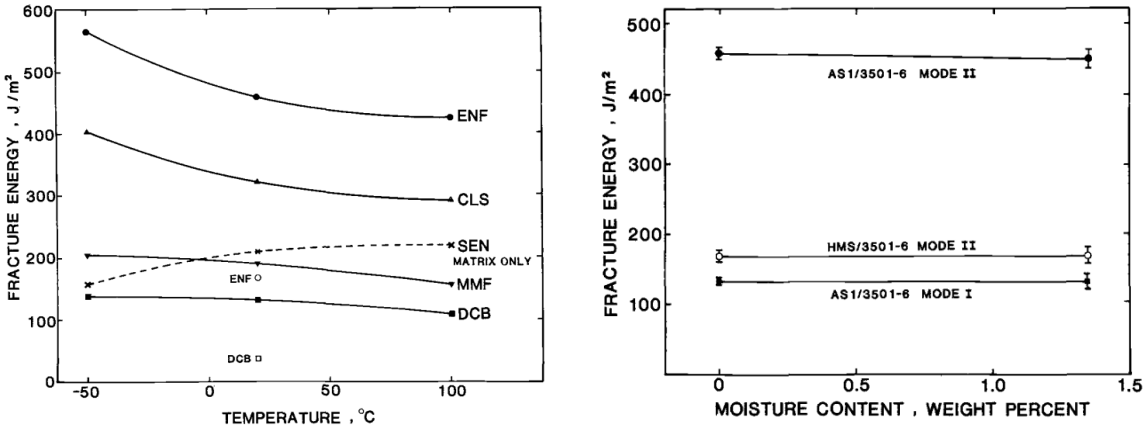

(a) Temperature effect

(b) Moisture effect

Figure 2.16: Effect of temperature and moisture on the mode I, II and mixed mode I & II fracture toughness of graphite/epoxy [43].

A study by Chou [78] on graphite/epoxy composites observed a slight reduction in initiation fracture toughness and a significant reduction in propagation toughness with varying moisture content. Mode I (DCB) dry and wet (1.6 wt% absorbed) have lower G_{Ic} characterized at P_{NL} compared to the 50% humidity equilibrium samples (0.2 wt% absorbed). Characterizing at P_{MAX} or $P_{5\%}$ leads to less of a difference, with P_{MAX} being the opposite, where the 50% equilibrium samples were observed to be lower. Crack propagation was considerably higher for dry specimens, with 50% equilibrium and wet samples were practically equal. For mode II (ENF), a similar observation was made where characterizing at P_{NL} resulted in significantly lower G_{IIc} for wet specimens, while P_{MAX} and $P_{5\%}$ did not lead to significant changes for moisture content.

In contrast, in a study by Garg and Ishai [79], the mode I (DCB) fracture initiation G_{Ic} of graphite/epoxy

was measured using acoustic emission. Testing in a room temperature environment did not lead to a significant increase for samples aged at 70 °C and 50% RH for over 98 days compared to dry samples. Aging at 70 °C in water for 62 days (2.1 wt% absorbed) resulted in a 25% increase of initiation fracture toughness. Testing dry specimens at 127 °C, increased G_{Ic} by 17%. This increase in fracture toughness was attributed to matrix plasticizing. Mode II testing appears to lead to a slight decrease of G_{IIc} with increasing moisture content, however a limited amount of specimens were tested with significant scatter.

Yao et al. [80, 81] researched the hygrothermal effects on carbon/epoxy fatigue delamination behavior. Specimens were aged at 70 °C at 85% RH (6 months) or in a water bath (4 months), until the effective moisture equilibrium changed less than 2%, within the measurement timespan. Testing was conducted at laboratory temperature conditions. The experiments demonstrated that fatigue delamination growth (FDG) is significantly influenced by hygrothermal aging, potentially increasing the crack growth rate by a factor of approximately 5. The influence of hygrothermal aging is shown in the Paris curve in figure 2.17. No significant difference was observed between the two aging methods. Fractographic analysis identified that hygrothermal aging had a detrimental impact on fiber/matrix adhesion and matrix porosity, however no obvious differences in damage mechanisms were identified between aged and unaged fracture surfaces. The degradation after aging was mainly contributed to fiber-matrix interface and matrix degradation induced by water absorption.

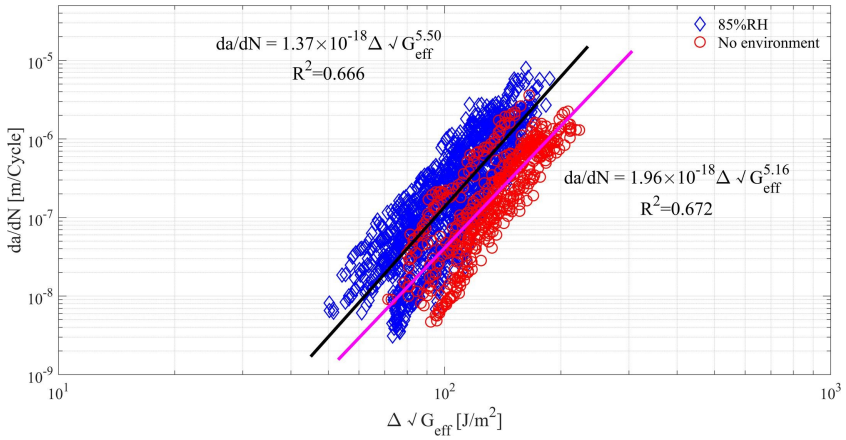

Figure 2.17: Effect of hygrothermal aging on fatigue delamination growth [80]

2.4. Summary of Findings

The literature review provides a comprehensive understanding of important aspects pertaining to flax fibers, fracture toughness and the effects of hygrothermal aging. Flax fibers offer a competitive and environmentally sustainable alternative to glass fibers. However, they are highly susceptible to environmental conditions, impacting their mechanical properties and dimensional stability, as hygrothermal aging may lead to fiber swelling, matrix plasticization and fiber plasticization and fiber-matrix debonding. Causing permanent changes to the material.

While the effects of hygrothermal aging on the tensile properties of FFRP has been extensively researched, the effects on its fracture toughness is unknown. Research on the effects on synthetic composites generally report a reduction in fracture toughness and fatigue delamination growth. However, for mode I fracture toughness, an improvement due to matrix ductility has also been reported.

The literature research highlights the gap in understanding the effect of hygrothermal aging on the fracture toughness of FFRP, this research aims to fill that gap by investigating the effects of hygrothermal aging on the mode I & II fracture toughness of FFRP in both quasi-static and fatigue loading conditions.

3

Research Scope

This chapter defines the scope of the study, including the problem statement, research objectives and key research questions. Together, these elements provide a structured framework for investigating the effects of hygrothermal aging on the fracture toughness of flax fiber-reinforced epoxy composites.

3.1. Problem Statement

Flax fibers offer the potential to replace glass fibers in certain composite applications, providing environmental benefits due to their lower environmental footprint and recyclability. However, for flax fiber-reinforced polymers (FFRPs) to become widely adopted, a more comprehensive understanding of their behavior during and after exposure to environmental conditions—such as temperature and humidity—is required. These conditions are common in many applications, including aerospace, wind energy, and automotive industries.

In biocomposites, environmental exposure is known to affect the fibers, matrix, and fiber-matrix interface, often resulting in changes to mechanical properties. Various studies have examined how moisture and temperature influence the tensile strength of FFRPs, showing significant degradation. However, no research to date has addressed the fatigue performance or the hygrothermal effects on fracture toughness of FFRPs. These properties are critical in designing durable composite structures, as they describe the material's resistance to crack growth under different loading modes encountered in real-world applications and in-service conditions.

3.2. Research Objectives

The main objective of this research was to evaluate the effects of hygrothermal aging on the fracture toughness of flax fiber-reinforced epoxy composites under both mode I and mode II fracture conditions, considering quasi-static and fatigue loading. To achieve this objective, the research was structured around the following aspects:

- *Quantifying the change in performance in mode I & II fracture toughness* due to hygrothermal aging under *quasi-static & fatigue* loading conditions. By conducting fracture toughness tests after exposing samples to controlled hygrothermal aging cycles.
- *Analyzing failure modes* of FFRP and the potential differences after aging through optical microscopy and scanning electron microscopy (SEM).
- *Analyzing the results and comparing them with existing data on carbon fiber reinforced composites* to understand the relative performance of flax fibers.

3.3. Research Questions

To research the hygrothermal effects on the fracture toughness of FFRP composites, the research question has been formulated as follows:

Main Research Question:

> To what extent does *hygrothermal aging* affect the *mode-I & -II fracture toughness* of *flax fiber* reinforced epoxy composites under *quasi-static* and *fatigue* loading conditions?

This has been divided up into the following sub-questions:

Sub Questions:

1. From literature, what microstructural and material properties influence the mode I & mode II fracture toughness of flax fiber reinforced composites?
2. What are the initial (pre-aging) mode I and mode II fracture toughness, of flax fiber-reinforced epoxy composites under *quasi-static* and *fatigue* loading conditions?
3. How does hygrothermal aging influence the microstructure and mechanical integrity of flax fiber-reinforced epoxy composites, and how does this affect the fracture toughness and fatigue delamination growth resistance?
4. How does hygrothermal aging affect the damage patterns and damage evolution in quasi-static and fatigue mode I & II loading conditions?

4

Methodology

This chapter outlines the methods and procedures used to investigate the effects of hygrothermal aging on the fracture toughness of flax fiber-reinforced epoxy composites. This chapter includes specimen preparation, experimental setup and analysis methods.

4.1. Specimen Preparation

The preparation of test specimens is critical to ensuring consistency and reliability in fracture toughness testing. This section describes the manufacturing process for mode I and mode II test specimens, quality control methods, the hygrothermal aging procedure, and provides an overview of the experiments conducted.

4.1.1. Manufacturing

The specimens for mode I and II testing were manufactured in the TU Delft composites lab. This section details the manufacturing process used to manufacture the specimens.

The composite material used in this study consists of Amplitex 280 flax fiber and SWANCOR 2511-1AL/BL epoxy. Amplitex 280g/m^2 is a quasi-unidirectional, non-crimp flax fabric produced by Bcomp in Switzerland. The polymer matrix is a thermosetting epoxy manufactured by Swancor Advanced Materials Co., based in Shanghai. This resin is characterized by moderate viscosity and an extended working time, making it well-suited for vacuum infusion processes.

The specimens were manufactured using two large aluminum plates that fit 500 × 500 mm plies. Both plates were thoroughly cleaned using acetone and coated with three layers of Marbocote 227 release agent to prevent the material from adhering to them during curing. Both mode I & II specimens were manufactured according to the stacking sequence, $[0_4//0_4]$ with "//" indicating the delamination plane created by inserting a $30\,\mu\mathrm{m}$ thick fluorinated ethylene propylene (FEP) release film at the mid-plane. This is slightly thicker than the recommended $< 13\,\mu\mathrm{m}$ per the ASTM and ISO standards. Figure 4.1 illustrates the manufacturing setup. To control specimen thickness, three layers of tacky tape were stacked between the top and bottom aluminum plates. The plies were oriented along the infusion direction, with release films positioned between two 4-ply stacks on each side of the panel. Once arranged, the top aluminum plate was placed over the plies, and a vacuum bag was applied over the assembly. This setup allowed the vacuum pump to infuse the panel efficiently along the fiber direction. The modified vacuum infusion setup, with the second plate over the fibers, ensures a smooth, uniform surface finish on both sides of the panel. This is essential for achieving consistent moisture absorption across both surfaces during aging.

After confirming the absence of leaks and ensuring a stable vacuum, the plates were infused and cured at room temperature for 24 hours. Following the initial cure, the panel underwent an 18-hour post-cure in an autoclave. Based on previous manufacturing trials, the manufacturer's standard cure cycle was extended to ensure full cure, as the original cycle showed an increase in glass transition temperature

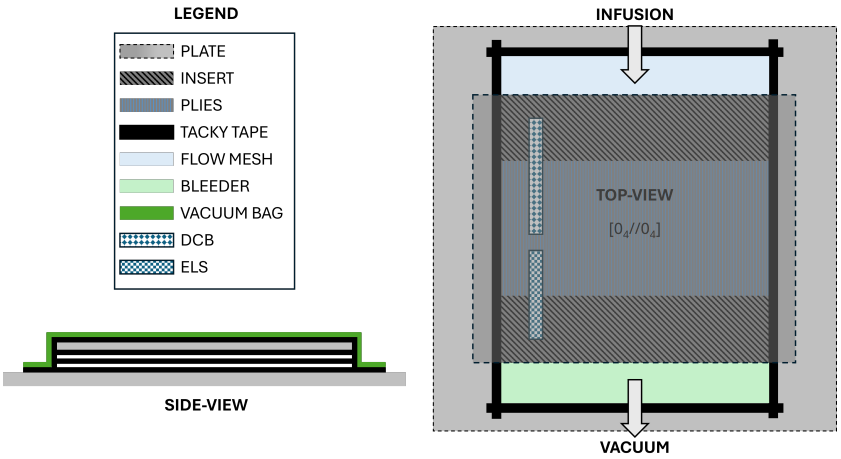

Figure 4.1: Schematic representation of the setup employed for manufacturing FFRP specimens.

(T_g) during DSC measurements, indicating incomplete curing. The modified cure cycle, shown in Figure 4.2, involves raising the temperature to 70 °C at a rate of 5 °C/min, holding for 18 hours at 7 bars of pressure. This cycle promotes full curing, improving the thermal and mechanical stability of the final panel.

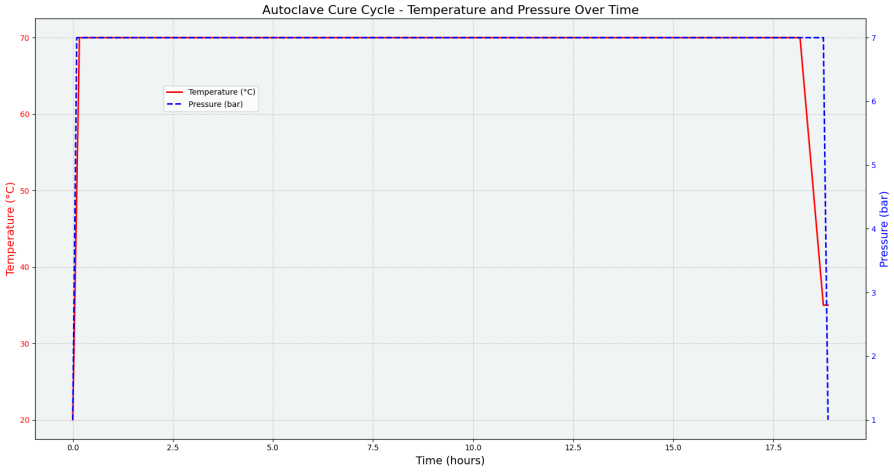

Figure 4.2: Diagram of the curing temperature and pressure inside the autoclave during the post-cure.

After the panel was fully cured, it was transported to DEMO, the electronic and mechanical support division at TU Delft, for waterjet cutting to achieve the final sample dimensions. The double cantilever beam (DCB) samples were cut according to ASTM D5528 standards, with a length (L) of 210 mm, width (b) of 25 mm, and an insert length of 60 mm. The end-loaded split (ELS) samples were cut to similar specifications, except with a reduced length of 170 mm. A total of 18 DCB and 18 ELS samples were cut from each plate. Figure 4.3 shows the manufacturing setup in the lab along with an image of one of the cut plates. To prevent the onset of delaminations due to the waterjet entry impact, the cutting path was initiated 5 mm prior to the sample edge. This adjustment allowed the high-pressure waterjet stream to stabilize before engaging the specimen, preserving the integrity of each sample.

For each testing condition, samples were used from various plates to minimize plate-to-plate variability due to subtle differences in manufacturing conditions like the height of the stacked tacky tape resulting in slight differences in thickness. Further variance may come from differing lab conditions, as not all plates were manufactured at the same time.

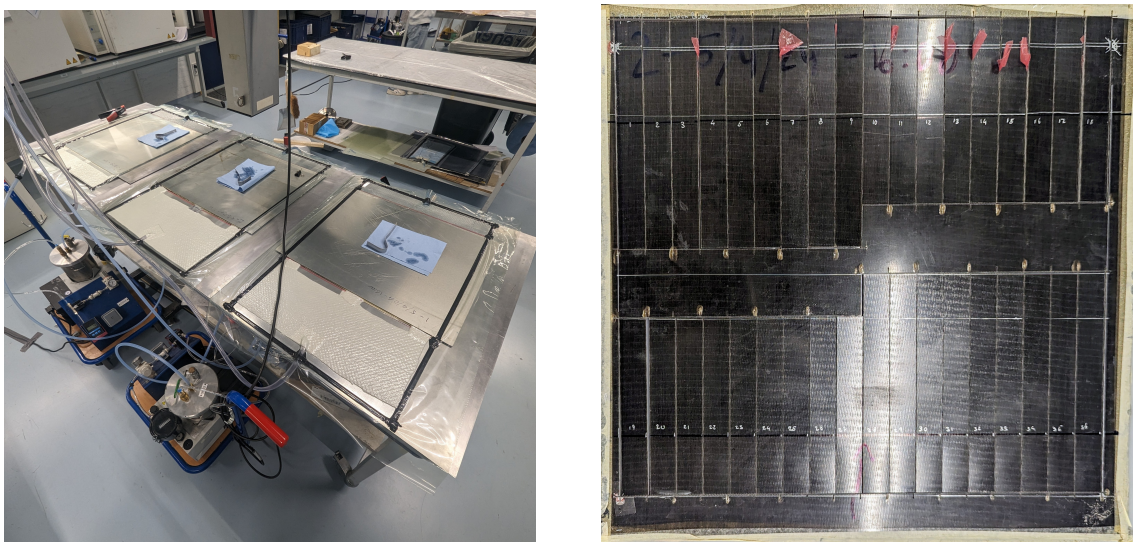

(a) Vacuum infusion setup **(b)** Resulting plate after waterjet cutting

Figure 4.3: Manufacturing setup in the composites lab and resulting plates.

After aging and prior to DCB and ELS testing, the samples underwent several preparation steps, including bonding of load blocks, marking measurement lines, and recording sample dimensions.

To improve crack visibility during testing, both sides of each specimen were coated with a thin layer of white industrial topcoat spray paint. For precise load transfer, aluminum loading blocks were bonded to the delaminated ends of the specimens. In mode I testing, these blocks were bonded to both sides of the specimen, while in mode II, the block was bonded only to the bottom side.

To ensure optimal bond strength, each loading block was prepared by sanding off residual epoxy, cleaning with acetone, sand-blasting the bonding surface, and cleaning it again, creating a uniform texture that promotes strong mechanical interlocking. The bonding region on the specimens was also lightly sanded to improve adhesion. Alignment during bonding was achieved using 3D-printed fixtures, and Loctite EA 3430 Epoxy was applied to the loading blocks. After epoxy application, the specimens were carefully aligned within the fixture and clamped to maintain constant pressure during the 24 hour curing process. The setup for both DCB and ELS preparation is illustrated in Figure 4.4.

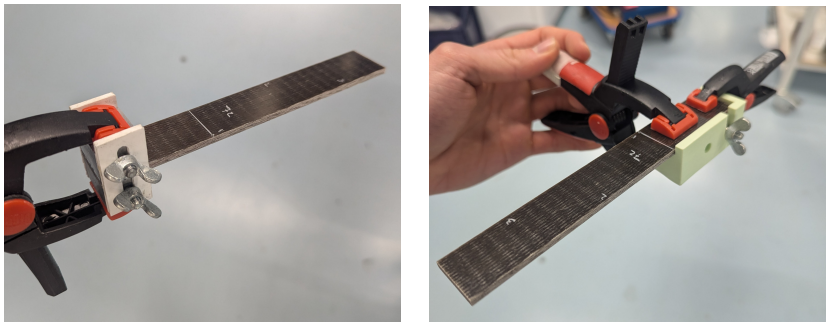

(a) DCB bonding **(b)** ELS bonding

Figure 4.4: Bonding procedure for load blocks on DCB & ELS samples.

After curing for 24 hours at room temperature, the fixtures were removed, and thin vertical lines were marked along the edge of each sample to facilitate visual detection of delamination growth. Marks were placed at 1 mm intervals starting from the end of the insert for the first 10 mm, followed by 2 mm intervals, as specified by ASTM D5528. For the ELS samples, an additional line was drawn 7 mm from the clamp to assist in monitoring the angle change at this location. Finally, prior to testing, the width, and thickness of each sample were recorded at the midpoint and 50 mm from either end. Figure 4.5

shows a fully prepared specimen ready for testing.

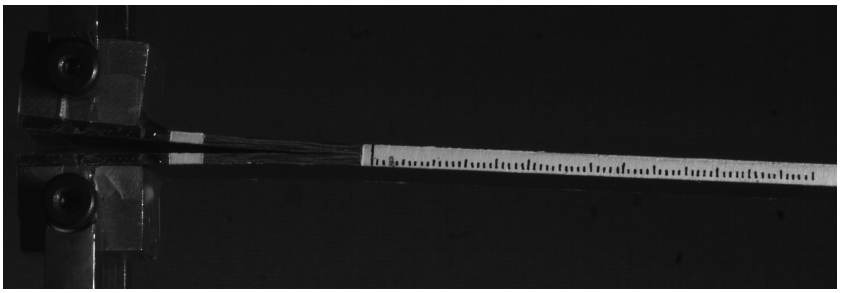

Figure 4.5: Fully prepared specimen ready for testing.

4.1.2. Quality Control

To ensure that the manufactured plates were suitable for testing, basic quality control procedures were conducted to assess their integrity and consistency. Dimensional measurements were taken to confirm uniformity, and Differential Scanning Calorimetry (DSC) was performed to determine the glass transition temperature (T_g), verifying that the matrix was fully cured. Additionally, cross-sectional samples were examined under a microscope to identify fiber volume fraction and potential defects, such as voids, fiber misalignment, and delaminations.

Specimen dimensions

The width, thickness, and weight of each specimen were measured prior to testing and are summarized in Table 4.1. Although the specimens were initially designed to have a uniform thickness of 4 mm, the manufacturing process, particularly the use of three layers of tacky tape to control thickness, resulted in slight variations across the plates and an average cured ply thickness of 0.44 mm instead of 0.5 mm.

Table 4.1: Average dimensions (width and thickness) of specimens per manufactured plate, including standard deviations.

	Plate 2		**Plate 3**		**Plate 4**	
	Average	Std	Average	Std	Average	Std
Width [mm]	25,18	0,02	25,23	0,40	25,17	0,07
Thickness [mm]	3,50	0,11	3,31	0,08	3,67	0,05

Differential Scanning Calorimetry

For each of the three manufactured plates, three samples were collected at three different locations near the center of the plate. These samples were then subjected to three cycles of:

- Equilibrate at 0 °C for 5 minutes
- Ramp 10 °C/min to 150 °C
- Isothermal 5 min at 150 °C
- Ramp down 10 °C/min to 0 °C

The results of the three specimens tested for plate 2 are shown in Figure 4.6. It can be seen that for each cycle the T_g, stays consistent, meaning that the plate is fully cured. Similar observation were made for plates 3 and 4.

Microscopy

To evaluate the internal structure of the plates, three cross-sectional samples from each plate were embedded in EpoFix resin, polished, and examined using a Keyence VK-X1000 confocal scanning microscope. The resulting images of each sample are shown in Figure 4.7. Plate 2 appears structurally sound, with black lines indicating stitching threads rather than voids. Plate 3 shows some noticeable voids in section 3-5, whereas sections 3-1 and 3-7 are largely free of defects. Similarly, Plate 4 has minor voids in sections 4-1 and 4-2 but is otherwise consistent in structure.

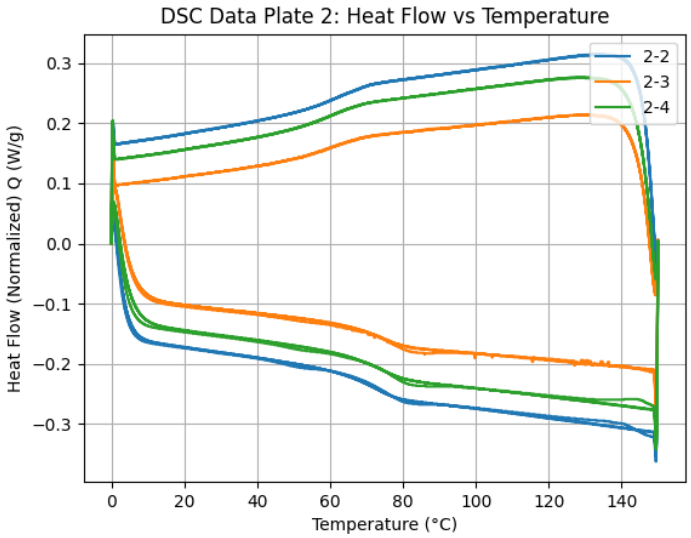

Figure 4.6: DSC results for plate 2, used to confirm consistency of T_g after curing.

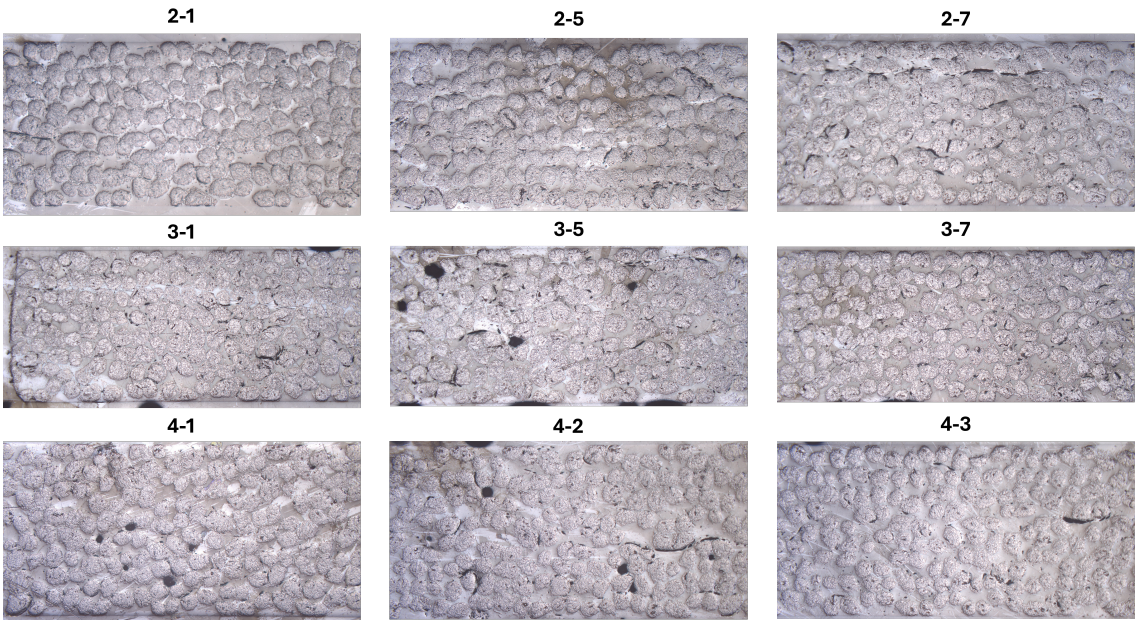

Figure 4.7: Cross-sectional images from plates 2, 3, and 4, highlighting fiber distribution and structural integrity.

The fiber volume fraction for each plate was estimated based on the weight and volume of the specimens, along with the known densities of the components. The volume of voids was assumed to be negligible in these calculations. The density of the Swancor 2511 resin was determined to be 1.15 g/cm^3, and the aerial weight of the fibers, as specified in the Amplitex datasheet, is 280 g/m^2. By measuring the weight and average dimensions of each specimen, the volumes of the epoxy and fibers were calculated. This method yielded fiber volume fractions of 43.2%, 46.3%, and 41.4% for Plates 2, 3, and 4, respectively.

Overall, slight differences were observed between the plates, primarily in thickness and fiber volume fractions. Despite these minor variations, all plates were deemed suitable for testing. However, to account for these differences, the fracture toughness values will be compared against the specifications of each individual plate.

4.2. Experimental Overview

The following section describes the experimental setup for both mode I and mode II testing under quasi-static and fatigue loading conditions. All tests were conducted at the Delft Aerospace Structures and Materials Laboratory (DASML). More detailed information on the experiments can be found in Appendix A.

Testing was conducted on specimens across three aging conditions: unaged, 1-cycle aged, and 2-cycle aged. An overview of the experiments is provided in Table 4.2. Quasi-static testing was organized into two rounds to manage the workload effectively. Round one included testing four unaged specimens and four specimens aged for one cycle. Round two involved testing all specimens aged for two cycles, as well as the remaining unaged and 1-cycle aged specimens. By saving unaged and 1-cycle aged specimens for the second round, all specimens were tested under similar laboratory conditions following the second aging cycle.

To systematically categorize the experiments, the following naming convention was used:

- **Type of tests:** Quasi-static (QS) or Fatigue (F)
- **Designation:** Each test was labeled with a unique identifier following the format X-Y-Z, where:
  - **Position 1 (X):** Specifies the type of test and fracture mode. For instance, ”QS1” refers to quasi-static mode I, while ”F2” refers to fatigue mode II.
  - **Position 2 (Y):** Indicates the aging condition of the specimen, where ”U” denotes unaged, ”A1” denotes 1-cycle aged, and ”A2” denotes 2-cycle aged.
  - **Position 3 (Z):** Sequential number assigned to each specimen tested under a given condition.

Table 4.2: Overview of Experimental Campaign.

Aging	Type of Test	Number of Experiments	
		Mode I	Mode II
Unaged	QS	6	6
1-cycle	QS	6	6
2-cycles	QS	6	7
Unaged	F	3	3
1-cycle	F	3	3

The table provides an overview of the experimental campaign, detailing the number of specimens tested under each loading mode and aging condition. This systematic approach allows for a robust analysis of how hygrothermal aging impacts the fracture toughness and durability of flax fiber composites under various loading conditions.

4.2.1. Hygrothermal Aging

During the lifetime of an aircraft, a wind turbine blade, or other outdoor structural components, materials are often exposed to extreme and fluctuating environmental conditions over both short and extended periods. To ensure the durability of such structures, it is essential to understand how materials respond under these environmental conditions, particularly in the case of flax fibers, which are highly susceptible to water absorption.

This thesis focuses on quantifying the effects of hygrothermal aging on flax fibers by exposing samples to controlled variations in humidity and temperature over an extended period, followed by testing under standard laboratory conditions.

To evaluate the effects of hygrothermal aging on the fracture toughness of flax fiber epoxy composites, specimens were subjected to a Weiss LF7m45 climate chamber, as shown in Figure 4.8. The aging cycle proceeded as follows: specimens were first exposed to 50 °C at 90% relative humidity (RH) until equilibrium was reached, then the RH was lowered to 30% where equilibrium was again allowed to establish, and finally adjusted to 50% RH until reaching equilibrium once more. Throughout each stage, the temperature was held constant at 50 °C to accelerate moisture absorption and desorption rates. During the final equilibrium phase at 50% RH, pristine (unaged) specimens were also placed in the climate chamber to ensure consistent testing conditions across both aged and unaged samples.

Figure 4.8: Weiss LF7m45 climate chamber used for controlled hygrothermal aging of specimens.

The weight of the samples was monitored every 2 to 4 days, with more frequent measurements taken immediately following changes in environmental conditions, when significant weight fluctuations were anticipated. As the samples approached equilibrium, the monitoring frequency was gradually reduced. Moisture evolution (M) was calculated using the following equation:

$$M = \frac{W_i - W_0}{W_0} \times 100 \tag{4.1}$$

Where W_i is the mass measured at each time interval, and W_0 is the initial mass of the sample. Equilibrium was determined by examining the moisture uptake graphs, where moisture evolution (M) was plotted against time. The results of these measurements are shown in Figure 4.9, with separate data for each aging condition and specimen type (ELS and DCB).

Notably, in Figure 4.9b, the specimens QS2-U-X1 through -X3 were initially set to 30% RH, as they were originally intended for in-service testing. However, after several unaged tests failed and in-service testing was canceled, the RH condition was quickly adjusted to 50%, before samples reached equilibrium at 30% RH.

In summary, the moisture evolution data confirm that equilibrium or near equilibrium was achieved for each aging condition, ensuring consistent pre-testing moisture levels across all specimens. These results provide a foundation for analyzing the effects of hygrothermal aging on fracture toughness in the subsequent tests.

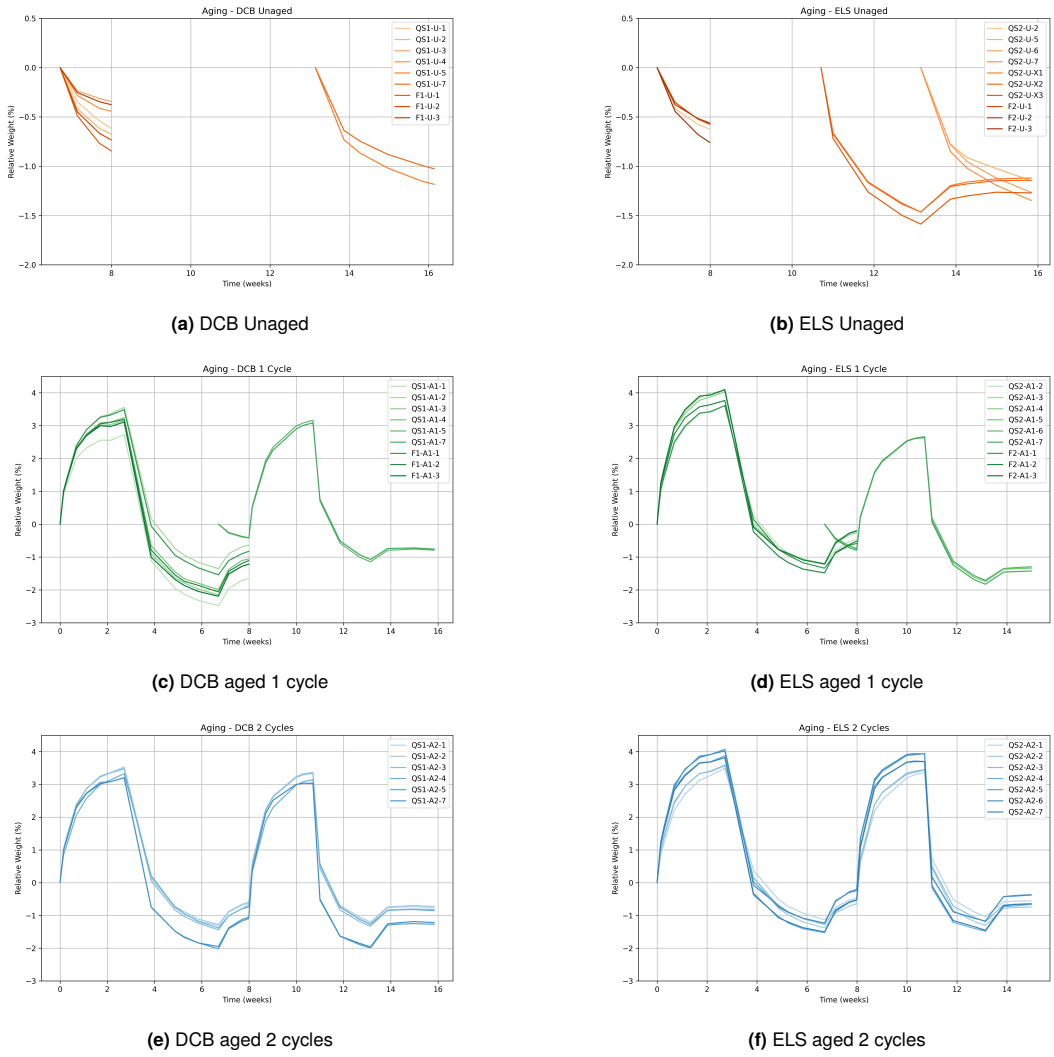

(a) DCB Unaged

(b) ELS Unaged

(c) DCB aged 1 cycle

(d) ELS aged 1 cycle

(e) DCB aged 2 cycles

(f) ELS aged 2 cycles

Figure 4.9: Moisture uptake behavior of DCB and ELS specimens during hygrothermal aging cycles, plotted over time.

4.2.2. Experimental Setup Mode I

ASTM D5528 provides the standard procedure for mode I interlaminar fracture toughness testing of unidirectional fiber-reinforced polymer matrix composites. In accordance with this standard, double cantilever beam (DCB) specimens were used with loading blocks to introduce the load, as shown in Figure 4.10.

Quasi-static fracture toughness

For quasi-static (QS) testing, a 10 kN Zwick testing machine with a 1 kN load cell was utilized. Crack growth was continuously monitored throughout the test using a 4-megapixel (MP) Optomotive camera equipped with an external spotlight, capturing images at intervals of 5–10 seconds. These images were saved directly to a computer stationed on the camera cart, which was linked to the Zwick control system. This setup enabled the image capture software to automatically generate a corresponding .txt file containing synchronized load and displacement data for each captured image, facilitating accurate tracking of crack progression and allowing for synchronization of images with the Zwick test data. The complete experimental setup, as implemented in the laboratory, is shown in Figure 4.11.

The initial non-pre-cracked (NPC) loading cycle was conducted under displacement control at a constant crosshead speed of 2 mm/min. Loading was manually halted using a trigger button once a crack growth of 3–5 mm had been achieved, after which the specimen was unloaded. This initial cycle provided data for calculating the NPC G_{Ic}. In the subsequent, pre-cracked (PC) loading cycle, the same

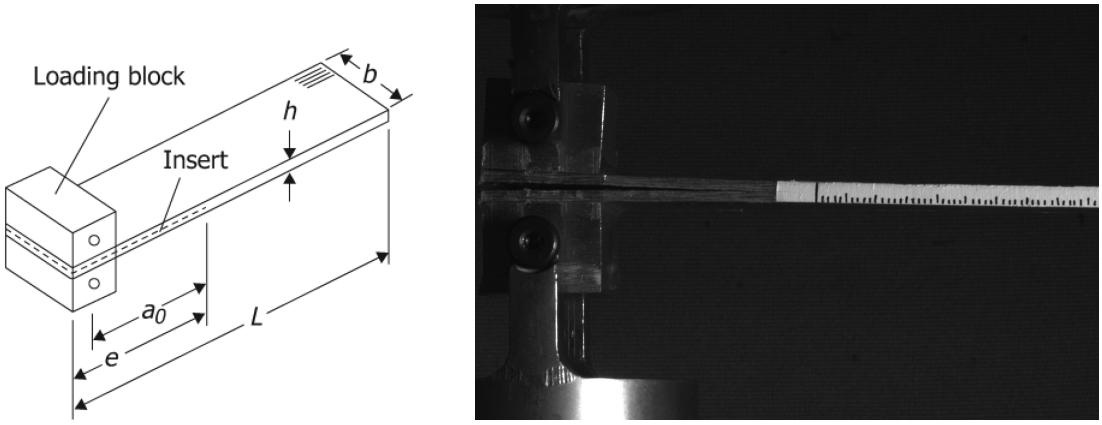

(a) Schematic DCB [36]

(b) Manufactured DCB

Figure 4.10: Schematic and manufactured DCB specimen, highlighting the specimen's configuration for mode I fracture toughness testing.

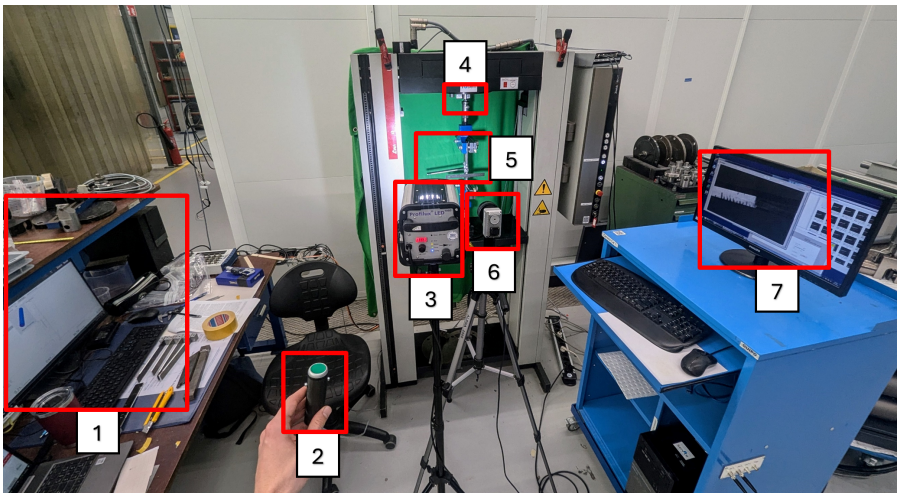

Figure 4.11: Experimental setup for mode I testing, highlighting the DCB specimen, test control system, and associated measurement devices, specified below:

1. Test control
2. Trigger
3. LED lights
4. 1 kN load cell
5. DCB test specimen
6. Camera
7. Camera car computer

crosshead speed was maintained, and the G_{Ic} initiation and propagation values were measured up to a crack size in the range of 100-120 mm. These values were then used to generate an R-curve for the material, to represent the fracture toughness for various aging states.

Fatigue fracture toughness

For fatigue testing of mode I crack opening, an MTS 10 kN fatigue test bench with a 1 kN load cell was used. The test setup was similar to that used for quasi-static (QS) testing, with the primary difference being the use of the fatigue test bench to apply cyclic loading. Fatigue testing was conducted at a displacement ratio (R) of 0.2, as initial trials at $R = 0.1$ resulted in significant negative loads at minimum displacement values due to plastic deformation in the specimen arms. This issue persisted to a lesser extent at $R = 0.2$. The cyclic loading was applied at a frequency of 5 Hz, with displacement cycling between 3.4 mm and 17 mm. A thermocouple was attached to the initial specimen to monitor any potential temperature increase resulting from the applied cyclic frequency. No significant temperature rise was observed, confirming that the specimen remained unaffected by thermal effects during testing.

To monitor crack growth during fatigue testing, images were captured, at 14 mm of displacement, every 100 cycles for the first 10,000 cycles, and every 1,000 cycles thereafter. Testing continued until either crack propagation approached the limits of the specimen or 200,000 cycles were reached.

4.2.3. Mode II

For mode II testing, the selection of an optimal method was less straightforward than for mode I. Various methods are commonly used in the literature, with End-Notched Flexure (ENF) being the most widely applied and the only method found for testing of flax fiber composites. However, ENF testing does not allow for stable crack growth, limiting the measurement to initiation toughness only. Therefore, for the purposes of this thesis, the End-Loaded Split (ELS) method was selected to enable stable crack propagation throughout the test. ELS is also the recommended method for mode II testing according to ISO 15114, which outlines a procedure for determining mode II fracture toughness, as illustrated in Figure 4.12. The fixture used in this setup allows the specimen to be firmly clamped while enabling the clamping arrangement to slide freely in the horizontal direction.

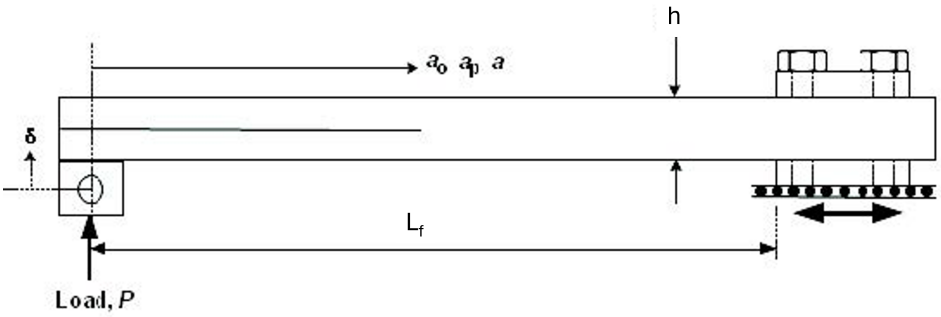

Figure 4.12: Illustration of the ELS specimen configuration for mode II interlaminar fracture testing [38].

Quasi-static fracture toughness

During initial trials, several complications arose when following the recommended procedure outlined in the standard. The calibration procedure produced highly variable results and left specimens permanently deformed. Additionally, pre-cracking in mode II led to significant plastic deformation. To address these issues, it was decided to manually grow the crack by 2–5 mm. This was accomplished by clamping the specimen at the base with the insert facing upward, then gently inserting a thin metal strip into the crack opening while visually monitoring the crack growth.

The pre-cracked specimen was then positioned in the test fixture with a free length (L_f) of 75 mm, as shown in Figure 4.13. Clamping was achieved by applying a 5 Nm torque to all four bolts, ensuring an evenly distributed clamping force. The 75 mm free length was selected to minimize the deflection needed to propagate the crack. Testing was conducted at a crosshead speed of 1 mm/min, continuing until a maximum displacement of 60 mm or until the crack reached within 10 mm of the clamp. During testing, load and displacement values were recorded, and images were captured every 10 seconds to monitor crack growth.

The experimental fatigue setup was similar to the configuration described in Section 4.2.2, but employed the MTS 10 kN fatigue machine. The setup, shown in Figure 4.14, was used for both quasi-static (QS) and fatigue testing.

Fatigue fracture toughness

The fatigue experimental setup is the same as for the QS tests. The difference is in the designed test program in the fatigue bench. Testing was conducted at R-ratio of 0.2, to keep things consistent with mode I. During the test the displacement cycled between 21 mm and 4.2 mm at a frequency of 3 Hz. The test was run until the crack had grown to within 10 mm from the clamp or at 200,000 cycles, which ever came first. To monitor crack growth, images were captured at 17 mm of displacement, every 100 cycles during the first 10,000 cycles, after which images were taken every 1,000 cycles. The minimum and maximum force and displacement values were recorded for each cycle.

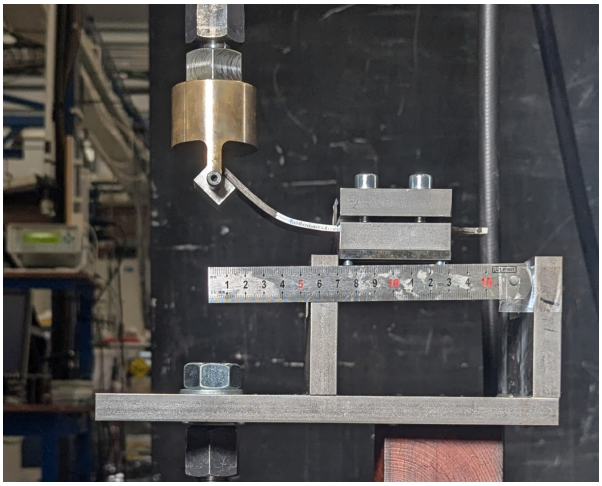

Figure 4.13: ELS fixture used for mode II fracture toughness testing.

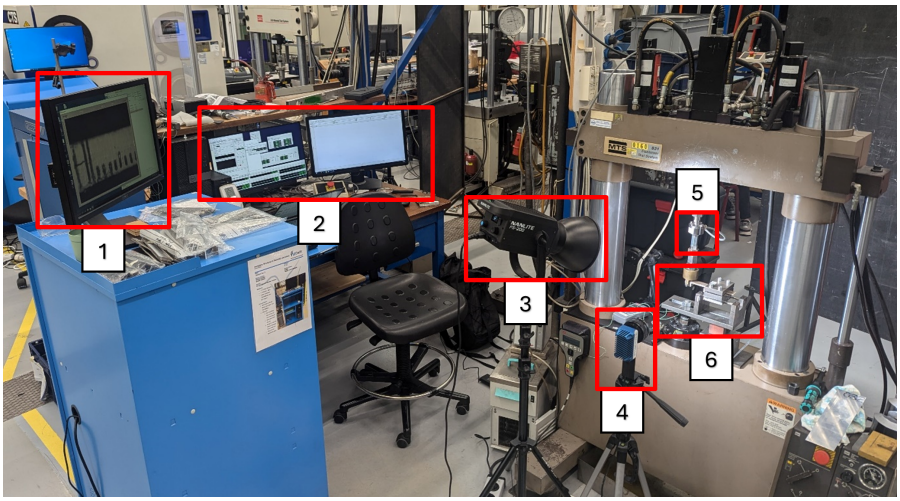

Figure 4.14: Experimental setup for mode II testing, highlighting the ELS specimen, test control system, and associated measurement devices, specified below:

1. Camera car computer
2. Test control
3. LED light
4. Camera
5. 1 kN load cell
6. ELS fixture with specimen

Similar to the observations made during mode I fatigue testing, initial trials in mode II revealed considerable plastic deformation in the specimens. This deformation introduced an unintended effect: the test effectively transitioned into a mixed-mode I and II configuration. Specifically, the upward displacement caused permanent deformation in the top arm of the specimen, which, in turn, resulted in a tensile opening effect on the downward motion. This phenomenon created a mode I component in addition to the intended mode II loading. As a result, each cycle of loading and unloading subjected the specimen to a combination of shear and tensile forces. This unintended mixed-mode effect is illustrated in Figure 4.15.

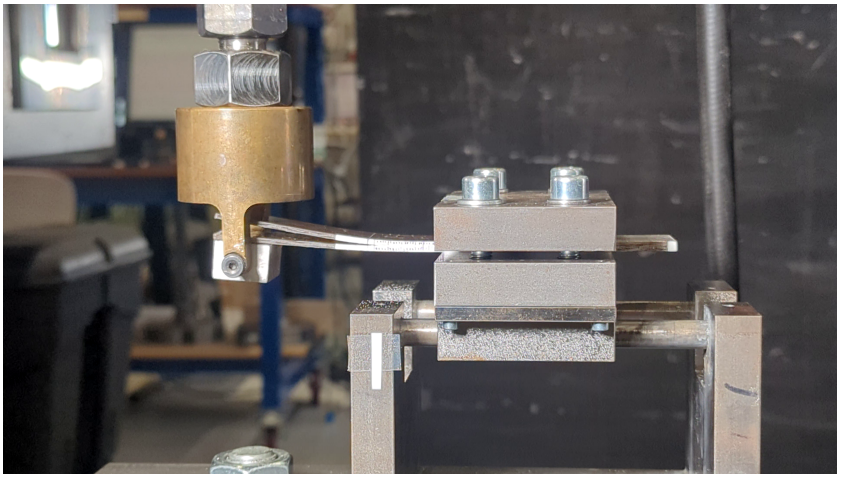

Figure 4.15: Unintentional mixed-mode I & II loading during mode II fatigue.

4.3. Analysis

This section outlines the approach used to analyze the data collected during the testing phase. It begins with the method for determining crack lengths, followed by the calculations for mode I and mode II fracture toughness under both quasi-static (QS) and fatigue loading conditions. The final part of this section describes the procedure for assessing surface roughness and obtaining high-resolution fractography images to further characterize fracture surfaces.

4.3.1. Crack Length Determination

Accurate determination of crack length is essential for calculating fracture toughness in both quasi-static (QS) and fatigue tests. Although similar principles are applied, each testing condition required slightly different approaches. The following subsections describe the methods used to measure crack growth in QS and fatigue tests, respectively.

Quasi-Static

The method for determining the crack length from the obtained images was consistent across, mode I & II QS testing. Before every test, the initial delamination length was measured and marked on the side of the specimen. The location of the initial delamination could accurately be determined by shining a bright light on one side of the specimen. The area where the release film was located appeared as a darker surface on the other side of the specimen. From the initial delamination, additional marks were made every 1-2 mm to aid in determination of crack length.

For each test, hundreds and sometimes thousands of images were collected. However, not every image could be analyzed for crack length. In mode I a maximum of 67 crack lengths were measured. For mode II, the maximum was 21, as the crack was not able to propagate as far. Following the standard, during the first 10 mm of propagation, the crack length was measured at least every 1 mm, after which crack lengths were recorded at least every 2 mm. Figure 4.16, shows two representative images from which crack lengths were recorded from mode I and mode II tests.

Fatigue

For fatigue testing, the compliance method was used to estimate crack length during the test. A representative subset of images was selected at key intervals to directly measure crack lengths. These measured lengths were plotted against their corresponding compliance values on a logarithmic scale. Using linear regression to establish a linear relationship between compliance and crack length. This relationship allowed for the estimation of crack growth throughout the entire test, enabling continuous estimate of crack propagation while minimizing the need for extensive image analysis.

Figures 4.17a and 4.17b illustrate how this method provides estimated crack length values compared to the measured crack lengths for mode I and mode II, respectively.

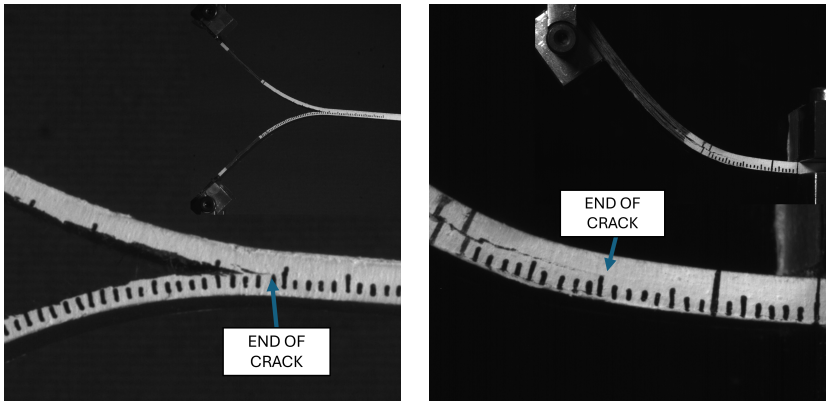

(a) Mode I — QS1-U-5_2816 **(b)** Mode II — QS2-U-5_1200

Figure 4.16: Zoomed-in images from mode I & II testing, used for crack growth analysis, with a full-scale view provided in the top-right corner.

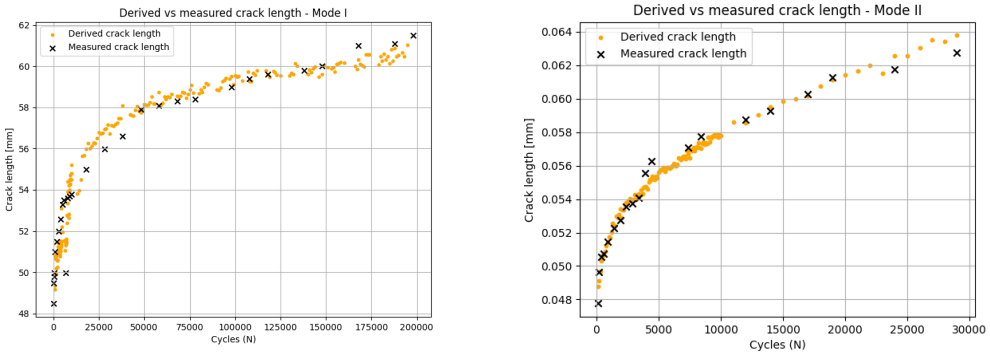

(a) Mode I — Compliance method **(b)** Mode II — Compliance method

Figure 4.17: Comparison of estimated and measured crack lengths for mode I and mode II tests, using compliance calibration methods.

4.3.2. Interlaminar Fracture Toughness

The interlaminar fracture toughness in this study was evaluated using two methods, namely the Strain Energy Release Rate (SERR) and the J-integral. These methods were applied to both mode I & II in QS and fatigue loading.

Strain Energy Release Rate

Using linear elastic fracture mechanics (LEFM), fracture toughness can be expressed as the strain energy release rate (SERR, G). This is defined as the loss of strain energy (dU) per unit of specimen width (b) for an infinitesimal increase in delamination length (da), assuming self-similar delamination growth under constant displacement. The general formula for G is given in Equation 4.2 [82].

$$G = -\frac{1}{b}\frac{dU}{da} \tag{4.2}$$

where:

U $=$ elastic strain energy
b $=$ specimen width
a $=$ delamination length

For mode I testing, the interlaminar fracture toughness, G_I, is calculated using the Modified Compliance Calibration (MCC) method, as described in ASTM D5528. This approach accounts for compliance

variations and includes correction factors, enabling an accurate measure of G_I under conditions where large displacements and or load block stiffening might otherwise affect results:

$$G_I^{MCC} = \frac{3P^2 \frac{C}{N_{corr}}^{\frac{2}{3}}}{2A_1 bh} F \tag{4.3}$$

where:

- P = applied force
- C = compliance, defined as δ/P, where δ is the displacement
- N_{corr} = load block correction factor
- A_1 = MCC calibration parameter
- h = Specimen height
- F = large displacement correction factor

The parameter A_1 is obtained by plotting $(C_i/N)^{1/3}$ versus a_i/h and applying linear regression to obtain the slope, as is illustrated in Figure 4.18. Where C_i = δ_i/P_i, the first two points on the plot correspond to the critical NPC and PC forces, the further points are from the propagation values. The correction factor F for large displacements is calculated as follows.

$$F = 1 - \frac{3}{10}\left(\frac{\delta}{a}\right)^2 - \frac{3}{2}\left(\frac{\delta l_1}{a^2}\right) \tag{4.4}$$

Where l_1, is the distance from the mid-plane of the specimen to the center of the pinhole. Finally, the loading block correction factor N_{corr} is calculated from:

$$N_{corr} = 1 - \left(\frac{l_2}{a}\right)^3 - \frac{9}{8}\left[1 - \left(\frac{l_2}{a}\right)^2\right]\left(\frac{\delta t}{a^2}\right) - \frac{9}{35}\left(\frac{\delta}{a}\right)^2 \tag{4.5}$$

Where l_2 is the horizontal distance from the center of the loading-block pinhole to the edge of the loading block.

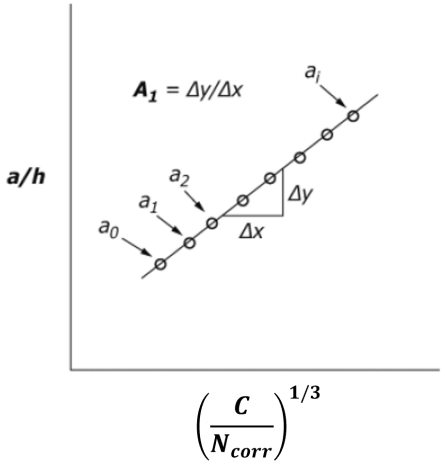

Figure 4.18: Modified compliance calibration method, illustrating the relationship between compliance and crack length for mode I fracture toughness analysis.

The critical force for calculating the NPC and PC initiation fracture toughness is determined by identifying a 5% increase in compliance from the original linear region of the force-displacement curve. This

linear region is defined as the portion between 25–75% of the maximum force. To determine the critical force P_c, a line with a 5% increase in compliance is plotted from the initial slope of the linear region. If this line intersects the force-displacement curve after the maximum force, then $P_c = P_{max}$. Otherwise, the critical force is taken as the point of intersection between the 5% compliance line and the force-displacement curve, designated as $P_c = P_{5\%}$. These critical points, along with the propagation values, are then plotted on an R-curve to visualize fracture toughness evolution with crack length.

For mode II, ISO 15114 recommends calculating the strain energy release rate (G_{IIC}) using corrected beam theory with an effective crack length (CBTE), as this approach is independent of direct crack length measurements. However, the CBTE method requires a clamp calibration procedure, which leads to permanent deformation of the specimens. To avoid this, the experimental compliance method (ECM) was employed, requiring the crack lengths to be measured from images obtained during testing, leading to more pronounced deviation within the specimens. The equation for ECM is shown below:

$$G_{II}^{ECM} = \frac{3P^2a^2m}{2b} * \frac{F}{N_{corr}} \tag{4.6}$$

Where the slope, m, is obtained by taking the slope of the linear relationship between the corrected compliance and the measured crack length cubed. The correction factors F, for large displacement, and N, for the effect of the load blocks, are given by:

$$F = 1 - \theta_1 \left(\frac{\delta}{L}\right)^2 - \theta_2 \left(\frac{\delta l_1}{L^2}\right) \tag{4.7}$$

$$N_{corr} = 1 - \theta_3 \left(\frac{l_2}{L}\right)^3 - \theta_4 \left(\frac{\delta l_1}{L^2}\right) - \theta_5 \left(\frac{\delta}{L}\right)^2 \tag{4.8}$$

Here l_1 represents the distance from the mid-plane of the specimen to the center of the pinhole, and l_2 represents the distance from the center of the pinhole to the edge of the load block. Theta values are calculated as follows:

$$\theta_1 = \frac{3}{20}\left\{\frac{15 + 50\left(\frac{a}{L}\right)^2 + 63\left(\frac{a}{L}\right)^4}{\left[1 + 3\left(\frac{a}{L}\right)^3\right]^2}\right\} \tag{4.9}$$

$$\theta_2 = \frac{-3\left(\frac{L}{a}\right)\left[1 + 3\left(\frac{a}{L}\right)^2\right]}{1 + 3\left(\frac{a}{L}\right)^3} \tag{4.10}$$

$$\theta_3 = \frac{4}{1 + 3\left(\frac{a}{L}\right)^3} \tag{4.11}$$

$$\theta_4 = \frac{-9}{4}\frac{\left\{\left[1 - \left(\frac{a}{L}\right)\right]\left[1 + 3\left(\frac{a}{L}\right)^3\right] + 4\left(\frac{a}{L}\right)^2\left[1 - \left(\frac{l_2}{a}\right)^2\right]\left[1 + 3\left(\frac{a}{L}\right)^2\right]\right\}}{\left[1 + 3\left(\frac{a}{L}\right)^3\right]^2} \tag{4.12}$$

$$\theta_5 = \frac{36}{35} \cdot \frac{1 + \frac{3}{8}\left(\frac{a}{L}\right)^3\left[35 + 70\left(\frac{a}{L}\right)^2 + 63\left(\frac{a}{L}\right)^4\right]}{\left[1 + 3\left(\frac{a}{L}\right)^3\right]^3} \tag{4.13}$$

J-Integral Approach

The J-integral, originally developed by J. Rice, is rooted in nonlinear fracture mechanics [83], whereas the strain energy release rate (SERR, G) is limited to linear elastic fracture mechanics (LEFM). The J-integral theory was initially formulated for a two-dimensional strain field applied to a linear or nonlinear elastic material containing a crack, as illustrated in Figure 4.19.

Although initially developed for linear and nonlinear elastic materials, the J-integral was extended to accommodate small-scale yielding at the crack tip and has been shown to yield reliable results for larger-scale yielding as well [84, 85]. This adaptability makes the J-integral a valuable tool in fracture analysis for materials exhibiting plasticity and complex deformation behavior, as is observed in the tested specimens.

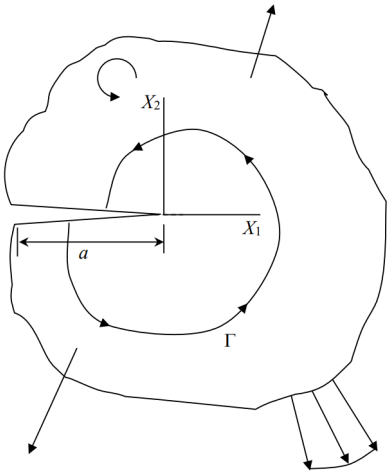

Figure 4.19: Two-dimensional body with a crack.

The general form of the J-integral as a path independent integral around the crack tip as described by Nilsson [86] is given by equation 4.14.

$$J = \frac{1}{b} \int_S \left(W \, \mathrm{d}\delta_{1j} - \mathbf{P}_{ji} \cdot \frac{\partial u_i}{\partial X_1} \right) N_j \, dS \tag{4.14}$$

Where W is the strain energy density and is a function of the stress and strain field as shown:

$$W = \int_0^{\epsilon_{ij}} \sigma_{ij} \, d\epsilon_{ij} \tag{4.15}$$

and,

δ = the Kronecker Delta
S = the contour surface
u = the displacement vector
dS = the counterclockwise incremental distance along the contour surface
P = Piola-Kirchoff stress tensor
N = outward normal unit vector to the contour

Following the derivation by Gunderson [84] and taking Figure 4.20 as reference, the displacement components can be written as:

$$u_1 = u + X_2 \sin \phi \tag{4.16}$$

$$u_2 = v - X_2\,(1 - \cos\phi) \tag{4.17}$$

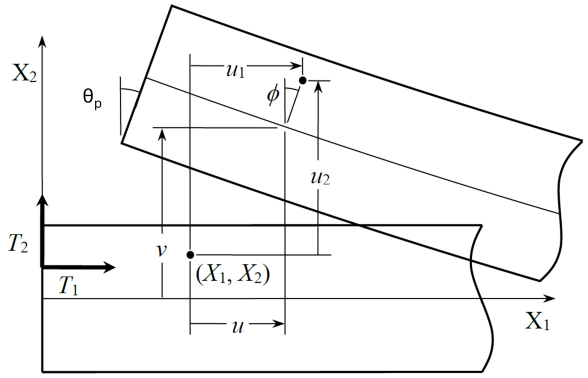

Figure 4.20: Coordinate convention for mode I J-integral approach [84].

The loading of the specimen can be described by nominal traction as $P_{11} = -T_1$ and $P_{12} = -T_2$. Now rewriting equation 4.14, yields

$$\frac{J_{\mathrm{I}} b}{2} = \int_{h/2} [W + T_1 \left(\frac{\partial u}{\partial X_1} + X_2 \cos\phi \frac{\partial \phi}{\partial X_1} \right) + T_2 \left(\frac{\partial v}{\partial X_1} - X_2 \sin\phi \frac{\partial \phi}{\partial X_1} \right)] \, b \, \mathrm{d}X_2 \tag{4.18}$$

Where $\frac{\partial u}{\partial X_1}$, $\frac{\partial v}{\partial X_1}$ and $\frac{\partial \phi}{\partial X_1}$ are constant with respect to X_2. The traction terms can be expressed as applied forces and moments, resulting in the following expression:

$$\frac{J_{\mathrm{I}} b}{2} = \int_{h/2} W b \, \mathrm{d}X_2 + P_1 \frac{\partial u}{\partial X_1} + P_2 \frac{\partial v}{\partial X_1} + M \frac{\partial \phi}{\partial X_1}. \tag{4.19}$$

The equation may be simplified by considering no or negligible moment, and only a vertical component as the force is applied through a pinhole, allowing for free rotation. Considering θ_p is the angle at the loading point, $\frac{\partial v}{\partial X_1} = \sin\theta_p$ the equation can be written as:

$$J_{\mathrm{I}} = \frac{2P}{b} \sin(\theta_p) \tag{4.20}$$

Pérez-Galmés et al. [87] proposed a data reduction method based on the J-integral for calculating the interlaminar fracture toughness in mode II ELS specimens, specifically when the material exhibits a significant Fracture Process Zone (FPZ).

Starting from the general J-integral expression in equation 4.14 and considering the deformed shape of the ELS specimen shown in Figure 4.21, the final equation for mode II fracture toughness can be derived under the following assumptions:

- The crack propagates in a straight line parallel to the x_1 axis
- The difference between θ_g and $\theta_g^{'}$ is negligible
- The curvature of the specimen is small compared to its length and the strains resulting from P_1 are negligible compared to the overall deformation

Under these assumptions, the mode II fracture toughness is given by the following equation:

$$J_{II} = \frac{3\,(P\cos\,(\theta_p))^2}{5 G_{12} b^2 h} + \frac{P\cos\,(\theta_p)\tan\,(\theta_p - \theta_g) - \tan\,(\theta_g)}{b} + \int_{-h}^{h} \left(-\frac{1}{2} E_{11} \varepsilon_{11}^2 \right) \mathrm{d}x_2 \tag{4.21}$$

Where:

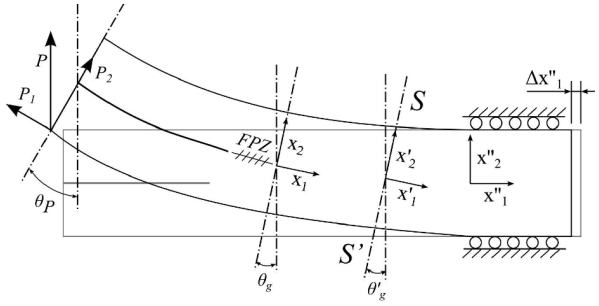

Figure 4.21: Illustration of deformed ELS specimen, indicating mode II J-integral components [87].

- P is the applied load,
- θ_p is the angle of the applied load,
- G_{12} is the shear modulus,
- b is the specimen width,
- h is half the specimen thickness,
- E_{11} is the Young's modulus in the fiber direction
- ε_{11} is the strain in the same direction.

The final integration in equation 4.21 can be estimated by applying Simple Beam Theory (SBT) to the longitudinal strain. According to Pérez-Galmés [87], this approach results in fracture toughness values within 2% of results obtained from strain gauges and Digital Image Correlation (DIC). This results in an expression that does not depend on the strains, but rather on the distances between the load application point and the clamp tool (L), and the distance between the section $S - S^{'}$ and the clamp tool (Ls), so that the final equation becomes:

$$J_{II} = \frac{3\left(P\cos\left(\theta_p\right)\right)^2}{5G_{12}b^2h} + \frac{P\cos\left(\theta_p\right)\tan\left(\theta_p - \theta_g\right) - \tan\left(\theta_g\right)}{b} - \frac{E_{11}h}{3}\left(\frac{3}{2}\frac{P\left(L - L_s\right)}{E_{11}bh^2}\right)^2 \tag{4.22}$$

where E_{11} is the Young's modulus in the fiber direction and G_{12} the shear modulus.

Calculation of E_{11} and G_{12}

The longitudinal Young's modulus E_{11} and the shear modulus G_{12} were determined from quasi-static (QS) tensile tests performed on the same flax-epoxy material combination used in this thesis.

To determine E_{11}, tensile tests were conducted along the fiber direction. The stress-strain response exhibited a bi-linear behavior typical of flax-epoxy composites, with an initial linear region followed by a change in stiffness. From the stress-strain curve, two moduli were extracted from the regions indicated by the vertical dashed lines in Figure 4.22a. For the analysis, the 2nd modulus was selected for the calculation of E_{11}, as it represents the material behavior after the initiation of damage, providing a conservative estimate of the material's stiffness under large deformation.

The shear modulus G_{12} was obtained from tensile tests on a $\pm 45^{\circ}$ cross-ply laminate. The shear modulus G_{12} was calculated in the strain range from 2000 to 6000 micro-strain as indicated by the vertical dashed lines in Figure 4.22b.

Angle Determination

For each specimen, the angle was determined at every measured delamination length using the image processing software ImageJ. The images obtained during testing were analyzed to measure the angle relative to the loading block. This process involved manually tracing the edge of the loading block in ImageJ to define the angle. Then for each delamination length, the change in angle from the initial, undeformed position was calculated. These angular changes were used to quantify the rotation of the specimen at the initiation and propagation points of each specimen.

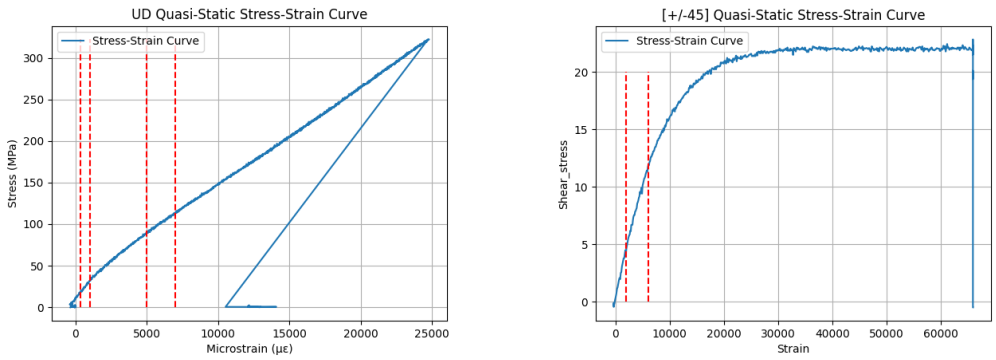

(a) Determination of E_{11}

(b) Determination of G_{12}

Figure 4.22: Stress-strain curves of UD and cross-ply flax epoxy laminates.

In addition to this, for mode II testing, the angle θ_g at the location $S - S^{'}$, as defined in Figure 5.16, was also determined. This angle was measured from the vertical line drawn on the specimen prior to testing at a length L_s and θ_g was calculated relative to the initial, undeformed configuration of the specimen.

Discussion G vs J

The strain energy release rate G, is the recommended analysis method per both ISO and ASTM standards. However, it is fully based on linear elastic fracture mechanics (LEFM), assuming that the energy put into the system is used to propagate the crack and is not to plastically deform the specimen arms. For both mode I & II tests performed in this thesis on flax/epoxy samples, the arms are plastically deformed and invalidate the assumption of LEFM. This is where the J-integral, derived on non-linear fracture mechanics, provide an alternative approach to calculate the fracture toughness in the presence of large Fracture Process Zones (FPZ) and large displacements. However, the J-integral for mode I & II, make assumptions that do not fully capture all aspects of plasticity in the specimens, therefore the calculated fracture toughness values should mainly be used for comparative evaluation of the aging states. The assumption in mode II, of the difference between θ_g and θ_g', get larger as the crack propagates and might influence results towards the end of propagation.

A comparison of the Strain Energy Release Rate (SERR), calculated using the compliance method with large displacement corrections, and the J-integral on fiberglass/epoxy samples (h = 4 mm) yielded remarkably similar results, differing by only 0.97% $\pm$ 0.92% [84]. This close agreement highlights how the correction factors for the SERR closely match the J-integral. The J-integral rooted in non-linear fracture mechanics should capture more of the plasticity effects for non-linear fracture mechanics scenarios where traditional LEFM assumptions fail.

For mode II, data from W. Tu [88] on unidirectional carbon/epoxy tested using the End-Loaded Split (ELS) method provides a comparison between SERR and the J-integral, as shown in Figure 4.23. A noticeable difference between the two methods is observed in this case. This discrepancy is likely due to the J-integral's ability to apply force corrections, ensuring that the component of the force used in the calculation is adjusted to account for the applied angle. Furthermore, more plasticity effects are accounted for in the FPZ. This adjustment allows the J-integral to more accurately reflect the fracture mechanics in cases where deflections become larger and non-linear effects are more pronounced, thereby providing a refined estimation of fracture toughness in mode II.

4.3.3. Fatigue

To analyze fatigue behavior, the crack growth rate is typically plotted against $\Delta\sqrt{G} = (\sqrt{G_{max}} - \sqrt{G_{min}})^2$. However, due to the plastic deformation observed during testing, G_{min} becomes negative, making it impossible to calculate $\Delta\sqrt{G}$.

An alternative approach is to use $\Delta G = G_{max} - G_{min}$, which avoids the issue of square-root calculations with negative values. For direct comparison with the J-integral results, however, J_{min} would also be required. The angle measurements for the specimens at minimum displacement are unavailable, as

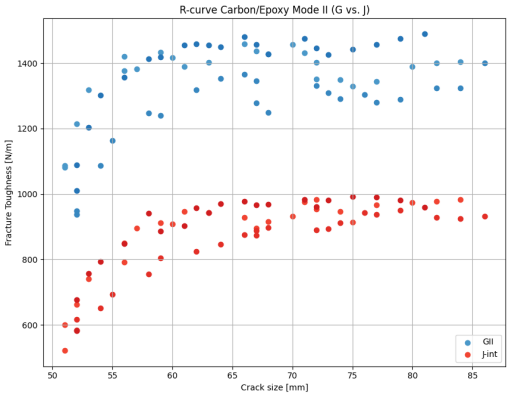

Figure 4.23: Comparison of SERR to J-integral for Carbon/Epoxy mode II ELS.

this aspect of the analysis was not initially anticipated. Therefore, the fatigue behavior will be plotted as crack growth rate against G_{max} and J_{max}

The crack growth rate is determined by first fitting a power-law function to the crack length versus cycle data and then calculating its derivative. This approach allows for a continuous assessment of crack growth rate, providing insight into the rate of crack propagation in response to fatigue loading.

The maximum fracture toughness for each cycle is calculated using Equations 4.3, 4.6, 4.20, and 4.22 as previously described, with modifications to incorporate the maximum force and displacement values for each cycle. Compliance is calculated using Equation 4.23, which utilizes the maximum and minimum displacement (δ_{max} and δ_{min}) and force (P_{max} and P_{min}) values within each cycle:

$$C = \frac{\delta_{max} - \delta_{min}}{P_{max} - P_{min}} \tag{4.23}$$

For the calculation of the J-integral, the change in angle at the load block was determined using the same principle as that used to determine the continuous crack length from a series of selected images, as described in Section 4.3.1. For mode II, the angle θ_g was calculated by averaging several measurement points.

4.3.4. Analysis of Variance (ANOVA)

To assess the impact of aging on fracture toughness, a One-Way ANOVA was conducted on the test results. ANOVA, or Analysis of Variance, is a statistical method used to compare means across multiple groups, helping to determine if observed differences are statistically significant.

In this analysis, fracture toughness was set as the dependent variable, with the aging state as the independent variable. Prior to applying ANOVA, the groups were checked for normality using the Shapiro-Wilk test to ensure they fit a normal distribution. Additionally, to verify the assumption of homogeneity of variance, a requirement for ANOVA, Levene's test was performed to determine if there were significant differences in variances across the aging states.

If both tests confirmed normality and homogeneity of variance, the ANOVA results were evaluated for statistical significance. The Null hypothesis, is rejected if the p-value is found to be less than 0.05, meaning that there is a less than 5% probability that the observed differences in fracture toughness between aging states occurred due to random variation alone.

4.3.5. Surface Roughness

After testing, the fracture surfaces were examined using the surface roughness function on a Keyence VK-X1000 Confocal Laser Scanning Microscope (Figure 4.24a), resulting in a 3D surface plot used for the analysis shown in Figure 4.24b. This analysis aimed to investigate whether aging impacts the

fracture surface roughness and, consequently, whether it influences the crack propagation path. A longer and rougher crack path can indicate higher energy absorption during propagation, as the crack likely encountered greater resistance and had to navigate around microstructural obstacles, enhancing the fracture toughness.

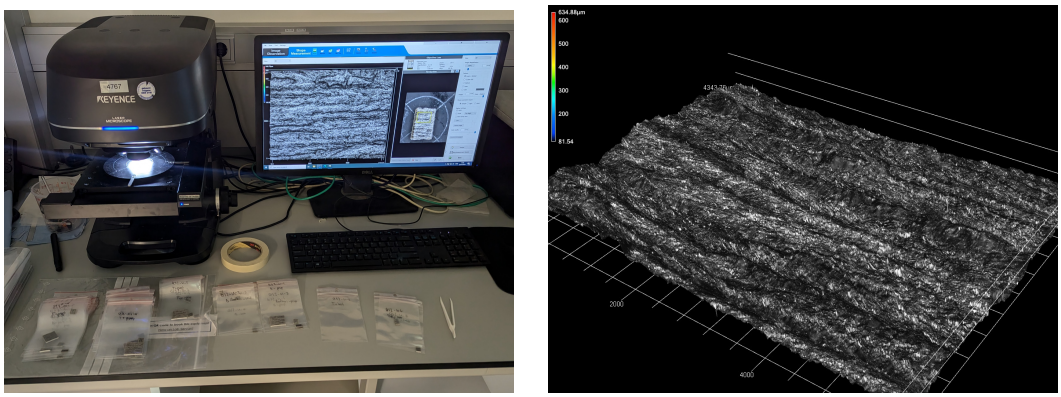

(a) Keyence VK-X1000 Confocal Laser Scanning Microscope **(b)** 3D surface topography

Figure 4.24: Keyence setup and obtained 3D surface topography used for surface roughness analysis.

The arithmetical mean height S_a is a key parameter in surface roughness analysis, particularly relevant for 3D surface topography measurements. It quantifies the average height deviations of a surface's topography within a specified area. The S_a value is defined mathematically as:

$$S_a = \frac{1}{A} \int \int_A |z(x, y)| \, dx \, dy$$

where:

- A is the total area being analyzed,
- $z(x, y)$ represents the height of the surface at each point (x, y).

A higher S_a value indicates a rougher surface, suggesting that more energy was dissipated as the crack propagated.

For each testing condition, three specimens were fully opened to split them in half, creating separate top and bottom specimen arms. For mode I testing, samples were cut from both the initiation and propagation regions of each arm. These samples were then stored individually in ziplock bags and labeled accordingly. The prepared samples were subsequently analyzed for surface roughness measurements and examined using the Scanning Electron Microscope (SEM).

4.3.6. Scanning Electron Microscope (SEM)

To examine the fracture surfaces in greater detail, the samples were analyzed using Scanning Electron Microscopy (SEM). SEM is ideally suited for studying fracture surface characteristics, as it produces high-resolution images with a large depth of field, enabling a detailed capture of the complex topography of the fracture surface.

SEM operates by directing a focused electron beam onto the fracture surfaces. As the electrons interact with atoms in the material, they produce various signals, which can be used to gather different types of information. For imaging the fracture surfaces, the primary focus is on detecting secondary electrons. These low-energy electrons do not penetrate deeply into the surface, making them highly sensitive to surface topography and ideal for capturing detailed images of the fracture features.

Figure 4.25 shows the SEM setups used in this study. Initially, the SEM at the Faculty of Civil Engineering was chosen for its capability to operate under low- and no-vacuum conditions. This choice was based on the hypothesis that high-vacuum conditions could potentially introduce additional damage to

the specimens by accelerating moisture removal. However, due to scheduling conflicts, it became necessary to use an alternative high-vacuum SEM setup. Upon comparing the images, it was concluded that, for the purpose of analyzing damage patterns on the fracture surfaces between aged and unaged specimens, the vacuum level did not significantly impact the results.

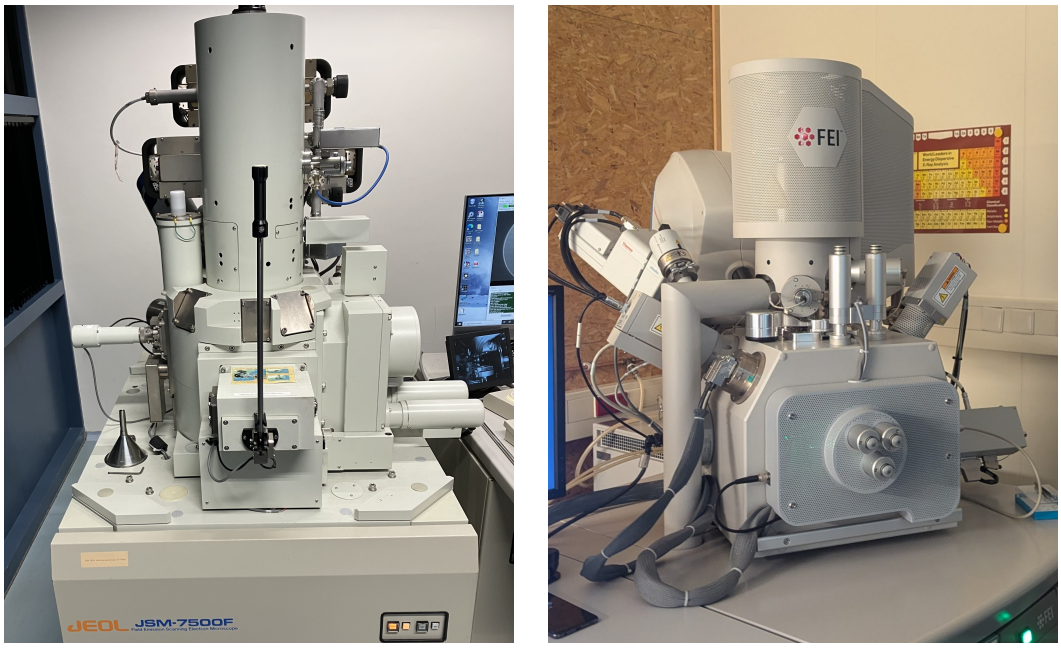

(a) SEM Aerospace faculty **(b)** SEM Civil faculty

Figure 4.25: SEM setup at civil and aerospace engineering faculties.

To assess the effects of aging on fracture surfaces, the SEM images were analyzed based on several key characteristics to evaluate the effect of aging on the damage mechanisms:

- **Fiber-Matrix Adhesion:** Observations focused on the degree of bonding between fibers and the surrounding matrix material. Strong adhesion would typically indicate minimal aging effects, while signs of fiber pull-out or gaps at the interface may suggest aging-induced degradation.
- **Matrix Residue on Fibers:** The presence and distribution of matrix residue on fiber surfaces was examined. Higher levels of residue on fibers post-fracture often indicate cohesive fracture within the matrix, while lower residue levels might suggest fiber-matrix debonding associated with aging.
- **Matrix Regions:** Matrix regions and patches were evaluated for size, fiber imprints and frequency, to see if aging has an effect.
- **Damage Patterns and Fracture Topography:** Broader damage patterns, like differences between mode I & II or top and bottom surfaces, were analyzed to identify differences between aged and unaged specimens.

This structured analysis allowed for a comparative evaluation of the microstructural effects of aging on the fracture surfaces.

5

Results and Discussions

This chapter presents and discusses the results obtained for mode I & II, quasi-static and fatigue fracture toughness testing of cyclic aged and unaged specimens. The aim is to evaluate how or if cyclic aging influences the fracture toughness of flax fiber reinforced epoxy.

5.1. Mode I QS

Figure 5.1 shows the force-displacement behavior of all tested specimens, with the displacement data shifted so that the x-intercept of the linear regression, performed on the portion of the curve between 25% and 75% of the maximum load, aligns with the origin. This adjustment ensures that the linear region starts from zero displacement, enabling consistent comparison of the specimens. It can be observed that during the initial NPC loading cycle, the material does not exhibit linear behavior. However, during the second PC loading cycle, the material demonstrates a highly linear response. This is a known phenomenon in FFRP, where on reloading, the material follows a different and more linear path upon reloading [89].

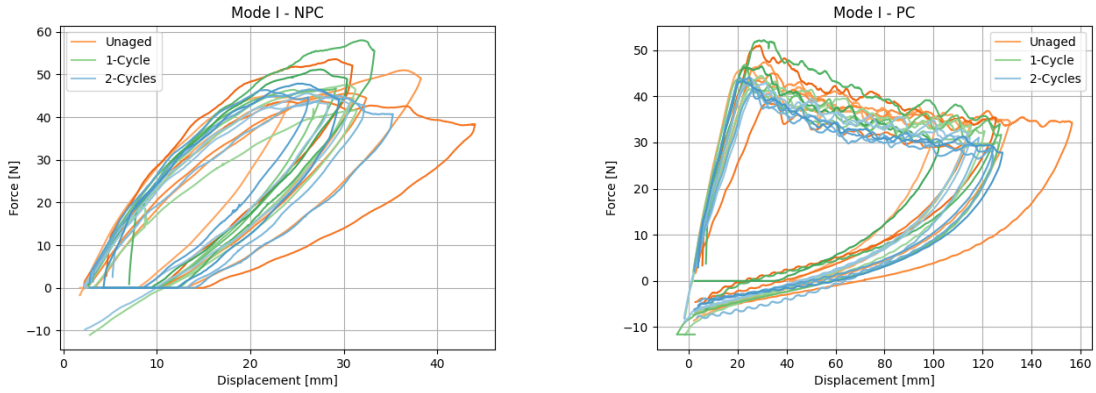

(a) NPC specimens

(b) PC specimens

Figure 5.1: Force-displacement curves mode I fracture toughness testing.

Both the NPC and PC specimens do not return to the origin, indicating permanent deformation as a result of the large displacements required to initiate and propagate the crack. The PC curves demonstrate an initial linear elastic response up to approximately 40-50 N, after which the load gradually decreases, reflecting steady crack propagation. During unloading, the specimens return to their initial position, showing a temporary negative force of approximately -10 N when the force-displacement data recording stopped. After remaining in this position for some time, the specimens exhibit relaxation and return to around -7 N. The behavior, exhibited by the PC force-displacement curve, corresponds to findings

by similar studies on fracture toughness summarized in Table 2.1. Figure 5.2 shows an overlaid image of the specimen in the fixture, illustrating its position both before testing and at its maximum displacement. This comparison highlights the extent of deformation experienced by the specimen during the test. Resulting in the permanently deformed specimens, as shown in Figure 5.3.

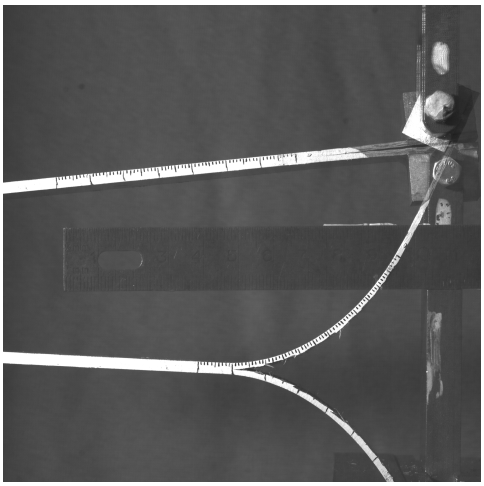

Figure 5.2: Specimen QS1-A1-4, before test and at max displacement position in test.

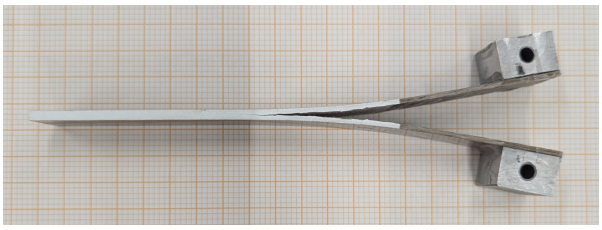

Figure 5.3: Final deformed DCB specimen after testing.

According to ASTM D5528 [36], specimen arms are classified as permanently deformed if restoring them to their original shape requires more than manual pressure applied with an index finger. Specimens exhibiting such deformation are considered invalid for fracture toughness evaluation, as linear-elastic fracture mechanics (LEFM) no longer apply. In the case of the tested specimens, the curvature can be removed manually; however, it is important to note that ASTM D5528's criteria are primarily based on the behavior of glass and carbon fiber composites, which may respond differently compared to the flax-epoxy materials used in this study and require more force to remove the curvature.

From the test data and crack length measurements obtained from the images during testing, the mode I fracture toughness, G_I and J_I, were calculated using Equations 4.3 and 4.20. The calculated results are presented as R-curves in Figure 5.4.

In Figure 5.4b, it can be observed that the initial NPC fracture toughness for one unaged specimen is shown as zero. This is due to the absence of the image corresponding to this test point, resulting in the inability to determine the angle required for calculating the J-integral. PC fracture toughness values used in the remainder of the analysis were calculated for all specimens without any issues.

Comparing both graphs, it can be seen that the initiation fracture toughness is considerably lower using the J-integral compared to the G, with the J-integral increasing more rapidly in fracture toughness ending up with similar propagation fracture toughness but showing less signs of plateauing. The J-integral was developed within the framework of non-linear fracture mechanics, making it more suitable for accounting for the plasticity and large deformations observed in the tests. Consequently, the subsequent analysis and results are presented using the J-integral to better capture the material behavior under these conditions.

In the following sections, results are presented for fracture toughness at initiation and propagation. For

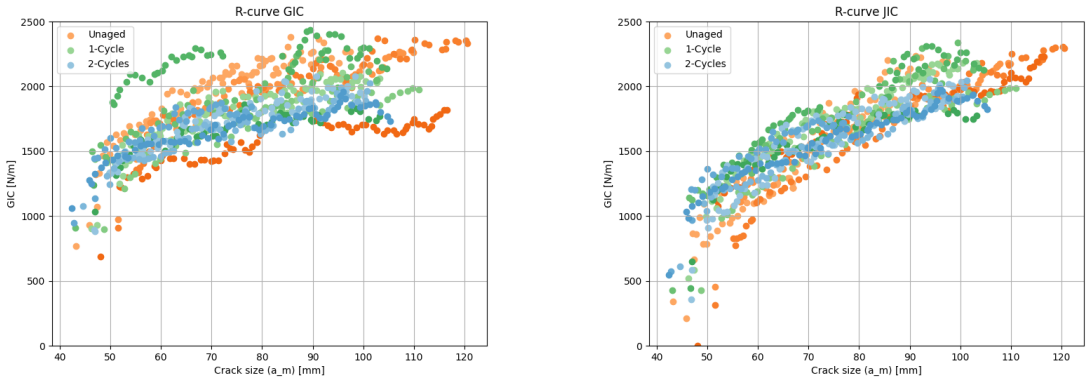

(a) SERR (G)

(b) J-integral

Figure 5.4: Mode I R-curves comparing fracture toughness evolution using SERR (G) and the J-integral.

initiation calculations, specimens A2-4 and U-5 were excluded, as they were pre-cracked beyond the acceptable range. For propagation, data points at 90–95 mm were excluded for specimens U-1, A1-7, and A2-5, as the crack had not propagated to this length. At the 70–75 mm propagation interval, all specimens met the criteria and were included in the analysis. By analyzing fracture toughness at key crack lengths, insights are provided into how aging cycles influence the material's resistance to crack growth.

5.1.1. Effect of Hygrothermal Aging on Fracture Toughness

This section specifically examines the impact of hygrothermal aging on the fracture toughness of flax fiber-reinforced composites, comparing the initiation and propagation toughness values across unaged, 1-cycle aged, and 2-cycle aged specimens.

Figure 5.5 illustrates the effect of aging on the pre-cracked (PC) initiation fracture toughness. For the unaged specimens, fracture toughness ranges from 780 to 1120 N/m, with an average value of 934 N/m. These results make sense, comparing them to the values found in the literature, as previously presented in Table 2.1. The unaged initiation values have a wide spread, indicating considerable variability within the flax fiber specimens.

After one aging cycle, the fracture toughness increases to an average of 1108 N/m, showing a notable increase compared to the unaged specimens. However, after the second aging cycle, there is no further change, with the average remaining steady at 1107 N/m. This stabilization suggests that the primary effect of aging on fracture toughness may occur during the initial cycle, with subsequent cycles having minimal impact on the PC initiation fracture toughness.

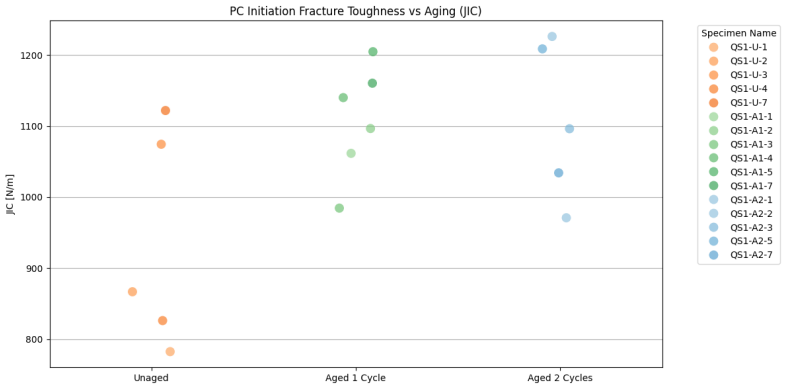

Figure 5.5: Effect of hygrothermal aging on mode I pre-cracked initiation fracture toughness.

An ANOVA analysis was conducted on the initiation fracture toughness data with a significance threshold of $p < 0.05$. Before performing the analysis, all groups were successfully checked for normality and equal variance using the Shapiro-Wilk and Levene's tests, respectively. The results indicate that the differences in fracture toughness between the aging states are statistically significant at initiation, with a p-value of 0.048.

The effect of aging on fracture toughness was also assessed at later stages of crack propagation by averaging fracture toughness values within the intervals of 70–75 mm and 90–95 mm crack lengths. These results are presented in Figure 5.6. All aging states show a wide range of fracture toughness values, making it difficult to distinguish a definitive trend. Aged specimens generally exhibit a slightly higher fracture toughness compared, to the unaged specimens, except for the 2-cycle aged specimens from 90-95 mm of crack length.

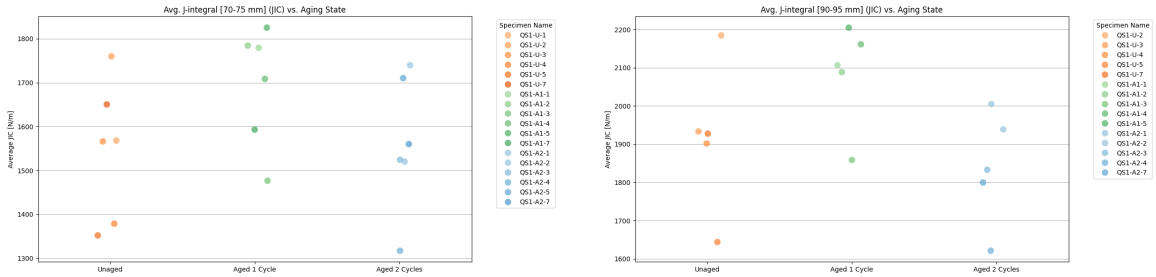

(a) crack length 70-75 mm

(b) crack length 90-95 mm

Figure 5.6: Effect of hygrothermal aging on mode I propagation fracture toughness.

An ANOVA analysis was performed, to look for statistically significant findings, yielding p-values of 0.20 for the 70–75 mm interval and 0.084 for the 90–95 mm interval, indicating that the differences in fracture toughness between aging conditions during propagation are not statistically significant.

In summary, the results for mode I quasi-static (QS) fracture toughness testing reveal key insights into the effects of hygrothermal aging on the fracture toughness of flax fiber-reinforced epoxy composites. Initiation fracture toughness showed a statistically significant increase after just one aging cycle. A second aging cycle did not result in further increases, suggesting that most substantial changes occur during initial exposure.

Propagation fracture toughness, on the other hand, did not show a statistically significant change across aging conditions, indicating that the initiation phase is more susceptible to the effects of aging. This difference may be attributed to the presence of the starter crack, which allows moisture to infiltrate and impact the initiation region of the specimens more directly. This exposure could lead to increased ductility in both the fibers and matrix, enhancing the material's ability to absorb energy during fracture initiation.

5.1.2. Effect of Temperature on Fracture Toughness

At the start of each test, the temperature in the laboratory was recorded, as flax fibers are known to be sensitive to temperature variations. This section reports the effect of the laboratory temperature on fracture toughness.

Figure 5.7 illustrates the relationship between initiation fracture toughness and temperature, with different colors representing the various aging states of the specimens. A slight downward trend might be observed, indicating that higher laboratory temperatures might correspond to lower initiation fracture toughness values.

Figure 5.8, presents the effect of laboratory temperature on the propagation fracture toughness. Interestingly, a slight opposite trend looks to occur, where the fracture toughness increases with an increase of temperature.

From these results, there is no clear and obvious trend on the implications of temperature on the fracture toughness over the temperature range of 20-27 °C. The differences, seen with temperature, may be

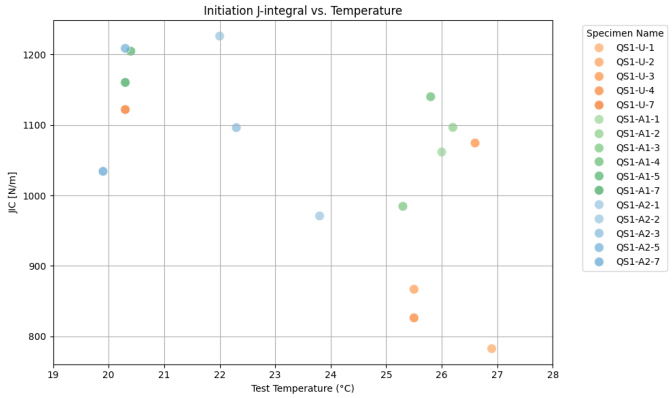

Figure 5.7: Effect of test temperature on mode I initiation fracture toughness.

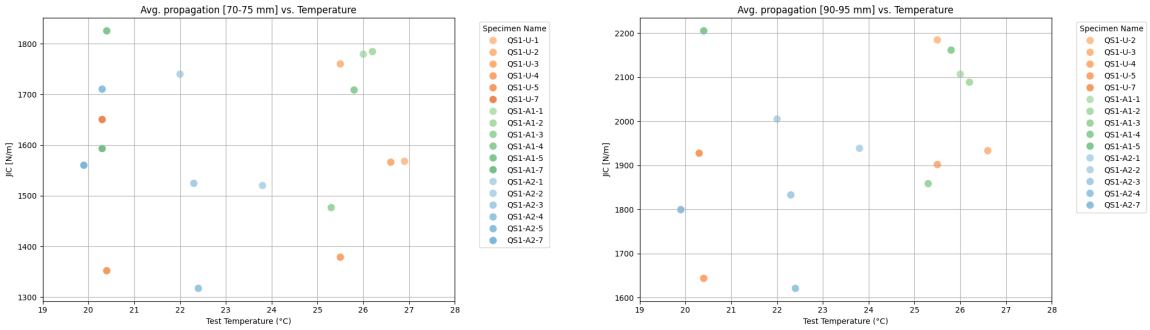

(a) Crack length 70-75 mm

(b) Crack length 90-95 mm

Figure 5.8: Effect of test temperature on the average mode I propagation fracture toughness.

attributed to natural variability within the samples rather than temperature alone. It would be expected that testing at higher temperatures leads to a more ductile material that might result in higher fracture toughness. For a better understanding of how temperature affects the fracture toughness, testing would have to be conducted in a controlled climate chamber with precise temperature control.

5.1.3. Effect of Thickness on Fracture Toughness

The effect of specimen thickness, and consequently the effect of the different plates used, was investigated. The influence of thickness on initiation fracture toughness is shown in Figure 5.9. No clear trend is observed, suggesting that thickness does not significantly affect the initiation fracture toughness in these tests.

The effect of thickness on the propagation fracture toughness was also investigated. As shown in Figure 5.10, again no clear trend is observed, further suggesting that this thickness range and the slight variations between the plates does not affect the results.

5.1.4. Fractography

This section discusses the fractography results obtained from mode I QS testing. Figure 5.11 illustrates the color variations between unaged surfaces (left), 1-cycle aged specimens (middle), and 2-cycle aged specimens (right). Aging appears to lighten the color of both outer and inner surfaces, making the fiber texture more visible. The color differences, observed in the top two 1-cycle aged specimens, is due to the specimens originating from different plates. The fracture surfaces themselves do not exhibit any clear differences to the naked eye.

Using the Keyence confocal microscope, the images in Figure 5.12 were obtained and subsequently used for surface roughness measurements. These images reveal similar fracture patterns for both aged and unaged specimens. The fracture surfaces appear fairly rough, featuring broken fibers and

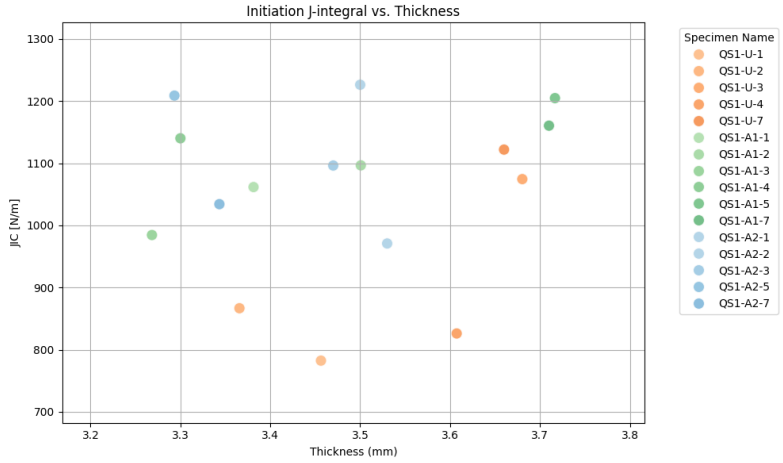

Figure 5.9: Effect of specimen thickness on the mode I initiation fracture toughness.

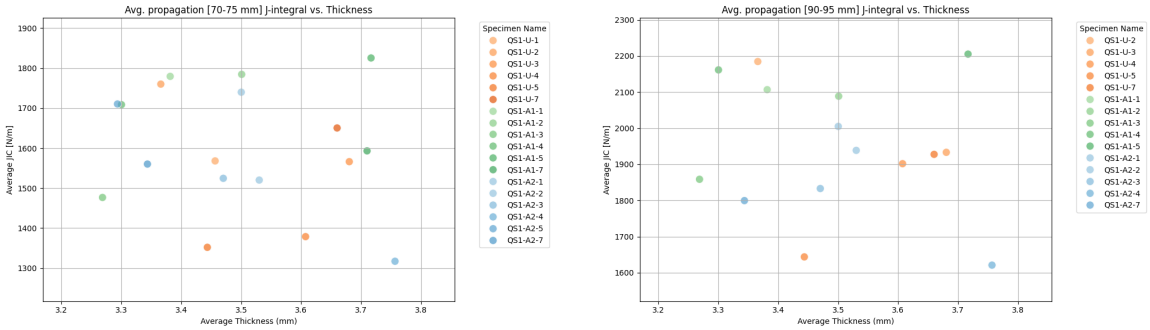

(a) Crack length 70-75 mm

(b) Crack length 90-95 mm

Figure 5.10: Effect of specimen thickness on the average mode I propagation fracture toughness.

Figure 5.11: Mode I fracture surfaces, unaged (left), 1-cycle (middle), 2-cycle (right).

fiber-bundle imprints, with the twist within the fiber bundles also visible.

Finally, the specimens were examined using SEM, as shown in Figure 5.13. The images on the left depict unaged specimens, while those on the right represent 1-cycle aged specimens. Distinct patterns observed include imprints of individual fibers and fiber bundles, broken fibers, fiber pullout, and matrix-rich regions.

The surfaces of loose fibers and fibers within the bundles appear mostly clean from matrix residue, indicating an initial weak fiber-matrix adhesion in unaged specimens that result in clean pull-out from the matrix. A closer examination of the differences between aging states reveals some variance, the

(a) Unaged initiation **(b)** 1-cycle aged initiation **(c)** 2-cycle aged initiation

Figure 5.12: Images from Keyence microscope of mode I quasi-static testing fracture surfaces.

unaged specimens exhibit larger smooth matrix regions, as shown in Figure 5.13c, however smaller regions of this are also found in aged specimens as is shown on the right side of Figure 5.13b.

5.1.5. Surface Roughness

The surface roughness of QS mode I specimens was analyzed using a Keyence VK-X1000 Confocal Laser Scanning Microscope. To evaluate both initiation and propagation regions, surface roughness measurements were taken on the top arm of each specimen. The bottom arm was not analyzed, as the setup is symmetric about the specimen's mid-plane, allowing surface roughness observations from the top arm to represent the entire specimen. The results are shown in Table 5.1.

Table 5.1: Surface roughness (Sa) for mode I QS specimens across aging conditions.

	Unaged	1-Cycle	2-Cycles
Top arm initiation (Sa)	79.57 $\pm$ 6.64 μm	99.34 $\pm$ 4.91 μm	84.48 $\pm$ 7.54 μm
Top arm propagation (Sa)	75.87 $\pm$ 11.66 μm	92.59 $\pm$ 4.04 μm	75.19 $\pm$ 13.27 μm

Examining the surface roughness results, initiation roughness values appear to be slightly higher than those observed during propagation. For both initiation and propagation, the first aging cycle led to a noticeable increase in roughness compared to unaged specimens, suggesting that initial aging may induce surface changes contributing to increased roughness. This observation aligns with the increase in fracture toughness observed after aging. However, after a second aging cycle, roughness values decrease again, which may indicate that prolonged aging leads to a reduction in surface roughness, although this trend does not correlate with changes in fracture toughness. Furthermore, the results exhibit significant variability, introducing uncertainty and limiting the ability to draw definitive conclusions.

5.1.6. Summary of Findings

Extensive plastic deformation in the specimens invalidates the assumptions of Linear Elastic Fracture Mechanics (LEFM). Although the J-integral provides a more accurate depiction of fracture toughness, it is not without limitations, and thicker specimens could yield different results. For comparative evaluation of aging effects, however, the J-integral remains valuable for assessing fracture toughness behavior before and after aging.

The effect of hygrothermal aging on fracture toughness is most pronounced in the initiation region, where the average fracture toughness increased by nearly 19% after one aging cycle. Subsequent aging cycles did not further influence fracture toughness. In the propagation stage, fracture toughness did not show a statistically significant difference after aging, although a slight increase was observed. This increase is thought to result from plasticization of the matrix and fibers. Unpublished data of the D-STANDART project on carbon-fiber epoxy samples showed an opposite trend where the fracture toughness decreased after aging, this may be due to the fact that aging was able to have a more pronounced effect on the fiber-matrix interface and reduce effects of fiber bridging. Fractography of the fracture surfaces did not reveal clear distinctions between aged and unaged specimens, the pri-

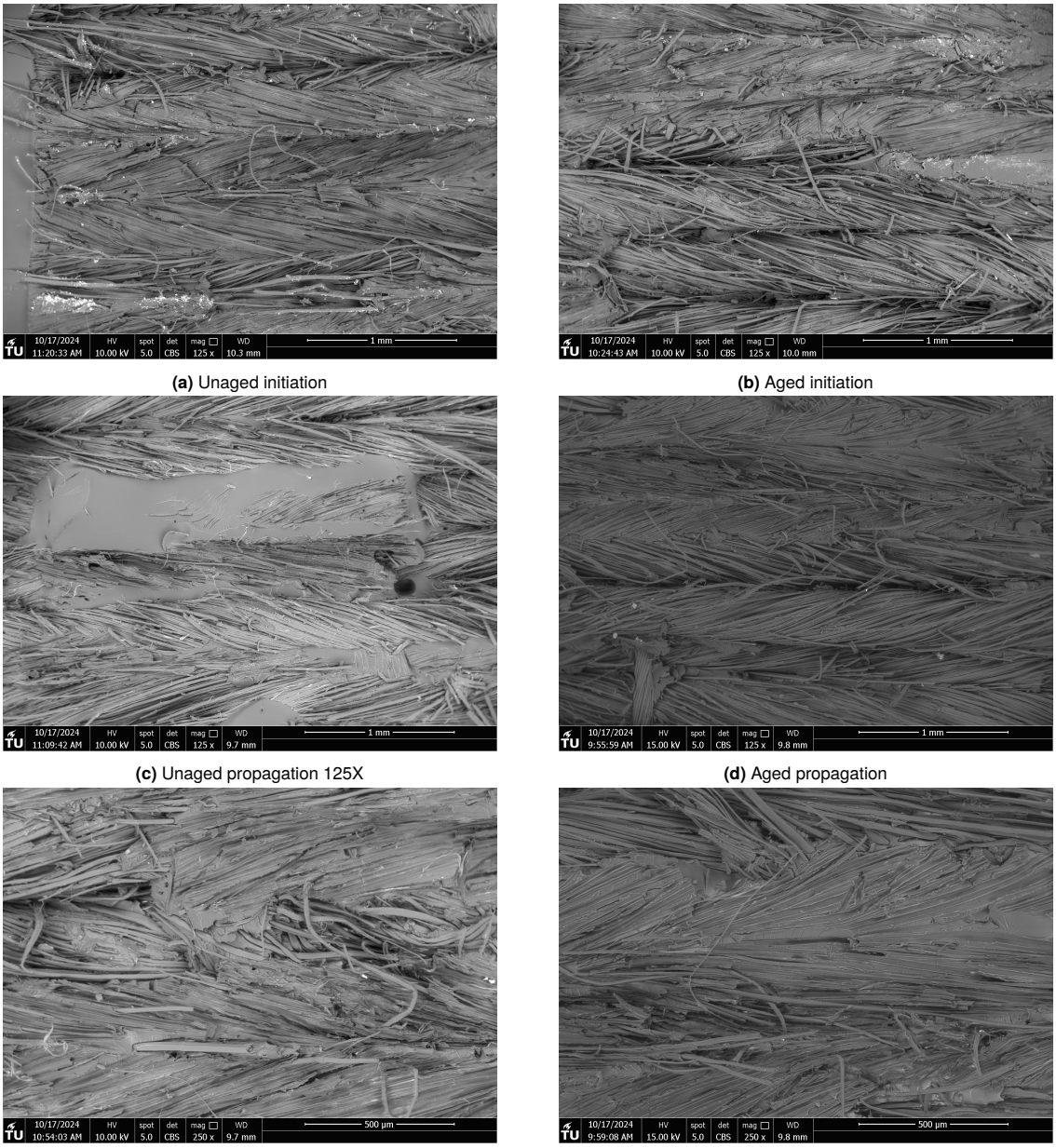

(a) Unaged initiation

(b) Aged initiation

(c) Unaged propagation 125X

(d) Aged propagation

(e) Unaged propagation 250X

(f) Aged propagation 250X

Figure 5.13: SEM images of fracture surfaces from mode I quasi-static testing.

mary differences observed were a color change in the specimens and slightly larger matrix patches in unaged specimens. The measured roughness of the fracture surface increased after 1 aging cycle, corresponding to the increase of fracture toughness after aging.

5.2. Mode II QS

Figure 5.14, presents the PC force-displacement curves, where the bi-linear behavior typical of flax fiber composites shows up. In contrast to mode I where the curve gradually decreased after reaching a maximum, here the curves exhibit a sharp drop, followed by a force increase, often higher than the initial peak. This behavior indicates that the crack growth in mode II is less stable than in mode I, but it does not exhibit exponential growth. This pattern repeats until the test is stopped at either the maximum travel of the test bench or when the crack was observed to have grown within 10 mm of the clamp.

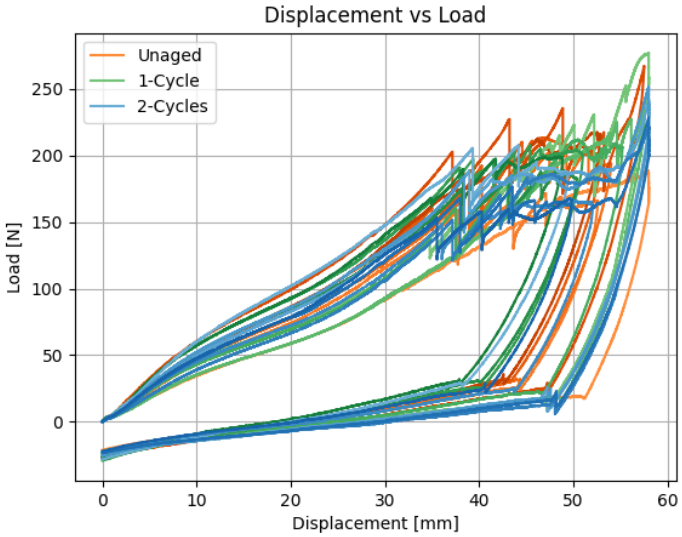

Figure 5.14: Force-displacement curves mode II fracture toughness testing.

The high peak forces observed at maximum displacement result from the sliding fixture reaching its limit, preventing further movement. During image analysis, it was verified that this occurred only after the crack had propagated to within 10 mm of the clamp, ensuring that the fixture limitations did not interfere with the crack growth measurements. During unloading of the ELS specimens, the force initially decreases rapidly before reaching a distinct point where it begins to stabilize. Observations during testing indicated that this stabilization occurred when the sliding ELS fixture started to move back to its original position. Once the specimens returned to their original position, the force registered within a range of -20 to -30 N, suggesting substantial plastic deformation. As with mode I specimens, some relaxation was observed after the specimens returned to their initial position. Figure 5.15 shows an overlaid image of an ELS specimen both before testing and at maximum displacement, illustrating the extent of deformation during testing. Figure 5.16 shows the resulting plastic deformation in the specimen after testing.

These figures clearly indicate that the assumptions of LEFM are not valid for these tests. Using the data and images obtained during the experiments, both G_{II} and J_{II} were calculated using Equations 4.6 and 4.22. The resulting R-curves for mode II fracture toughness are presented in Figure 5.17.

The graphs clearly show that the two analysis methods, G_{II} and J_{II}, yield significantly different results. This difference can be attributed to the J-integral's ability to account for plasticity effects and incorporate corrections for the applied force based on measured angles. Given these advantages, the subsequent analysis presents results using the J-integral, as it better captures the material's plastic behavior during testing.

5.2.1. Effect of Hygrothermal Aging on Fracture Toughness

Figure 5.18 presents the initiation fracture toughness results for QS mode II testing, categorized by each aging condition.

The unaged specimens exhibit a wide range of fracture toughness values, from approximately 800 to

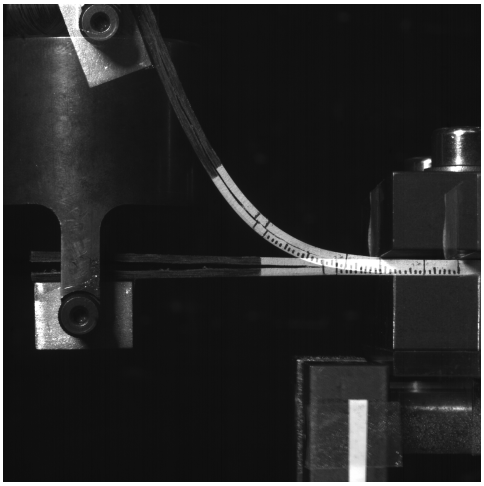

Figure 5.15: Specimen QS2-U-2, prior to testing and at maximum deflection.

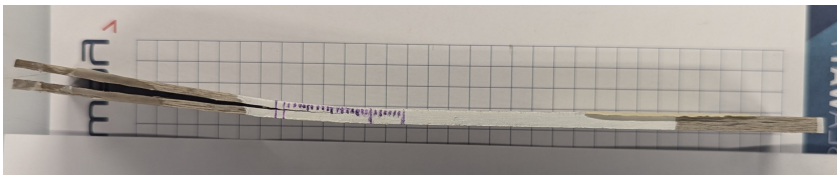

Figure 5.16: Final deformed ELS specimen after testing.

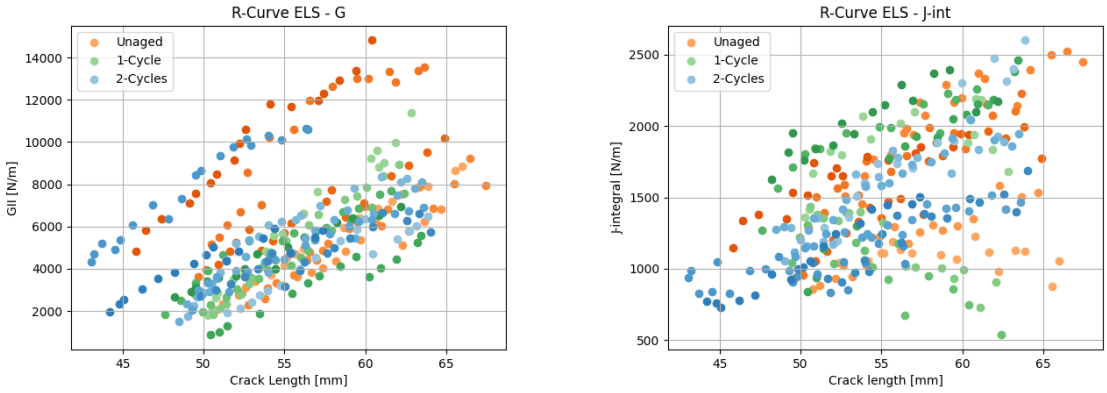

(a) SERR (G)

(b) J-integral

Figure 5.17: Mode II R-curves comparing fracture toughness evolution using SERR (G) and the J-integral.

1550 N/m, with most values clustering between 800 and 1200 N/m. This spread indicates substantial variability in initial fracture toughness, potentially arising from inherent differences in material properties or initial microstructural variations within the specimens.

After one aging cycle, the range of fracture toughness remains similar, but the variance between specimens appears more pronounced, suggesting that aging may introduce additional factors influencing fracture behavior. However, this distribution does not display a clear trend in either increasing or decreasing toughness as a direct effect of the aging process.

For specimens aged over two cycles, the fracture toughness values fall within a narrower range of approximately 800 to 1300 N/m, indicating reduced variability compared to both unaged and 1-cycle aged specimens. This clustering may suggest a stabilization effect from the extended aging, potentially leading to more uniform fracture toughness characteristics across the sample set.

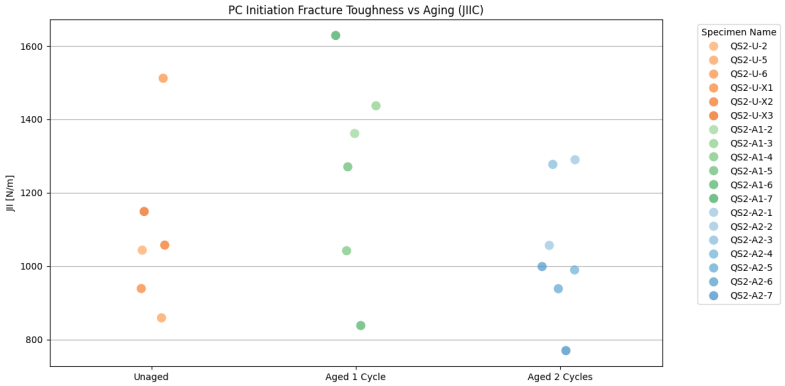

(a) J-integral

Figure 5.18: Effect of hygrothermal aging on mode II pre-cracked initiation fracture toughness.

Propagation values have been calculated over a range of 55-60 mm and results are shown in Figure 5.19. Here we see similar results as for the initiation, as there does not seem to be a clear upward or downward trend for propagation fracture toughness.

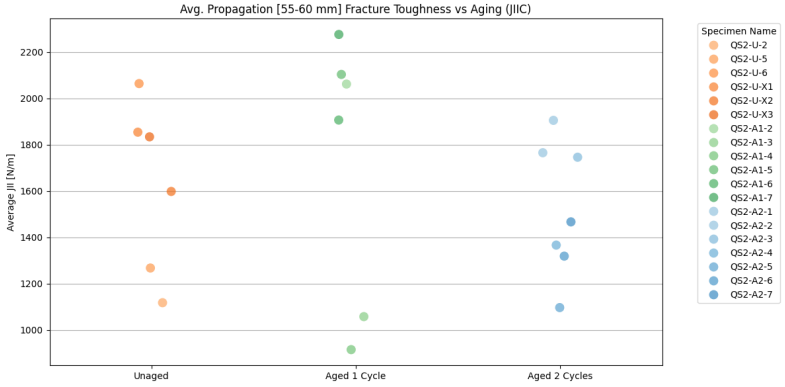

(a) J-integral

Figure 5.19: Effect of hygrothermal aging on mode II propagation fracture toughness.

Conducting an ANOVA analysis indicates that the differences between aging states are statistically insignificant, with a p-value of 0.25 for initiation and 0.71 for propagation.

5.2.2. Effect of Temperature on Fracture Toughness

For mode II testing, the laboratory temperatures recorded at the start of each test, ranged from 21 to 27 °C. The results, shown in Figure 5.20, indicate that there is no clear upward or downward trend in fracture toughness values for either initiation or propagation stages in relation to temperature or aging condition. This suggests that within this temperature range, mode II fracture toughness remains relatively unaffected by minor variations in ambient temperature.

5.2.3. Effect of Thickness on Fracture Toughness

Plotting fracture toughness against specimen thickness yields the results shown in Figure 5.21. These plots seem to reveal an upward trend, with fracture toughness increasing as specimen thickness increases for both initiation and propagation stages. This trend may be influenced by the reduced plastic deformation observed in thicker specimen arms. Thicker arms are more rigid, resulting in higher forces required for deformation during loading, which can lead to higher apparent fracture toughness values.

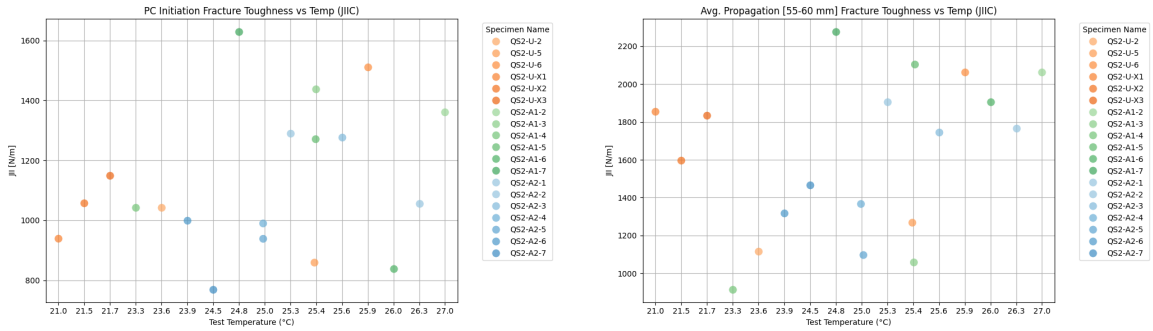

(a) Initiation **(b)** Propagation 55-60 mm

Figure 5.20: Effect of test temperature on mode II initiation & propagation fracture toughness.

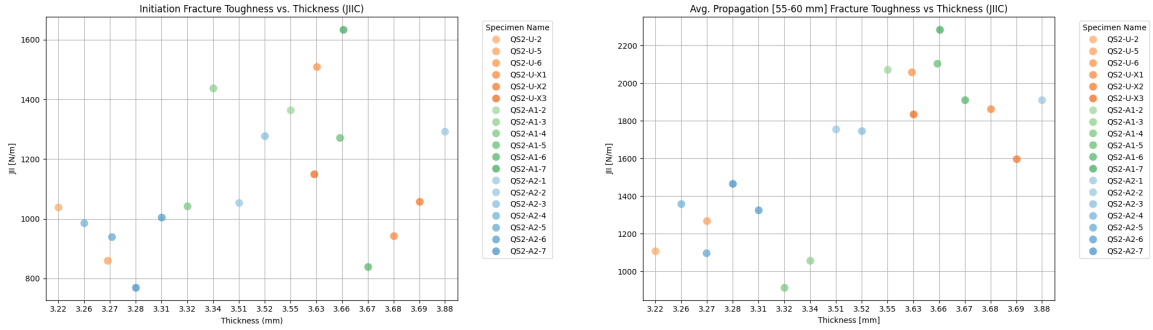

(a) Initiation **(b)** Propagation 55-60 mm

Figure 5.21: Effect of specimen thickness on mode II initiation & propagation fracture toughness.

5.2.4. Fractography

Figure 5.22 shows the exposed fracture surfaces of mode II QS test specimens. The mode I pre-cracking and final splitting regions exhibit distinct failure patterns compared to the darker regions associated with mode II shear crack growth. Furthermore, the specimens are arranged with alternating top and bottom arms, with the shear crack regions on the bottom arms appearing slightly darker than those on the top arms.

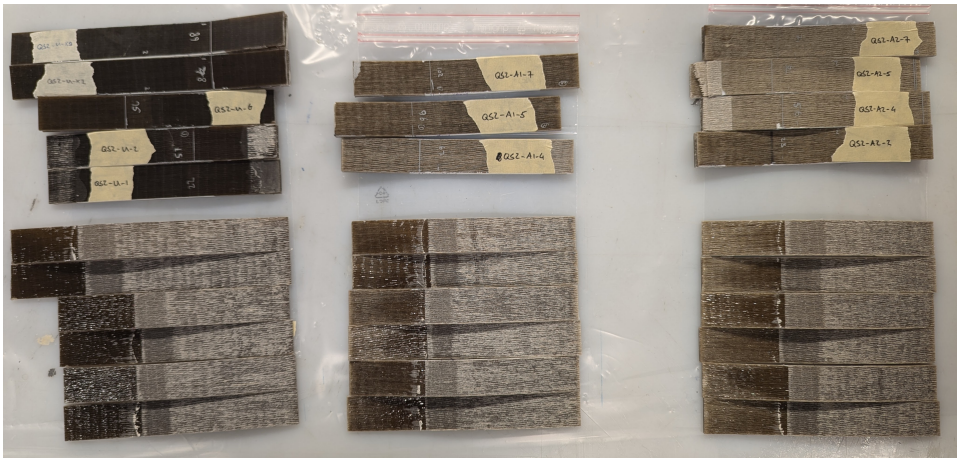

Figure 5.22: Mode II fracture surfaces, unaged (left), 1-cycle (middle), 2-cycle (right).

Placing the specimens under the Keyence microscope produced the images shown in Figure 5.23 for the bottom arm specimens and Figure 5.24 for the top arm specimens. The specimens are arranged from left to right in the order of unaged, 1-cycle aged, and 2-cycle aged. Comparing the images to mode

I, the fiber bundles look to be less intact, which can also be said for the difference between bottom and top mode II surfaces where the top surface looks to have more fibers while the bottom looks to contain more imprints over all the aging states.

Placing the specimens under the Keyence microscope produced the images shown in Figure 5.23 for the bottom arm specimens and Figure 5.24 for the top arm specimens. The specimens are arranged from left to right in the order of unaged, 1-cycle aged, and 2-cycle aged. Compared to mode I, the fiber bundles appear less intact, a trend that is also observed in the differences between the bottom and top surfaces of the arms in mode II. The top surface appears to retain more fibers, while the bottom surface exhibits more fiber imprints across all aging states.

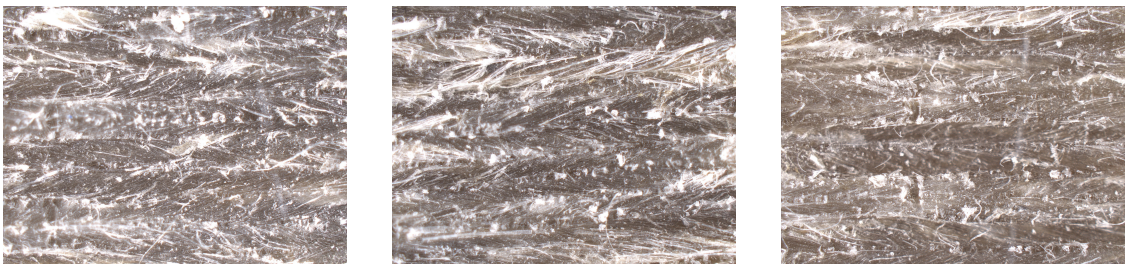

(a) Unaged **(b)** 1-cycle aged **(c)** 2-cycle aged

Figure 5.23: Fracture surface images from Keyence microscope of bottom arms of mode II quasi-static testing.

(a) Unaged **(b)** 1-cycle aged **(c)** 2-cycle aged

Figure 5.24: Fracture surface images from Keyence microscope of top arms of mode II quasi-static testing.

A closer examination of the fibers using SEM produced the images shown in Figure 5.25, which more clearly illustrate the differences between mode I and mode II. Figures 5.25c and 5.25d display an enlarged view of the region between two fiber bundles, revealing cusps—a common fracture characteristic in shearing modes. Similar to mode I, distinct imprints of fibers, broken fibers, and matrix-rich regions are observed. Closer inspection of individual fibers indicates no significant differences between the aging states.

5.2.5. Surface Roughness

The surface roughness results for quasi-static (QS) mode II specimens are presented in Table 5.2. For mode II specimens, measurements were taken from both the top and bottom fracture surfaces, as visual inspection revealed notable differences in surface characteristics between these regions. Since the crack was not able to propagate far in mode II, surface roughness measurements were focused on the central region of the crack growth zone, providing a representative profile of the roughness characteristics for these samples.

The results indicate a similar surface roughness trend for both the bottom and top arms of the specimens. After the first aging cycle, surface roughness decreased slightly but remained fairly consistent. Following the second aging cycle, however, the roughness increased by approximately 10% compared to unaged specimens. This trend contrasts with the observations from mode I testing, where surface roughness increased after the first cycle but returned close to unaged levels after the second cycle. These findings do not agree with the fracture toughness measurements, However it's worth noting that

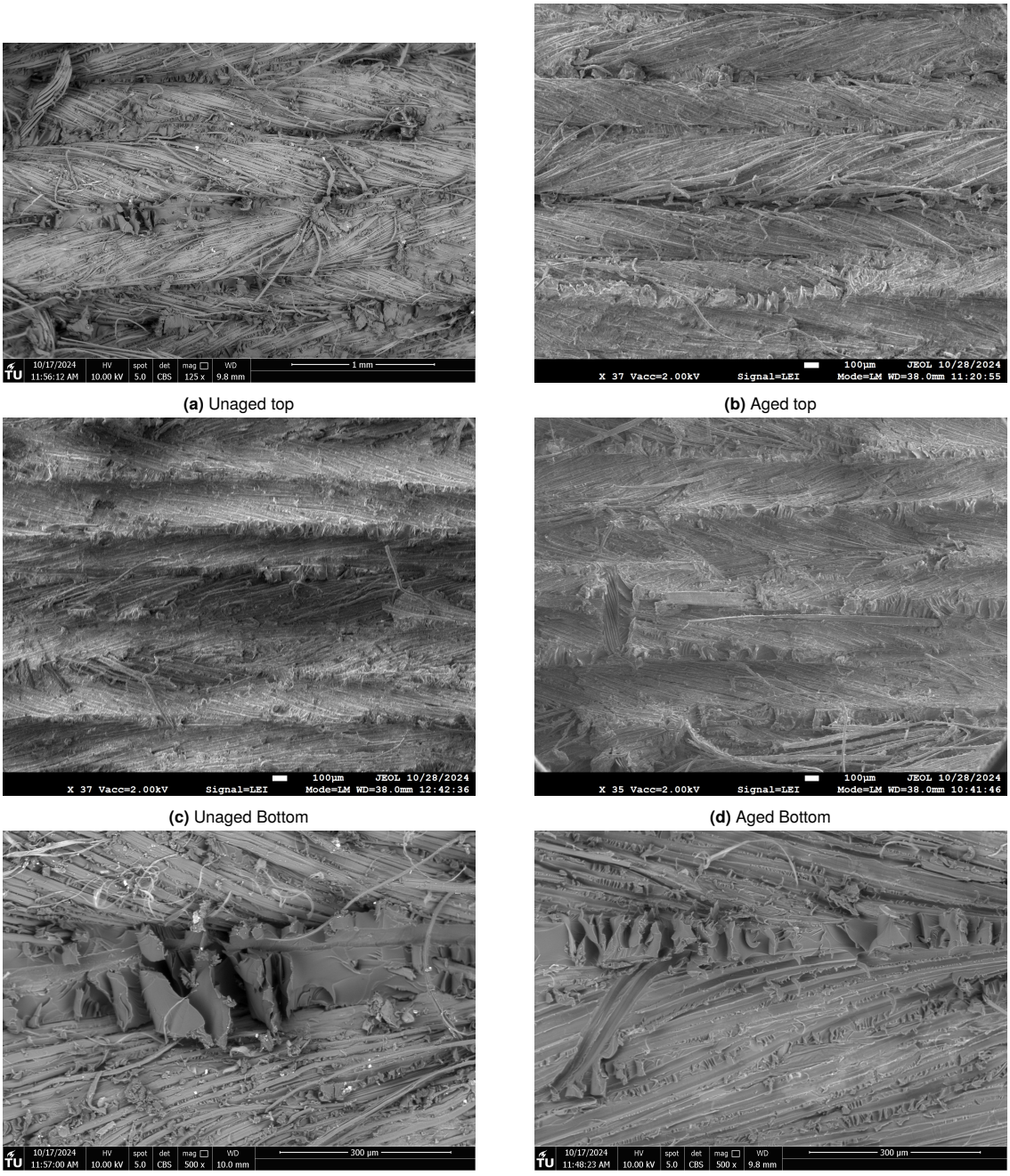

(a) Unaged top

(b) Aged top

(c) Unaged Bottom

(d) Aged Bottom

(e) Unaged top 500X

(f) Aged bottom propagation

Figure 5.25: SEM images of fracture surfaces from mode II quasi-static testing.

the roughness results exhibited high standard deviation, limiting the ability to make definitive conclusions.

5.2.6. Summary of Findings

Mode II quasi-static testing proved challenging due to the severe plastic deformation required to propagate the crack. The recommended ECM method by ISO 15114 could not be applied, and the free length needed to be significantly reduced to enable crack growth. Consequently, only 15 mm of crack growth was achieved, and the J-integral method by Pérez-Galmés [87] was used to calculate fracture toughness at initiation and near the end of the crack growth region. This approach provides an indication of how aging affects fracture toughness in mode II. An ANOVA performed on the obtained results

Table 5.2: Surface roughness (Sa) for mode II QS specimens across aging conditions.

	Unaged (U)	1-Cycle (A1)	2-Cycles (A2)
Bottom arm (Sa)	79.71 $\pm$ 3.66 μm	77.56 $\pm$ 18.86 μm	90.08 $\pm$ 5.76 μm
Top arm (Sa)	81.79 $\pm$ 4.95 μm	77.12 $\pm$ 1.63 μm	87.94 $\pm$ 6.05 μm

indicated that the change in fracture toughness was not statistically significant, with p-values of 0.25 for initiation and 0.71 for propagation. The data showed considerable variance within the aging states, and fracture toughness demonstrated an upward trend with specimen thickness. Further testing with thicker specimens may reveal a different trend, with less energy absorbed in plastically deforming the arms but focussed on propagating the crack. Surface roughness measurements did not align with fracture toughness trends and showed an opposite trend to mode I findings, where roughness only increased after the second aging cycle. Additionally, fractography did not reveal significant differences between aged and unaged specimens.

5.3. Mode I Fatigue

This section presents the results from mode I fatigue testing, conducted on unaged and 1-cycle aged specimens. Due to time constraints, 2-cycle aged specimens were not included in this study. The laboratory temperature during testing remained relatively stable, ranging between 28 and 29.2 °C across the samples. Consistent with mode I quasi-static testing, the specimens displayed substantial permanent deformation; therefore, the results are presented using the J-integral method to account for plasticity effects.

5.3.1. Paris Curve

From the measured and derived crack length data, along with the calculated fracture toughness values, a Paris curve was constructed to characterize the fatigue crack growth rate for the tested specimens. This curve, shown in Figure 5.26, plots the crack growth rate (da/dN) against the applied fracture toughness (J_{max}), providing insight into the relationship between loading conditions and crack propagation behavior in mode I fatigue testing.

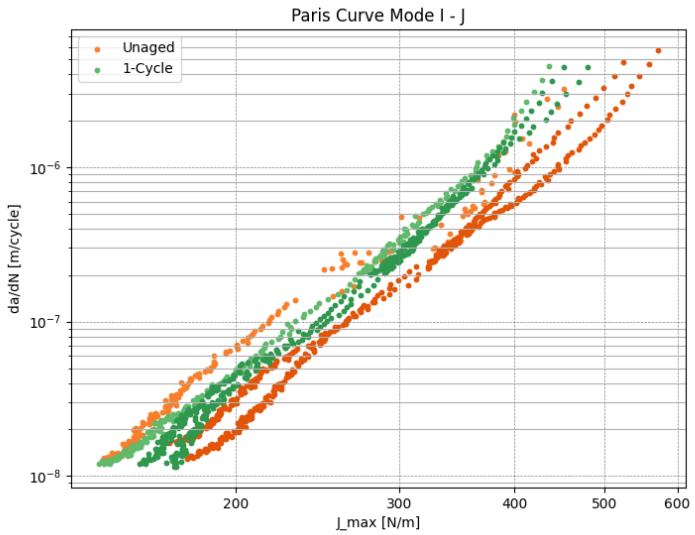

Figure 5.26: Mode I Paris curves.

The results reveal that the crack growth rate (da/dN) for aged specimens is higher than that for unaged specimens, particularly at higher J_{max} values. Conducting an ANOVA analysis at $J_{max} = 420$ N/m, results in a p-value of 0.032, confirming that aging results in statistically significant changes. The difference between aged and unaged specimens remains significant down to a J_{max} value of 318 N/m, below which the p-value exceeds the threshold of 0.05. Indicating that the impact of aging on crack growth diminishes as J_{max} decreases.

5.3.2. Fractography

This section will present and discuss the fractography results obtained from mode I specimens tested in fatigue. Images, 5.27a & 5.27b, present an overview image of unaged and 1-cycle aged specimens. Images, 5.27c & 5.27d show the fibers up close. The overall damage pattern between unaged and aged don't show any significant differences, with the fiber possibly indicating more resin attached for unaged.

Further examination using SEM is shown in Figure 5.28. Here similar things are observed as in mode I QS testing, with similar damage patterns and only small differences in observed size of smooth matrix patches in unaged specimens, as shown in the top right of Figure 5.28a. A closer examination of the surfaces of individual fibers across aging states did not reveal any significant differences.

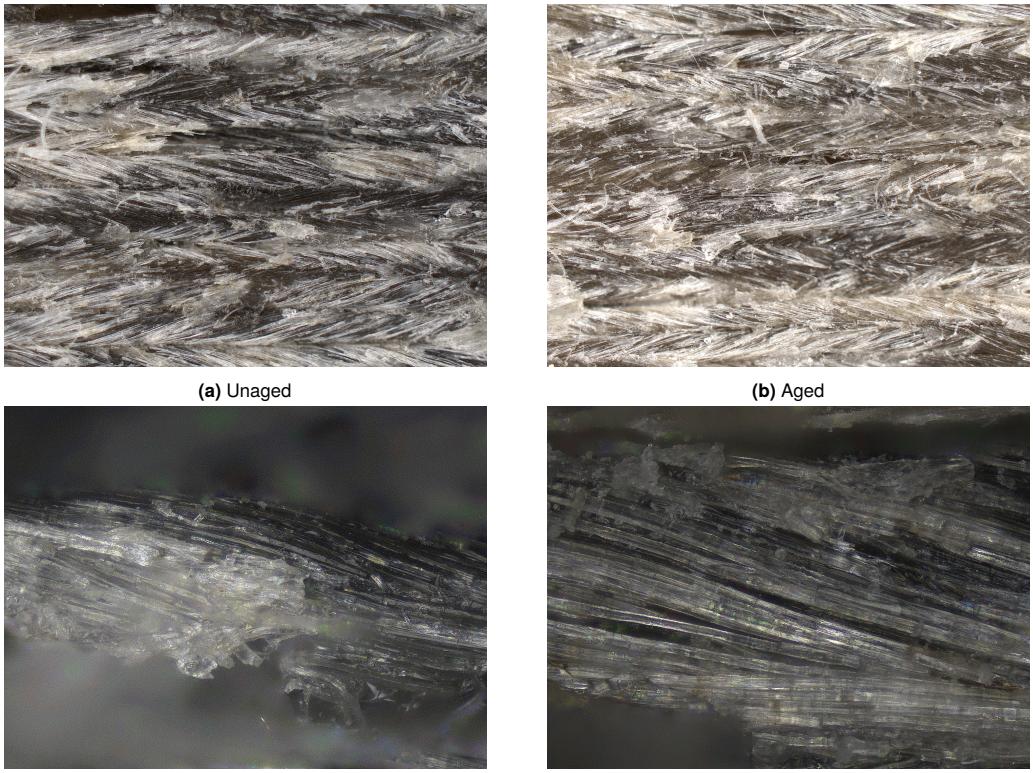

(a) Unaged **(b)** Aged

(c) Unaged 20X fiber **(d)** Aged 20X fiber

Figure 5.27: Fracture surface images from Keyence microscope for mode I fatigue testing.

5.3.3. Surface Roughness

Table 5.3, shows the results obtained from measuring the surface roughness of mode I fatigue samples. Both the top and bottom arms were evaluated, similar to mode II QS, the crack did not propagate far in fatigue and the roughness was evaluated near the center of the crack growth zone.

Table 5.3: Surface roughness (Sa) for mode I Fatigue specimens across aging conditions.

	Unaged (U)	1-Cycle (A1)
Bottom arm (Sa)	88.4 $\pm$ 27.56 μm	67.61 $\pm$ 13.55 μm
Top arm (Sa)	88.29 $\pm$ 6.65 μm	79.2 $\pm$ 1.38 μm

The results indicate that the surface roughness in both the top and bottom arms appears to decrease after one aging cycle. This agrees with the reduction in fracture toughness after aging in fatigue and revealing an opposite trend from mode I QS testing where surface roughness and fracture toughness increased after aging. However, there is substantial variability across measurements, which introduces uncertainty and limits the ability to confirm this trend with high confidence.

5.3.4. Summary of Findings

Mode I fatigue testing was evaluated using the J_{max} parameter, as the specimens exhibited plasticity, which invalidated LEFM assumptions and resulted in negative force values at minimum displacement. Unlike mode I quasi-static testing, aged specimens performed worse in fatigue testing, especially at higher J_{max} values. The crack growth rate in aged specimens at a given J_{max} was higher than in unaged specimens. At lower J_{max} values, the distinction between aged and unaged specimens becomes less pronounced. The data indicated statistically significant changes between aging states down to $J_{max} = 318$ N/m.

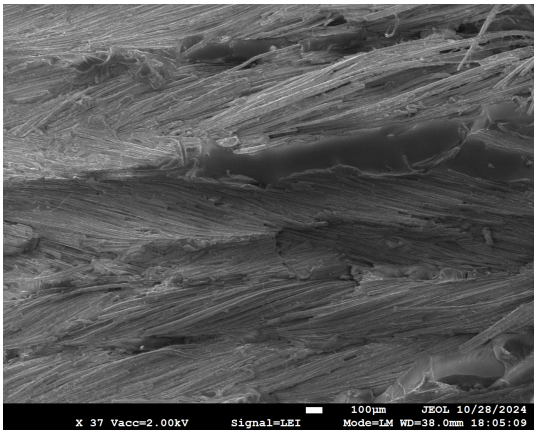

(a) Unaged

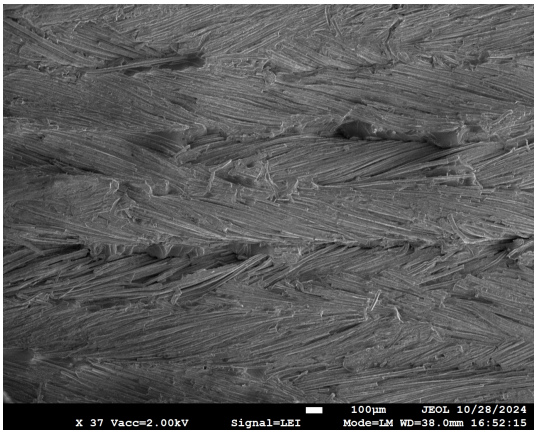

(b) Aged

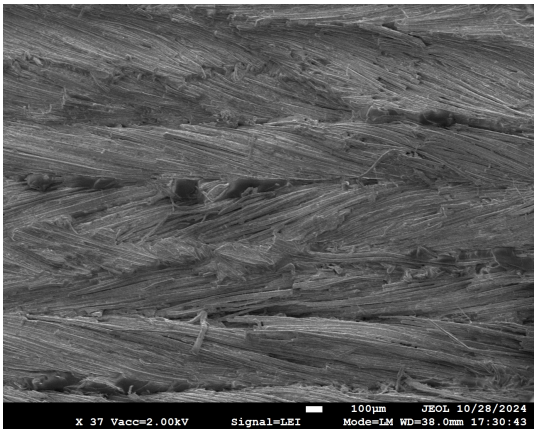

(c) Unaged

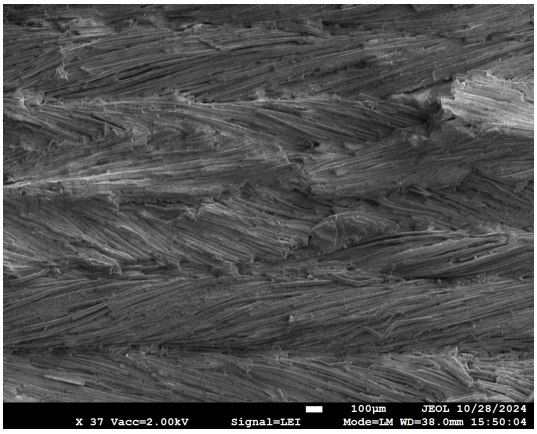

(d) Aged

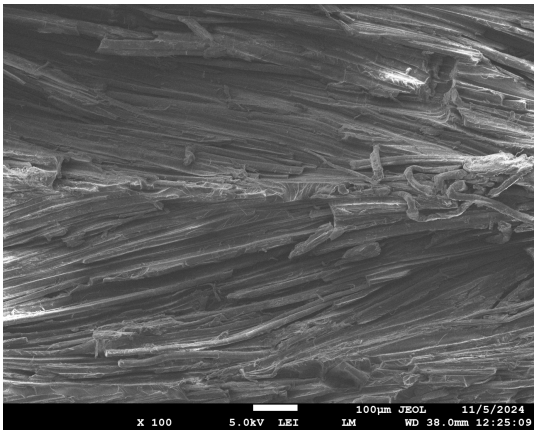

(e) Unaged enlarged

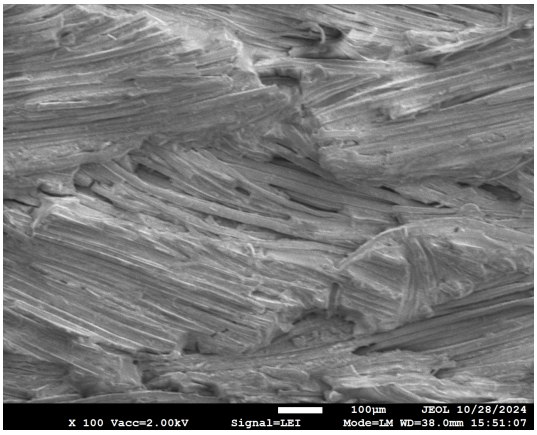

(f) Aged enlarged

Figure 5.28: SEM images of fracture surfaces from mode I fatigue testing.

This is an opposite trend compared to unpublished data by the D-STANDART project, where aging improved the fatigue performance. Analysis of the fracture surfaces, did not reveal any clear differences between aged and unaged. Surface roughness revealed the roughness decreasing after 1-aging cycle in agreement with the fracture toughness results.

5.4. Mode II Fatigue

This section presents the results obtained from mode II fatigue testing. The laboratory temperature remained relatively constant throughout this phase of the experimental campaign, ranging between 23.8 and 25.5 °C. It must be noted that the specimens were not subjected to pure mode II loading, with the unloading cycle, resulting in a tensile opening mode. Figure 5.29 illustrates the crack growth progression during the fatigue tests.

For all specimens, crack growth was measured until the crack advanced to within 10 mm of the clamp. As shown in Figure 5.29, some specimens, both aged and unaged, reached this point after approximately 25,000 cycles, while others continued until 87,500 or even 175,000 cycles. This wide variation in the number of cycles required to reach the final crack length highlights a notable variability in crack growth behavior across the specimens.

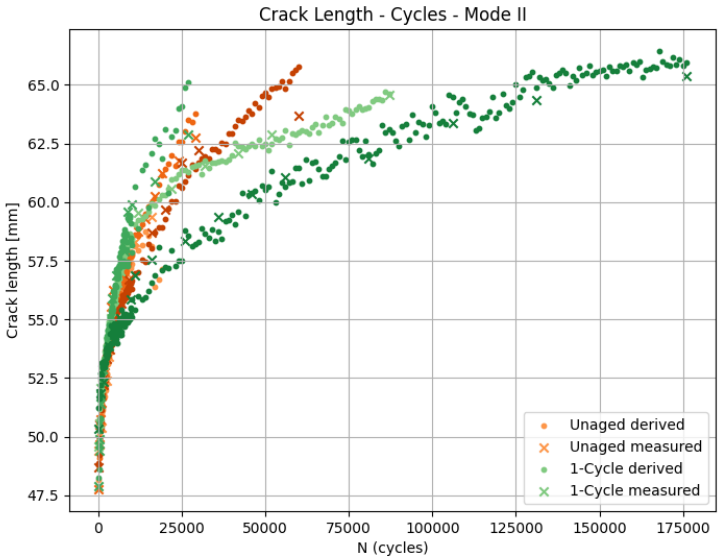

Figure 5.29: Mode II a-N curve illustrating the relationship between crack length and number of cycles.

In contrast to mode I fatigue testing, the effect of aging on crack growth appears less pronounced. The crack growth behavior of unaged specimens generally falls within the broad range observed for the 1-cycle aged specimens, indicating that aging has a less consistent influence on crack propagation under the subjected loading conditions.

5.4.1. Paris Curve

To further examine the crack growth behavior, a Paris curve was created. Figure 5.30 illustrates the Paris curves for both unaged and 1-cycle aged specimens. The Paris curve for mode II shows a wide range for the Paris relation between both unaged and aged specimens, consistent with the observations from the a-N curve. Aged specimens do show a reduced variability compared to unaged specimens. However, the spread makes it impossible to say whether the aging otherwise significantly affects the fracture toughness of mode II fatigue loading.

5.4.2. Fractography

Figures 5.31 and 5.32 show the unaged and aged fracture surfaces obtained from the Keyence microscope, respectively. No clear differences between aged and unaged specimens were observed. A similar pattern to mode II fatigue was identified, where the top arm contained fiber bundles and the bottom arm primarily exhibited fiber imprints.

Further examining the specimens, using SEM, resulted in the images presented in Figure 5.33. From

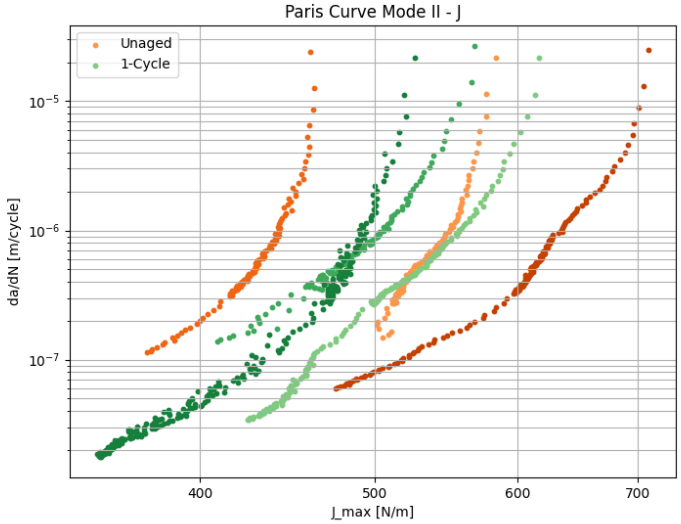

Figure 5.30: Mode II Paris curves.

(a) Bottom arm **(b)** Top arm **(c)** Bottom arm fiber 20X

Figure 5.31: Keyence unaged fracture surfaces from mode II fatigue testing.

(a) Bottom arm **(b)** Top arm **(c)** Bottom arm fiber 20X

Figure 5.32: Fracture surface images from Keyence microscope for mode II fatigue testing.

these images, the fracture pattern looks different compared to mode II QS static testing with less pronounced cusping, which may be due to the slower propagation of the crack in fatigue and the introduced mode I crack opening component.

5.4.3. Surface Roughness

Finally, the surface roughness for mode II is presented in Table 5.4. Both the top and bottom arms were evaluated, near the center of the crack growth zone.

Similar to mode I fatigue, the surface roughness of the specimens generally tends to decrease after aging. However, the high variability observed in both fracture toughness and surface roughness measurements makes it impossible to correlate surface roughness findings with fracture toughness.

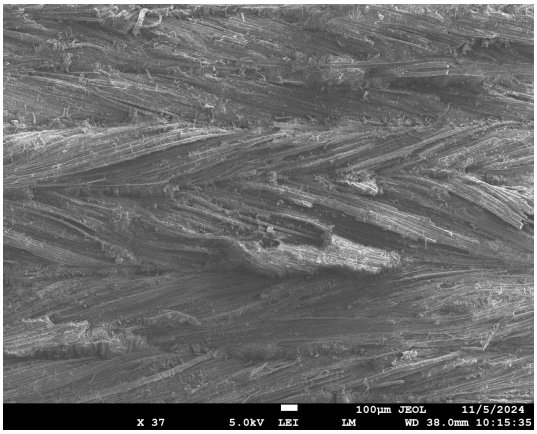

(a) Unaged top arm

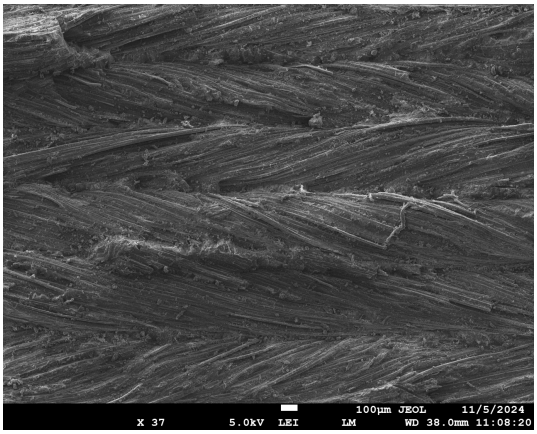

(b) Aged top arm

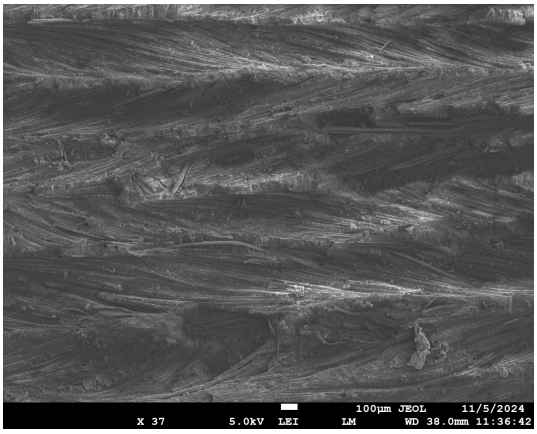

(c) Unaged bottom arm

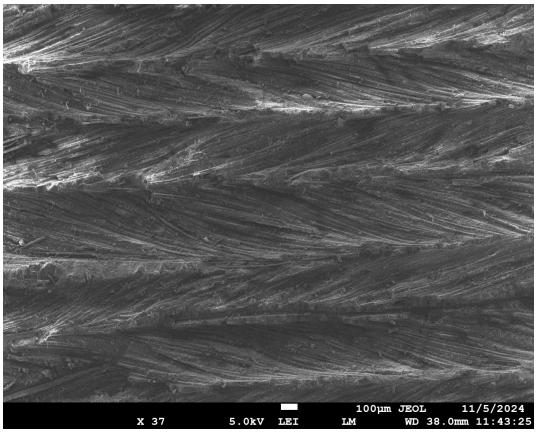

(d) Aged bottom arm

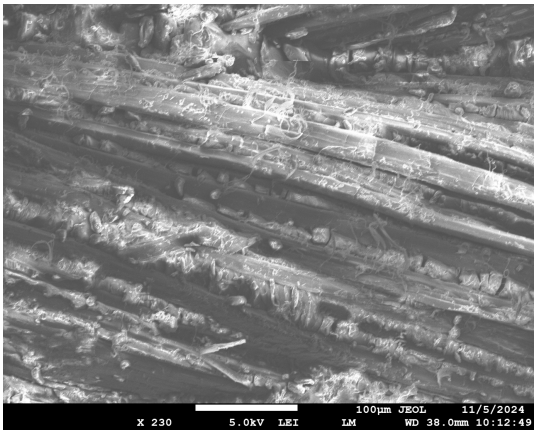

(e) Unaged enlarged

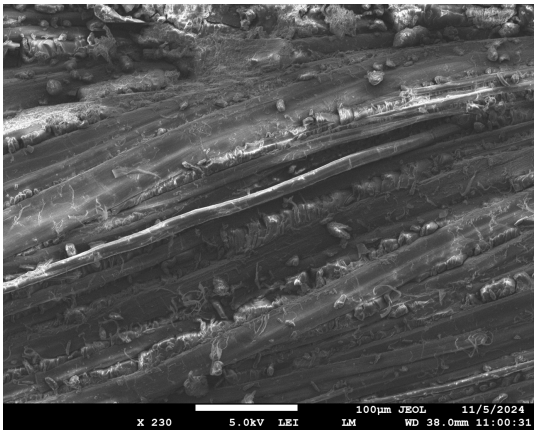

(f) Aged enlarged

Figure 5.33: SEM images of fracture surfaces from mode II fatigue testing.

5.4.4. Summary of Findings

Mode II fatigue testing proved challenging, yielding an uncertain set of results regarding the effect of aging on fracture toughness. The primary effect of aging observed was a reduction in variance compared to the unaged tests. For more reliable results, testing should be conducted on thicker specimens, eliminating the mode I component of the test as the applied energy is directed toward crack propagation rather than deformation of the specimen arms. Additionally, this would allow for a longer free length, enabling further crack propagation and collection of more data.

Table 5.4: Surface roughness (Sa) for mode II Fatigue specimens across aging conditions.

	Unaged (U)	1-Cycle (A1)
Bottom arm (Sa)	83.28 $\pm$ 12.91 μm	77.87 $\pm$ 5.21 μm
Top arm (Sa)	84.3 $\pm$ 14.52 μm	73.42 $\pm$ 8.28 μm

6

Conclusion & Recommendations

This chapter summarizes the effects of hygrothermal aging on the fracture toughness of flax fiber-reinforced composites and provides recommendations for future research.

6.1. Conclusion

This study investigated the hygrothermal effects on the fracture toughness of flax fiber-reinforced composites (FFRP), focusing on quasi-static (QS) and fatigue responses under both mode I and mode II conditions. To assess these effects, Double Cantilever Beam (DCB) and End-Loaded Split (ELS) specimens were manufactured. A portion of the specimens were exposed to one or two cycles of humidification and drying at elevated temperature in a climate chamber, while the remaining specimens were retained as control specimens in an unaged state. The results reveal nuanced effects of aging on fracture behavior, differing between modes, initiation, and propagation regions.

Testing of flax fiber-reinforced polymer (FFRP) composites proved challenging due to the thickness of the manufactured specimens and the non-linear, time-dependent behavior of flax fibers. Both DCB and especially ELS specimens tested in quasi-static and fatigue modes exhibited significant plastic deformation, invalidating the assumptions of Linear Elastic Fracture Mechanics (LEFM) typically used to calculate fracture toughness according to standard methods. Consequently, the J-integral was used to calculate fracture toughness for both mode I and mode II. The J-integral, based on non-linear fracture mechanics, accommodates larger Fracture Process Zones and accounts for large displacements through the beam opening angle. While these equations do not fully capture all effects observed in the FFRP specimens, they provide a more realistic approximation of fracture toughness compared to the Strain Energy Release Rate (SERR). Thus, the obtained fracture toughness values are primarily intended for comparative analysis between aging states, while also offering valuable insight into potential fracture behavior in FFRP structures with similar stiffness.

In mode I QS testing, the findings indicate that a single aging cycle was sufficient to substantially increase the average initiation fracture toughness by 19%, with no further changes to the initiation fracture toughness after a second aging cycle. In contrast, the propagation fracture toughness was not deemed to be significantly affected by aging. The observed improvement on initiation toughness is likely due to the plasticization of fibers and matrix from moisture absorption during aging.

Mode II QS testing of FFRP did not show any trends or significant changes in fracture toughness after aging, in either the initiation or propagation phases. ELS specimens were more profoundly affected by the plastic deformation than DCB specimens, possibly resulting in measuring more non-linearity effects rather than pure fracture toughness. The measured variation in specimen thickness, ranging from 3.2 to 3.9 mm, showed an upward trend in fracture toughness as the thickness and therefore stiffness increased. Future testing of stiffer specimens may therefore lead to different results.

Mode I fatigue testing showed a leftward shift on the Paris curve for aged specimens, indicating a reduction in delamination growth resistance compared to unaged specimens. This trend contrasts with

findings from QS testing and may stem from inherent differences between the two loading modes. The difference between aging states was determined to be statistically significant at higher J_{max} values, diminishing after initial crack propagation. This pattern aligns with the QS findings, where the effect of aging was more significant during initiation than in the propagation phase. Mode II fatigue testing yielded more uncertain results, with the Paris curve displaying high variability among unaged specimens. Aging appeared to reduce this variability, resulting in a narrower range that fell within the wide spread of the unaged specimen results. Analysis of the fracture surfaces of fatigue specimens revealed a reduction in surface roughness of approximately 10% for mode I and 17% for mode II in aged specimens, suggesting that unaged specimens followed a more tortuous fracture path, contributing to higher fracture toughness.

Fractographic analysis of the fracture surfaces did not reveal any significant differences in damage patterns, fiber-matrix adhesion, or matrix residue on fibers. This suggests that the observed shift in initiation fracture toughness for mode I QS testing is primarily attributed to changes in internal material properties rather than variations in fracture surface characteristics.

The findings indicate cautiously optimistic results for QS fracture toughness testing. Mode I, initiation fracture toughness increased after one aging cycle, while mode II fracture toughness remained unaffected. This suggests that fracture toughness either improves or remains stable after exposure to cycles of humidification and drying at elevated temperature. Fatigue testing on the other hand indicates a reduced effect on mode I fracture toughness, requiring more caution in designing FFRP components subjected to environmental conditions. These conclusions demonstrate that hygrothermal aging has a multifaceted and complex influence on flax fiber composites. Contributing valuable insights into designing durable natural fiber composites capable of withstanding environmental conditions. Providing an eco-friendly alternative to conventional composites and contributing to reduced reliance on synthetic, non-renewable resources.

6.2. Recommendations for Future Work

While this study provides valuable insights into the hygrothermal effects on fracture toughness in FFRP, it also highlights key areas for improvement in the future development of this research.

6.2.1. Stiffer Specimens

Plastic deformation exhibited by both DCB and ELS specimens invalidated the assumptions of Linear Elastic Fracture Mechanics (LEFM). To prevent this, the specimen arms need to be stiffer so that the energy applied to the specimen is directed toward crack propagation rather than dissipating through plastic deformation of the arms. For future research, the following calculations may be used as a guideline for determining appropriate specimen thickness for DCB and ELS samples.

Using simple beam theory (SBT), the required specimen arm thickness can be calculated using the following equation:

$$h_{arm} = \sqrt{\frac{6P_{max}a_0}{b\sigma_y^f}}, \quad and\ t_{specimen} = 2h_{arm} \tag{6.1}$$

where:

- P_{max} = Maximum expected force
- a_0 = Initial delamination length
- b = specimen width
- σ_y^f = flexural yield strength

From the Amplitex 280 datasheet, the flexural strength is given as 198 MPa when paired with Araldite epoxy. The Swancor epoxy used in this study has a flexural strength of 110-120 MPa, compared to the 115-125 MPa of Araldite. To estimate the required thickness for Swancor epoxy, the flexural

strength was taken as 175 MPa. The specimen width and insert length were kept at 25 mm and 50 mm, respectively.

$$G_I^{SBT} = \frac{12P^2a_0^2}{b^2h_{arm}^3E_{11}} \tag{6.2}$$

$$G_{II}^{SBT} = \frac{9P^2a_0^2}{4b^2h_{arm}^3E_{11}} \tag{6.3}$$

Here, E_{11} was taken as 12068 MPa, as previously discussed in Section 4.3.2. The required fracture toughness for mode I & II were taken as the average of the aged specimens for mode I and for mode II as the average of both aged and unaged specimens, resulting in 1108 N/m for mode I and 1129 N/m mode II. The required thickness was iteratively calculated until the applied force and calculated thickness matched the experimentally determined fracture toughness. This resulted in a required specimen thickness of 2.624 mm and 14.237 for mode I & II respectively.

For mode I, the calculated thickness is 19% thinner than the tested specimens and corresponds to a force of 25 N. This result is clearly incorrect, as the tested specimens with a thickness of 3.8 mm already exhibited significant plastic deformation. The maximum force experienced during mode I test was 54 N, doubling this as a safety margin, leads to a required specimen thickness of 5.44 mm and an estimated applied fracture toughness of 2302 N/m.

For mode II, the calculated thickness of 14.2 mm is already considerable but could require even more since mode I, also significantly underestimated the required thickness. To achieve such a thickness, the current manufacturing method would have to be adapted significantly, or changed to a resin transfer molding process. An alternative approach would be to reinforce the specimens with a stiffer material, such as glass fiber, carbon fiber or steel, applied to the top and bottom surfaces of the specimen.

If the current manufacturing method is to be used in the future, it is recommended, to adapt the process to ensure accurate thickness control. A more precise method for regulating specimen thickness should be implemented, rather than relying on layers of tacky tape. This can be accomplished by placing spacers at the corners of the top plate to provide consistent and controlled spacing.

6.2.2. Testing In-Situ Environmental Conditions

To gain a comprehensive understanding of how FFRP behaves under environmental conditions, future research should expand to testing under in-situ environmental conditions. This approach would provide insights into how fracture toughness is affected when subjected to direct environmental conditions.

6.2.3. Influence of Viscoelastic Material Behavior on Fracture Toughness

Flax fiber composites exhibit viscoelastic material behavior, meaning that the material has an elastic and time-dependent response to deformation. This behavior, may influence the fracture toughness, particularly under sustained or cyclic loading conditions, as time dependent deformation may alter crack propagation and dissipate energy through relaxation. Understanding how this viscoelastic behavior influences the fracture toughness would lead to a better understanding and allow for more accurate predictions.

6.2.4. Alternate Crack Propagation Measurements

Accurately determining crack length is a critical yet challenging aspect of fracture toughness measurements. Precisely identifying the crack front from the specimen's edge can introduce variability and only provides information from one side, while the actual crack length likely varies across the specimen width. To enhance measurement reliability, several methods can be employed. One approach involves using Digital Image Correlation (DIC), where a speckle pattern is applied to the specimen's surface, enabling DIC software to monitor crack propagation by detecting deformations around the crack tip. Alternatively, for translucent FFRP samples, illuminating the underside of the specimen with a bright light can help visualize and accurately locate the crack front, as shown in Figure 6.1. This method was discovered

midway through the testing campaign and was therefore not applied in this thesis, but it offers a simple yet reliable approach for determining crack length during testing.

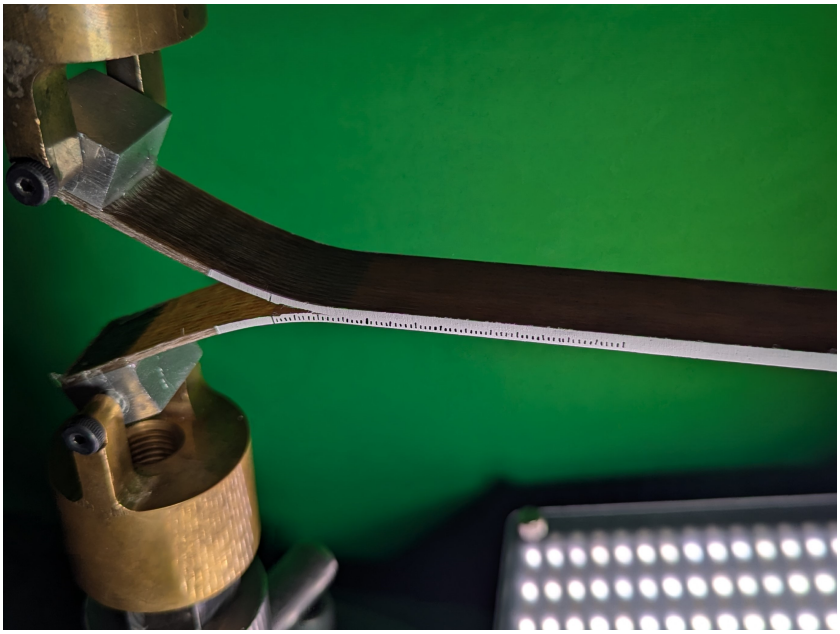

Figure 6.1: Visualization of crack length in FFRP specimens, utilizing their translucent properties to enhance crack tracking during testing.

References

[1] *Goal 12 | UN Department of Economic and Social Affairs*. URL: https://sdgs.un.org/goals/goal12.

[2] *Goal 13 | UN Department of Economic and Social Affairs*. URL: https://sdgs.un.org/goals/goal13.

[3] Libo Yan, Nawawi Chouw, and Krishnan Jayaraman. "Flax fibre and its composites – A review". In: *Composites Part B: Engineering* 56 (Jan. 2014), pp. 296–317. ISSN: 1359-8368. DOI: 10.1016/J.COMPOSITESB.2013.08.014.

[4] Paul Wambua, Jan Ivens, and Ignaas Verpoest. "Natural fibres: can they replace glass in fibre reinforced plastics?" In: *Composites Science and Technology* 63.9 (July 2003), pp. 1259–1264. ISSN: 0266-3538. DOI: 10.1016/S0266-3538(03)00096-4.

[5] Yi-Fan Niu, Yan Yan, and Jia-Wei Yao. "Hygrothermal aging mechanism of carbon fiber/epoxy resin composites based on quantitative characterization of interface structure". In: (2020). DOI: 10.1016/j.polymertesting.2020.107019. URL: https://doi.org/10.1016/j.polymertesting.2020.107019.

[6] Shulan Yang et al. "Influence of hygrothermal aging on the durability and interfacial performance of pultruded glass fiber-reinforced polymer composites". In: *Journal of Materials Science* 54.3 (Feb. 2019), pp. 2102–2121. ISSN: 15734803. DOI: 10.1007/S10853-018-2944-6. URL: https://www.researchgate.net/publication/328008654_Influence_of_hygrothermal_aging_on_the_durability_and_interfacial_performance_of_pultruded_glass_fiber-reinforced_polymer_composites.

[7] A. Bergeret, L. Ferry, and P. Ienny. "Influence of the fibre/matrix interface on ageing mechanisms of glass fibre reinforced thermoplastic composites (PA-6,6, PET, PBT) in a hygrothermal environment". In: *Polymer Degradation and Stability* 94.9 (Sept. 2009), pp. 1315–1324. ISSN: 0141-3910. DOI: 10.1016/J.POLYMDEGRADSTAB.2009.04.009.

[8] Yan Li and Bing Xue. "Hydrothermal ageing mechanisms of unidirectional flax fabric reinforced epoxy composites". In: (2016). DOI: 10.1016/j.polymdegradstab.2016.02.004. URL: http://dx.doi.org/10.1016/j.polymdegradstab.2016.02.004.

[9] M. Ravandi et al. "The effects of through-the-thickness stitching on the Mode I interlaminar fracture toughness of flax/epoxy composite laminates". In: *Materials & Design* 109 (Nov. 2016), pp. 659–669. ISSN: 0264-1275. DOI: 10.1016/J.MATDES.2016.07.093.

[10] Eliso Kvavadze et al. "30,000-Year-Old Wild Flax Fibers". In: *Science (New York, N.Y.)* 325 (Mar. 2009), p. 1359. DOI: 10.1126/science.1175404.

[11] Issam Elfaleh et al. "A comprehensive review of natural fibers and their composites: An eco-friendly alternative to conventional materials". In: *Results in Engineering* 19 (Sept. 2023), p. 101271. ISSN: 2590-1230. DOI: 10.1016/J.RINENG.2023.101271.

[12] M. Ramesh. "Flax (Linum usitatissimum L.) fibre reinforced polymer composite materials: A review on preparation, properties and prospects". In: *Progress in Materials Science* 102 (May 2019), pp. 109–166. ISSN: 0079-6425. DOI: 10.1016/J.PMATSCI.2018.12.004.

[13] *Flax Fibers (HS: Flax,) Product Trade, Exporters and Importers | The Observatory of Economic Complexity*. URL: https://oec.world/en/profile/hs/flax-fibers.

[14] *Flax-linen Tex & Tech | ALLIANCE*. URL: https://allianceflaxlinenhemp.eu/en/flax-lin-tex-tech.

[15] Nina Graupner et al. "A Competitive Study of the Static and Fatigue Performance of Flax, Glass, and Flax/Glass Hybrid Composites on the Structural Example of a Light Railway Axle Tie". In: *Frontiers in Materials* 9 (Apr. 2022), p. 837289. ISSN: 22968016. DOI: 10.3389/FMATS.2022.837289/BIBTEX.

[16] J H Lee et al. “Development of Natural Fiber Wind Turbine Blades using Design Optimization Technology”. In: ().

[17] Darshil U. Shah, Peter J. Schubel, and Mike J. Clifford. “Can flax replace E-glass in structural composites? A small wind turbine blade case study”. In: *Composites Part B: Engineering* 52 (Sept. 2013), pp. 172–181. ISSN: 1359-8368. DOI: 10.1016/J.COMPOSITESB.2013.04.027.

[18] Z N Azwa et al. “A review on the degradability of polymeric composites based on natural fibres”. In: (2012). DOI: 10.1016/j.matdes.2012.11.025. URL: http://dx.doi.org/10.1016/j.matdes.2012.11.025.

[19] A. Stamboulis, C. A. Baillie, and T. Peijs. “Effects of environmental conditions on mechanical and physical properties of flax fibers”. In: *Composites Part A: Applied Science and Manufacturing* 32.8 (Aug. 2001), pp. 1105–1115. ISSN: 1359-835X. DOI: 10.1016/S1359-835X(01)00032-X.

[20] Abdul Moudood et al. “Environmental effects on the durability and the mechanical performance of flax fiber/bio-epoxy composites”. In: *Composites Part B: Engineering* 171 (Aug. 2019), pp. 284–293. ISSN: 1359-8368. DOI: 10.1016/J.COMPOSITESB.2019.05.032.

[21] W. Woigk et al. “Interface properties and their effect on the mechanical performance of flax fibre thermoplastic composites”. In: *Composites Part A: Applied Science and Manufacturing* 122 (July 2019), pp. 8–17. ISSN: 1359-835X. DOI: 10.1016/J.COMPOSITESA.2019.04.015.

[22] Nick Sweygers et al. “Prediction of the equilibrium moisture content based on the chemical composition and crystallinity of natural fibres”. In: *Industrial Crops and Products* 186 (Oct. 2022), p. 115187. ISSN: 0926-6690. DOI: 10.1016/J.INDCROP.2022.115187.

[23] Lennart Salmén and Elina Bergström. “Cellulose structural arrangement in relation to spectral changes in tensile loading FTIR”. In: *Cellulose* 16.6 (Dec. 2009), pp. 975–982. ISSN: 09690239. DOI: 10.1007/S10570-009-9331-Z/FIGURES/11. URL: https://link.springer.com/article/10.1007/s10570-009-9331-z.

[24] Mohammad Asim et al. “Thermal stability of natural fibers and their polymer composites”. In: *Iranian Polymer Journal 2020 29:7* 29.7 (May 2020), pp. 625–648. ISSN: 1735-5265. DOI: 10.1007/S13726-020-00824-6. URL: https://link.springer.com/article/10.1007/s13726-020-00824-6.

[25] *Primary Wood Processing: Principles and Practice - John C.F. Walker - Google Books*. URL: https://books.google.nl/books?hl=en&lr=&id=wJ-I0LwnyP4C&oi=fnd&pg=PR9&ots=YwF2Rma5dm&sig=LZh7rZTtXO942irE6NHoSws4zsQ&redir_esc=y#v=onepage&q&f=false.

[26] Maya Jacob John and Sabu Thomas. “Biofibres and biocomposites”. In: *Carbohydrate Polymers* 71.3 (Feb. 2008), pp. 343–364. ISSN: 0144-8617. DOI: 10.1016/J.CARBPOL.2007.05.040.

[27] Christophe Baley et al. “Variability of mechanical properties of flax fibres for composite reinforcement. A review”. In: *Industrial Crops and Products* 145 (Mar. 2020), p. 111984. ISSN: 0926-6690. DOI: 10.1016/J.INDCROP.2019.111984.

[28] J. Andersons, E. Poriķe, and E. Sparniņš. “The effect of mechanical defects on the strength distribution of elementary flax fibres”. In: *Composites Science and Technology* 69.13 (Oct. 2009), pp. 2152–2157. ISSN: 0266-3538. DOI: 10.1016/J.COMPSCITECH.2009.05.010.

[29] Christophe Baley and Alain Bourmaud. “Average tensile properties of French elementary flax fibers”. In: *Materials Letters* 122 (May 2014), pp. 159–161. ISSN: 0167-577X. DOI: 10.1016/J.MATLET.2014.02.030.

[30] C. Baley. “Analysis of the flax fibres tensile behaviour and analysis of the tensile stiffness increase”. In: *Composites Part A: Applied Science and Manufacturing* 33.7 (July 2002), pp. 939–948. ISSN: 1359-835X. DOI: 10.1016/S1359-835X(02)00040-4.

[31] Christophe Baley et al. “Specific features of flax fibres used to manufacture composite materials”. In: *International Journal of Material Forming 2018 12:6* 12.6 (Dec. 2018), pp. 1023–1052. ISSN: 1960-6214. DOI: 10.1007/S12289-018-1455-Y. URL: https://link.springer.com/article/10.1007/s12289-018-1455-y.

[32] Morten ; Rask and Bo Madsen. “General rights Twisting of fibres in yarns for natural fibre composites 18 TH INTERNATIONAL CONFERENCE ON COMPOSITE MATERIALS”. In: ().

[33] Hongbin Li et al. “Recent Progress in Flax Fiber-Based Functional Composites”. In: *Advanced Fiber Materials* 4 (2022), pp. 171–184. DOI: 10.1007/s42765-021-00115-6. URL: https://doi.org/10.1007/s42765-021-00115-6.

[34] Amna Siddique, Baozhong Sun, and Bohong Gu. “Structural influences of two-dimensional and three-dimensional carbon/epoxy composites on mode I fracture toughness behaviors with rate effects on damage evolution”. In: *Journal of Industrial Textiles* 50.1 (July 2020), pp. 23–45. ISSN: 15308057. DOI: 10.1177/1528083718819871/ASSET/IMAGES/LARGE/10.1177{_}1528083718819871-FIG19.JPEG. URL: https://journals.sagepub.com/doi/full/10.1177/1528083718819871.

[35] T. A. Sebaey et al. “Characterization of crack propagation in mode I delamination of multidirectional CFRP laminates”. In: *Composites Science and Technology* 72.11 (June 2012), pp. 1251–1256. ISSN: 0266-3538. DOI: 10.1016/J.COMPSCITECH.2012.04.011.

[36] *ASTM D5528-13*. URL: https://compass.astm.org/document/?contentCode=ASTM%7CD5528-13%7Cen-US&proxycl=https%3A%2F%2Fsecure.astm.org&fromLogin=true.

[37] *ASTM D7905*. URL: https://compass.astm.org/document/?contentCode=ASTM%7CD7905_D7905M-19E01%7Cen-US&proxycl=https%3A%2F%2Fsecure.astm.org&fromLogin=true.

[38] *ISO 15114:2014 - Fibre-reinforced plastic composites — Determination of the mode II fracture resistance for unidirectionally reinforced materials using the calibrated end-loaded split (C-ELS) test and an effective crack length approach*. URL: https://www.iso.org/standard/55357.html.

[39] Yangyang Ge et al. “Test methods for measuring pure mode III delamination toughness of composite Emmanuel Test methods for measuring pure mode III delamination toughness of composite Open Archive Toulouse Archive Ouverte (OATAO) Test methods for measuring pure mode III delamination toughness of composite”. In: *Polymer Testing* 55 (2016), pp. 261–268. ISSN: 0142-9418. DOI: 10.1016/j.polymertesting.2016.08.025{\"{i}}. URL: https://u-bourgogne.hal.science/hal-01445372.

[40] James G Ratcliffe. “Characterization of the Edge Crack Torsion (ECT) Test for Mode III Fracture Toughness Measurement of Laminated Composites”. In: ().

[41] W J Cantwell and Andj Morton. “The impact resistance of composite materials-a review”. In: ().

[42] S Heimbs et al. “Failure behaviour of composite T-joints with novel metallic arrow-pin reinforcement”. In: (2013). DOI: 10.1016/j.compstruct.2013.11.022. URL: http://dx.doi.org/10.1016/j.compstruct.2013.11.022.

[43] Laraib Alam Khan et al. “Effect of hygrothermal conditioning on the fracture toughness of carbon/epoxy composites cured in autoclave/Quickstep”. In: *Journal of Reinforced Plastics and Composites* 32.16 (2013), pp. 1165–1176. ISSN: 15307964. DOI: 10.1177/0731684413486367/FORMAT/EPUB.

[44] M A Caminero, I García-Moreno, and G P Rodríguez. “Experimental study of the influence of thickness and ply-stacking sequence on the compression after impact strength of carbon fibre reinforced epoxy laminates”. In: (2018). DOI: 10.1016/j.polymertesting.2018.02.009. URL: https://doi.org/10.1016/j.polymertesting.2018.02.009.

[45] Na Ning et al. “Effect of polymer nanoparticle morphology on fracture toughness enhancement of carbon fiber reinforced epoxy composites”. In: *Composites Part B* 234 (2022), pp. 1359–8368. DOI: 10.1016/j.compositesb.2022.109749. URL: https://doi.org/10.1016/j.compositesb.2022.109749.

[46] Hamed Fallahi et al. “Insights into the effect of fiber-matrix interphase physiochemical-mechanical properties on delamination resistance and fracture toughness of hybrid composites”. In: (2022). DOI: 10.1016/j.compositesa.2022.107390. URL: https://doi.org/10.1016/j.compositesa.2022.107390.

[47] Toshiya Kamae and Lawrence T Drzal. “Carbon fiber/epoxy composite property enhancement through incorporation of carbon nanotubes at the fiber-matrix interphase-Part II: Mechanical and electrical properties of carbon nanotube coated carbon fiber composites”. In: (2022). DOI: 10.1016/j.compositesa.2022.107023. URL: https://doi.org/10.1016/j.compositesa.2022.107023.

[48] R O Ritchie. “Mechanisms of fatigue-crack propagation in ductile and brittle solids”. In: *International Journal of Fracture* 100 (1999), pp. 55–83.

[49] Hailong Shi et al. “Role of extrinsic and intrinsic toughening mechanisms in graphene nanosheets reinforced magnesium matrix layered composites”. In: *Materials Science and Engineering: A* 885 (Oct. 2023), p. 145619. ISSN: 0921-5093. DOI: 10.1016/J.MSEA.2023.145619.

[50] Radhika Wazalwar, Megha Sahu, and Ashok M. Raichur. “Mechanical properties of aerospace epoxy composites reinforced with 2D nano-fillers: current status and road to industrialization”. In: *Nanoscale Advances* 3.10 (May 2021), pp. 2741–2776. ISSN: 25160230. DOI: 10.1039/D1NA00050K.

[51] M F Hibbs, M K Tse, and W L Bradley. “Interlaminar Fracture Toughness and Real-Time Fracture Mechanism of Some Toughened Graphite/Epoxy Composites”. In: *Toughened Composites*. Ed. by N J Johnston. West Conshohocken, PA: ASTM International, 1987, pp. 115–130. DOI: 10.1520/STP24374S. URL: http://www.astm.org/cgi-bin/doiLink.cgi?STP24374S.

[52] P. Compston, P.-Y.B. Jar, and P. Davies. “Matrix effect on the static and dynamic interlaminar fracture toughness of glass-fibre marine composites”. In: *Composites Part B: Engineering* 29.4 (Jan. 1998), pp. 505–516. ISSN: 13598368. DOI: 10.1016/S1359-8368(98)00004-3.

[53] Oshin Fernandes, Jyoti Dutta, and Yogeesha Pai. “Effect of various factors and hygrothermal ageing environment on the low velocity impact response of fibre reinforced polymer composites-a comprehensive review”. In: *Cogent Engineering* 10.1 (2023). ISSN: 23311916. DOI: 10.1080/23311916.2023.2247228/ASSET/E68598E2-3BE3-4F99-915A-8196987E146A/ASSETS/GRAPHIC/OAEN{_}A{_}2247228{_}F0014{_}OC.JPG.

[54] Carolina Furtado et al. “J-Integral Experimental Reduction Reveals Fracture Toughness Improvements in Thin-Ply Carbon Fiber Laminates with Aligned Carbon Nanotube Interlaminar Reinforcement”. In: *ACS Applied Materials & Interfaces* (Apr. 2024). ISSN: 1944-8244. DOI: 10.1021/ACSAMI.3C17333. URL: https://pubs.acs.org/doi/10.1021/acsami.3c17333.

[55] R. Rikards et al. “Mode I, mode II, and mixed-mode I/II interlaminar fracture toughness of GFRP influenced by fiber surface treatment”. In: *Mechanics of Composite Materials* 32.5 (1996), pp. 439–462. ISSN: 01915665. DOI: 10.1007/BF02313863/METRICS. URL: https://link-springer-com.tudelft.idm.oclc.org/article/10.1007/BF02313863.

[56] Vishnu Prasad et al. “Enhancing Mode I and Mode II interlaminar fracture toughness of flax fibre reinforced epoxy composites with nano TiO 2”. In: (2019). DOI: 10.1016/j.compositesa.2019.105505. URL: https://doi.org/10.1016/j.compositesa.2019.105505.

[57] Vishnu Prasad et al. “Evaluation of interlaminar fracture toughness and dynamic mechanical properties of nano TiO2 coated flax fibre epoxy composites”. In: *Polymer Testing* 91 (Nov. 2020), p. 106784. ISSN: 0142-9418. DOI: 10.1016/J.POLYMERTESTING.2020.106784.

[58] Yan Li, Yiu Wing Mai, and Lin Ye. “Effects of fibre surface treatment on fracture-mechanical properties of sisal-fibre composites”. In: *Composite Interfaces* 12.1-2 (2005), pp. 141–163. ISSN: 09276440. DOI: 10.1163/1568554053542151. URL: https://www.tandfonline.com/doi/abs/10.1163/1568554053542151.

[59] Rafiullah Khan. “Fiber bridging in composite laminates: A literature review”. In: *Composite Structures* 229 (Dec. 2019), p. 111418. ISSN: 0263-8223. DOI: 10.1016/J.COMPSTRUCT.2019.111418.

[60] Angela Russo et al. “materials Fiber Bridging Induced Toughening Effects on the Delamination Behavior of Composite Stiffened Panels under Bending Loading: A Numerical/Experimental Study”. In: (). DOI: 10.3390/ma12152407. URL: www.mdpi.com/journal/materials.

[61] Liaojun Yao et al. “Bridging effect on mode I fatigue delamination behavior in composite laminates”. In: *Composites Part A: Applied Science and Manufacturing* 63 (Aug. 2014), pp. 103–109. ISSN: 1359-835X. DOI: 10.1016/J.COMPOSITESA.2014.04.007.

[62] *Standard Test Method for Mode I Interlaminar Fracture Toughness of Unidirectional Fiber-Reinforced Polymer Matrix Composites - ASTM D5528*. Tech. rep. URL: https://compass.astm.org/document/?contentCode=ASTM%7CD5528_D5528M-21%7Cen-US.

[63] Mike van der Panne and John Alan Pascoe. “Fatigue delamination growth - Is UD testing enough?” In: *Procedia Structural Integrity* 42 (Jan. 2022), pp. 449–456. ISSN: 2452-3216. DOI: 10.1016/J.PROSTR.2022.12.057.

[64] El Hadi Saidane et al. “Mode-I interlaminar fracture toughness of flax, glass and hybrid flax-glass fibre woven composites: Failure mechanism evaluation using acoustic emission analysis”. In: *Polymer Testing* 75 (May 2019), pp. 246–253. ISSN: 0142-9418. DOI: 10.1016/J.POLYMERTESTING.2019.02.022.

[65] Yousef Saadati et al. “A Study of the Interlaminar Fracture Toughness of Unidirectional Flax/Epoxy Composites”. In: (). DOI: 10.3390/jcs4020066. URL: www.mdpi.com/journal/jcs.

[66] George C. Jacob et al. “The effect of loading rate on the fracture toughness of fiber reinforced polymer composites”. In: *Journal of Applied Polymer Science* 96.3 (May 2005), pp. 899–904. ISSN: 00218995. DOI: 10.1002/APP.21535.

[67] Yan Li, Di Wang, and Hao Ma. “Improving interlaminar fracture toughness of flax fiber/epoxy composites with chopped flax yarn interleaving”. In: *Science China Technological Sciences* 58.10 (Oct. 2015), pp. 1745–1752. ISSN: 18691900. DOI: 10.1007/S11431-015-5911-3/METRICS. URL: https://link.springer.com/article/10.1007/s11431-015-5911-3.

[68] Benze Yu et al. “Experimental and numerical investigation into interlaminar toughening effect of chopped fiber-interleaved flax fiber reinforced composites”. In: *Acta Mechanica Sinica/Lixue Xuebao* 40.1 (Jan. 2024), pp. 1–14. ISSN: 16143116. DOI: 10.1007/S10409-023-23287-X/METRICS. URL: https://link.springer.com/article/10.1007/s10409-023-23287-x.

[69] F. Bensadoun, I. Verpoest, and A. W. Van Vuure. “Interlaminar fracture toughness of flax-epoxy composites”. In: *Journal of Reinforced Plastics and Composites* 36.2 (Feb. 2017), pp. 121–136. ISSN: 15307964. DOI: 10.1177/0731684416672925/ASSET/IMAGES/LARGE/10.1177{_}0731684416672925-FIG8.JPEG. URL: https://journals-sagepub-com.tudelft.idm.oclc.org/doi/10.1177/0731684416672925.

[70] Wen Xue Wang et al. “Experimental investigation on test methods for mode II interlaminar fracture testing of carbon fiber reinforced composites”. In: *Composites Part A: Applied Science and Manufacturing* 40.9 (Sept. 2009), pp. 1447–1455. ISSN: 1359-835X. DOI: 10.1016/J.COMPOSITESA.2009.04.029.

[71] Thamilarasu S. Rajendran et al. “Mode I and Mode II Delamination of Flax/Epoxy Composite Laminate”. In: *MATEC Web of Conferences* 202 (Sept. 2018), p. 01002. ISSN: 2261-236X. DOI: 10.1051/MATECCONF/201820201002. URL: https://www.matec-conferences.org/articles/matecconf/abs/2018/61/matecconf_aame2018_01002/matecconf_aame2018_01002.html.

[72] P Davies et al. “COMPARISON OF TEST CONFIGURATIONS FOR THE DETERMINATION OF G IIC : RESULTS FROM AN INTERNATIONAL ROUND ROBIN”. In: 28.9 (1999), pp. 432–437. DOI: 10.1179/146580199101540600. URL: http://dx.doi.org/10.1179/146580199101540600.

[73] Alok Behera et al. “Effect of hygrothermal aging on static behavior of quasi-isotropic CFRP composite laminate”. In: *Composites Communications* 17 (Feb. 2020), pp. 51–55. ISSN: 2452-2139. DOI: 10.1016/J.COCO.2019.11.009.

[74] Valentin’ ’Perruchoud. *Effects of in-service environmental conditions on FRP composites*. Tech. rep. 2023.

[75] Thomas Cadu et al. “Cyclic hygrothermal ageing of flax fibers’ bundles and unidirectional flax/epoxy composite. Are bio-based reinforced composites so sensitive?” In: (2019). DOI: 10.1016/j.indcrop.2019.111730. URL: https://doi.org/10.1016/j.indcrop.2019.111730.

[76] Luigi Calabrese et al. “Toughness Evolution of Flax-Fiber-Reinforced Composites under Repeated Salt Fog–Dry Aging Cycles”. In: *Polymers 2024, Vol. 16, Page 1926* 16.13 (July 2024), p. 1926. ISSN: 2073-4360. DOI: 10.3390/POLYM16131926. URL: https://www.mdpi.com/2073-4360/16/13/1926/htm%20https://www.mdpi.com/2073-4360/16/13/1926.

[77] Alan J. Russell and Ken N. Street. “Moisture and Temperature Effects on the Mixed-Mode Delamination Fracture of Unidirectional Graphite/Epoxy”. In: *ASTM Special Technical Publication* (1985), pp. 349–370. ISSN: 00660558. DOI: 10.1520/STP36314S. URL: https://asmedigitalcollection.asme.org/astm-ebooks/book/1517/chapter/27813687/Moisture-and-Temperature-Effects-on-the-Mixed-Mode.

[78] Iton Chou. “Effect of fiber orientation and moisture absorption on the interlaminar fracture toughness of CFRP laminates moisture absorption on the interlaminar fracture toughness of CFRP laminates”. In: (2012). DOI: 10.1163/156855198X00264. URL: https://www.tandfonline.com/action/journalInformation?journalCode=tacm20.

[79] Amar Garg and Ori Ishai. “Hygrothermal Influence on Delamination Behaviour of Graphite/Epoxy Laminates”. In: *NASA Technical Memorandum* 85935 (Mar. 1984). URL: https://ntrs.nasa.gov/api/citations/19840013836/downloads/19840013836.pdf.

[80] Liaojun Yao et al. “Hygrothermal effects on fatigue delamination behavior in composite laminates”. In: *Composite Structures* 330 (Feb. 2024), p. 117830. ISSN: 0263-8223. DOI: 10.1016/J.COMPSTRUCT.2023.117830.

[81] Liaojun Yao et al. “Does hygrothermal degradation of Mode I fatigue delamination resistance in carbon fibre reinforced polymer laminates depend on the ageing conditions?” In: *Composite Structures* 342 (Aug. 2024), p. 118240. ISSN: 0263-8223. DOI: 10.1016/J.COMPSTRUCT.2024.118240.

[82] Irwin G.R. and Kies J.A. “Critical energy rate analysis of fracture strength.” In: *Welding* 33.4 (1954), pp. 193–198.

[83] J. R. Rice. “A Path Independent Integral and the Approximate Analysis of Strain Concentration by Notches and Cracks”. In: *Journal of Applied Mechanics* 35.2 (June 1968), pp. 379–386. ISSN: 0021-8936. DOI: 10.1115/1.3601206. URL: https://dx.doi.org/10.1115/1.3601206.

[84] Joshua Gunderson. “Large Displacement J-Integral Double Cantilever Beam (DCB) Test Method for Mode I Fracture Toughness”. In: *Boise State University Theses and Dissertations* (Dec. 2020). DOI: 10.18122/td/1769/boisestate. URL: https://scholarworks.boisestate.edu/td/1769.

[85] T.L. Anderson. *Fracture Mechanics*. CRC Press, Mar. 2017. ISBN: 9781315370293. DOI: 10.1201/9781315370293.

[86] Fred Nilsson. “Large displacement aspects on fracture testing with double cantilever beam specimens”. In: *International Journal of Fracture* 139.2 (May 2006), pp. 305–311. ISSN: 03769429. DOI: 10.1007/S10704-006-8376-3/METRICS. URL: https://link-springer-com.tudelft.idm.oclc.org/article/10.1007/s10704-006-8376-3.

[87] M. Pérez-Galmés et al. “A data reduction method based on the J-integral to obtain the interlaminar fracture toughness in a mode II end-loaded split (ELS) test”. In: *Composites Part A: Applied Science and Manufacturing* 90 (Nov. 2016), pp. 670–677. ISSN: 1359-835X. DOI: 10.1016/J.COMPOSITESA.2016.08.020.

[88] *Mode II Delamination Test Results for Unidirectional and Multidirectional Carbon/Epoxy Composite Laminates Using End-Loaded Split (dataset)*. URL: https://data.4tu.nl/datasets/72b67fbb-dd92-41b0-8d16-bf7679df01b0/1.

[89] Rihab Messadi et al. *Mechanical cyclic tensile behavior of the flax/PP biocomposite Using DIC Technique*. Sept. 2022. DOI: 10.22541/au.166320183.30578414/v1.

A

CHADA TEMPLATES

CHADA

Characterization Data and description of a characterization experiment

Quasi-static mode I fracture toughness testing of aged & unaged samples

Used in *Hygrothermal effects on fracture toughness of flax fiber epoxy*

Template filled by: *Luca Baak*

Overview of the Characterization

1	**Specimen**	*Unidirectional DCB flax fiber (FlaxTape Ecotechnilin) reinforced with epoxy (SWANCOR 2511-1ALBL)*
2	**Chain of methods**	*Test method(s) used:* *1. Aging of samples following ASTM D5229* *2. Quasi-static loading to determine fracture toughness following ASTM D5528*
3	**Data publication**	*10.4121/ecc4e249-43b3-49c4-b9ba-8a430493fb0f*
4	**Access conditions**	*Data may be publicly shared*
5	**Workflow**	*The effect of hygrothermal aging on mode I quasi-static fracture toughness has been determined through the following experimental procedures. Specimens have been tested in the following conditions: unaged, after 1- and 2-aging cycles.* *Sample weight and thicknesses were measured initially and periodically to determine moisture absorption while aging. Samples were placed in climate chamber at 50C and 90% RH until reaching equilibrium after which conditions changed to 50C and 30% RH until reaching equilibrium. Finally, conditions are changed to 50C and 50% RH prior to testing and unaged samples are also placed in the climate chamber to ensure equal testing conditions. Some samples will undergo two aging cycles while others are tested after the first aging cycle.* *There were two rounds of testing to maintain similar lab conditions, while testing different aging conditions.*

1. Sample		
1.1	**Material**	*Flax fiber (FlaxTape Ecotechnilin) reinforced with Epoxy (SWANCOR 2511-1ALBL)*
1.2	**Specimen specifications and nomenclature**	*Specimen dimensions:* *W = 25 mm* *L = 210 mm* *T = 3.2-3.8 mm* *a_0 = 50 mm* *Specimen QS1-U-XXX (Quasi-static, mode I, unaged)* *Specimen QS1-A1-XXX (Quasi-static, mode I, 1 aging cycle)* *Specimen QS1-A2-XXX (Quasi-static, mode I, 2 aging cycle)*
1.3	**Manufacturing & preparation**	***Manufacturing:*** *1. Hand lay-up was used to create laminate plates.* *2. The laminate was vacuum-infused and cured at room temperature for at least 12 hours* *3. The plates were cured in the autoclave at 70 °C and 7 bar for 18 hours* *4. The plates were cut to final dimensions using a waterjet cutter.* ***Aging:*** *1. Aged samples were placed in climate chamber for one or two cycles at 50 degrees and then saturated at 90%RH, down to 30%RH and back up to 50%, with unaged samples being placed in the climate chamber at 50%RH to ensure equal conditions* ***After aging:*** *1. Both edges of the specimen were covered with white paint.* *2. Load blocks were bonded to the specimen* *3. One side of the specimen was marked with lines every 1 or 2 mm to be able to track crack growth.*
1.4	**Test environment**	*Room temperature – laboratory environment*

TU Delft

Specimen and manufacturing drawings

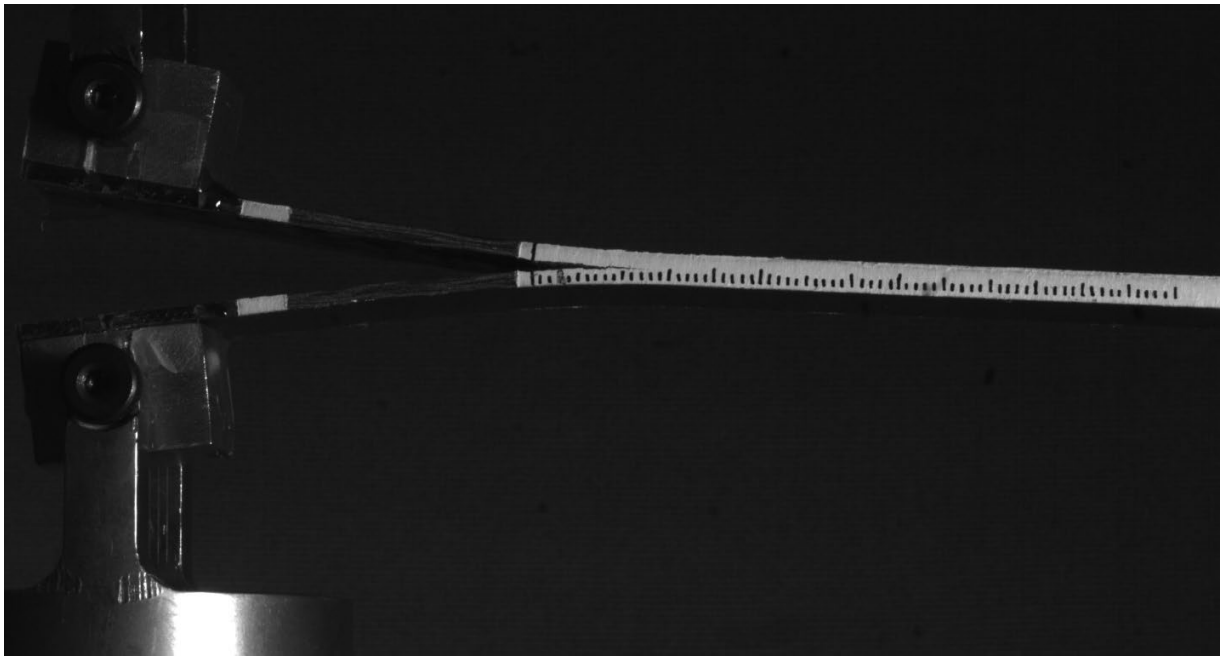

2. Method		
2.1	**Probe**	*Zwick 10 kN static test machine*
2.2	**Test set-up**	*1 kN loadcell, Digital camera, Spotlight*
2.3	**Signal**	*Force, displacement, images of crack length*
2.4	**Detectors**	*1. Zwick 10 kN machine crosshead displacement for displacement measurement* *2. 1 kN capacity load cell for force measurement* *3. Digital camera type Optomotive with 4 MP resolution for crack length measurements*
2.5	**Test procedure**	*Specimens widths and thicknesses were measured 50 mm from each end and in the middle. Insert crack length was measured. Test lab temperature and humidity were measured prior to each test.* *Camera was focussed on the crack front, with the spotlight providing extra light.* *Non-precracked specimens were first loaded quasi-statically under displacement control until crack growth was observed to be between 3-5 mm, specimen was then unloaded to zero force.* *Precracked testing was performed until crack had grown at least 50 mm from insert. Then unloaded to the original displacement position and force was noted.*
2.6	**Input parameters**	*Loading was conducted at 2 mm/min displacement rate – ASTM between 1-5 mm/min.* *Unloading was conducted at 10 mm/min displacement rate – ASTM up to 25 mm/min.* *Spotlight at 6% light output* *Camera picture interval every 5-10 seconds* *Load force max 100 N (setting to camera car)* *Displacement max 300 mm (setting to camera car)*

Test set-up images

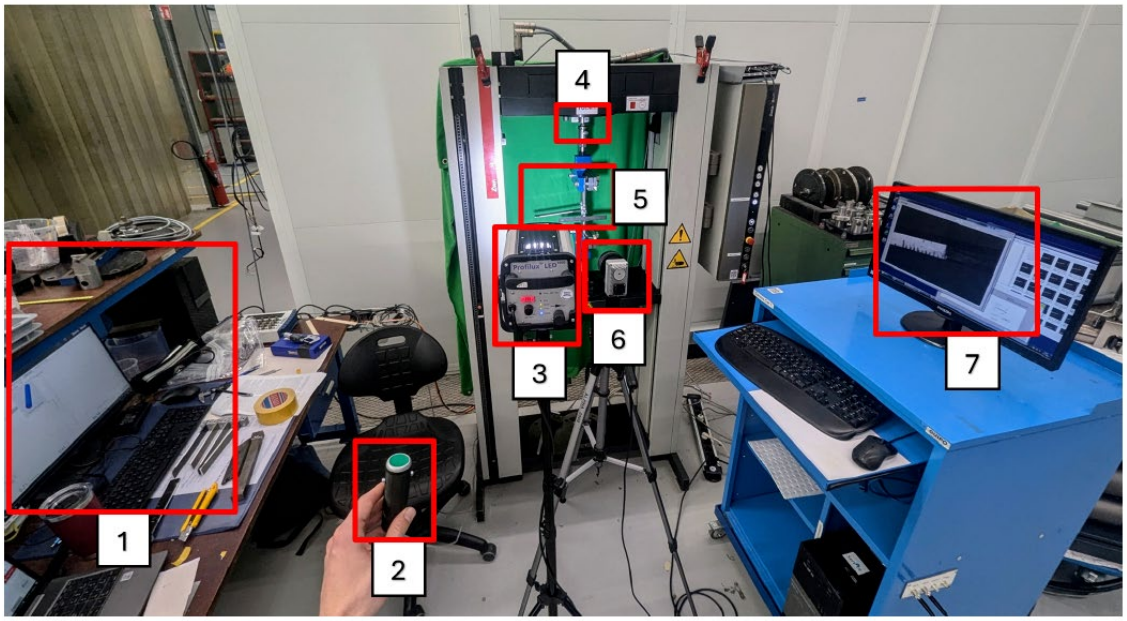

1. Test control
2. Trigger
3. LED lights
4. 1 kN load cell
5. DCB test specimen
6. Camera
7. Camera car computer

3. Raw Data		
3.1	**Raw Data**	*Displacement in mm and force in Newton are stored in the file named DataExport_DCB, Photographs are stored as .bmp files named SPECIMENID_yyyy_date_time.jpg, where yyyy corresponds to the image number.*
3.2	**Data acquisition rate**	*Force and displacement were recorded at a frequency of 10 Hz Photographs were taken every 5 seconds.*

4. Data Processing		
4.1	**Data filtering processes**	*Crack length is measured from the images at least once every 1 mm in the first 10 mm of propagation after which the length is measured at least once every 2 mm.* *Camera car was connected to the test bench capturing force displacement data for each image. These datapoints for each image were aligned and the data from the test bench (force and displacement) together with crack length was used in the analysis* *The force displacement data was aligned such that linear interpolation between the 25-75% linear portion of the curve originated in the origin.*
4.2	**Properties or relationships of interest**	*Fracture toughness (G_{Ic}) and (J_{Ic})*
4.2	**Data analysis procedures**	*Specimens exhibited significant plastic deformation, therefore both G_{Ic} and $J_{Ic.}$ For G_{Ic} the MCC method was used to calculate the fracture toughness values using correction factors for load blocks and large displacements. For J_{Ic} the angles of the load blocks were captured and the fracture toughness was calculated from (2P)/b * sin(theta/2) following: Joshua Gunderson. "Large Displacement J-Integral Double Cantilever Beam (DCB) Test Method for Mode I Fracture Toughness"* *The required angles were calculated using imageJ.*

CHADA

Characterization Data and description of a characterization experiment

Quasi-static mode II fracture toughness testing of aged & unaged samples

Used in *Hygrothermal effects on fracture toughness of flax fiber epoxy*

Template filled by: *Luca Baak*

Overview of the Characterization

1	**Specimen**	*Unidirectional ELS Flax fiber (FlaxTape Ecotechnilin) reinforced with Epoxy (SWANCOR 2511-1ALBL)*
2	**Chain of methods**	*Test method(s) used:* *1. Aging of samples following ASTM D5229* *2. Quasi-static loading to determine fracture toughness following ISO 15114*
3	**Data publication**	*10.4121/ecc4e249-43b3-49c4-b9ba-8a430493fb0f*
4	**Access conditions**	*Data may be publicly shared*
5	**Workflow**	*The effect of hygrothermal aging on mode I quasi-static fracture toughness has been determined through the following experimental procedures. Specimens have been tested in the following conditions: unaged, after 1- and 2-aging cycles.* *Sample weight and thicknesses were measured initially and periodically to determine moisture absorption while aging. Samples were placed in climate chamber at 50C and 90% RH until reaching equilibrium after which conditions changed to 50C and 30% RH until reaching equilibrium. Finally, conditions are changed to 50C and 50% RH prior to testing and unaged samples are also placed in the climate chamber to ensure equal testing conditions. Some samples will undergo two aging cycles while others are tested after the first aging cycle.* *There were two rounds of testing to maintain similar lab conditions, while testing different aging conditions.*

1. Sample		
1.1	**Material**	*Flax fiber (FlaxTape Ecotechnilin) reinforced with Epoxy (SWANCOR 2511-1ALBL)*
1.2	**Specimen specifications and nomenclature**	*Specimen dimensions:* *W = 25 mm* *L = 170 mm* *T = 4 mm* *a_0 = 50 mm* *Specimen QS2-U-XXX (Quasi-static, mode I, unaged)* *Specimen QS2-A1-XXX (Quasi-static, mode I, 1 aging cycle)* *Specimen QS2-A2-XXX (Quasi-static, mode I, 2 aging cycle)*
1.3	**Manufacturing & preparation**	***Manufacturing:*** *1. Hand lay-up was used to create laminate plates.* *2. The laminate was vacuum-infused and initially cured for at least 12 hours* *3. The plates were cured in the autoclave at 70 °C and 7 bar for 18 hours* *4. The plates were cut to final dimensions using a waterjet cutter.* ***Aging:*** *1. Aged samples were placed in climate chamber for one or two cycles at 50 degrees and then saturated at 90%RH, down to 30%RH and back up to 50%, with unaged samples being placed in the climate chamber at 50%RH to ensure equal conditions* ***After aging:*** *1. Both edges of the specimen were covered with white paint.* *2. Load blocks were bonded to the specimen using Loctite 3430* *3. One side of the specimen was marked with lines every 1 or 2 mm to be able to track crack growth. Another mark was made 7 mm from the clamp* *4. Specimens were precracked 3 mm by hand*
1.4	**Test environment**	*Room temperature – laboratory environment*

TU Delft

Specimen and manufacturing drawings

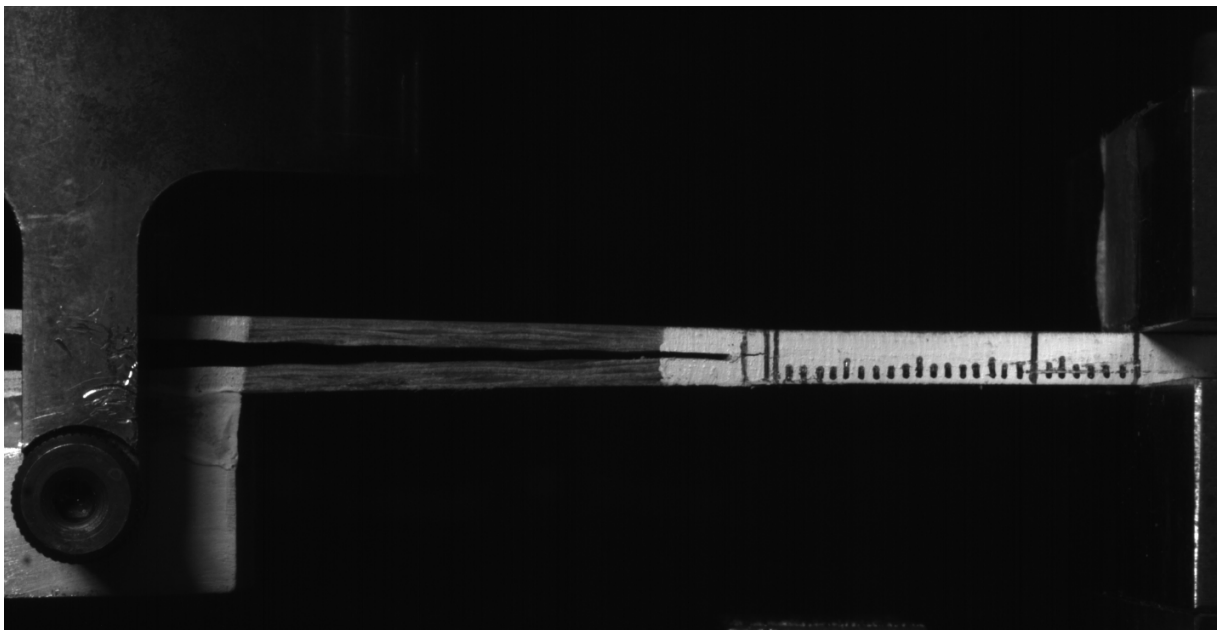

2. Method		
2.1	**Probe**	*MTS 10 kN fatigue testing machine*
2.2	**Test set-up**	*ELS test fixture & camera setup to record crack propagation*
2.3	**Signal**	*Force, displacement, crack length*
2.4	**Detectors**	*1. 10 kN MTS machine crosshead displacement for displacement measurement* *2. 1 kN capacity load cell for force measurement* *3. Digital camera type Optomotive with 4 MP resolution for crack length measurements*
2.5	**Test procedure**	*Prior to testing, samples were pre-cracked 2-5 mm by hand and specimen was loaded into the fixture applying a 5 Nm torque to the bolts . The fracture toughness test has been performed quasi-statically according to ISO 15114 at a loading rate of 1 mm/min until the crack is within 10 mm of the clamp, the specimen is unloaded at 5 mm/min. During the test the load, displacement was recorded continuously and periodical images are taken to record crack growth.*
2.6	**Input parameters**	*Quasi-static testing was conducted at 1 mm/min displacement load rate and 5 mm/min unloading rate.* *Maximum displacement of 60 mm* *Spotlight at 6%* *Camera picture interval every 5-10 seconds* *Bolts tightened 5 Nm using torque wrench* *Free-length at 75 mm to reduce required displacement to propagate crack*

Test set-up images

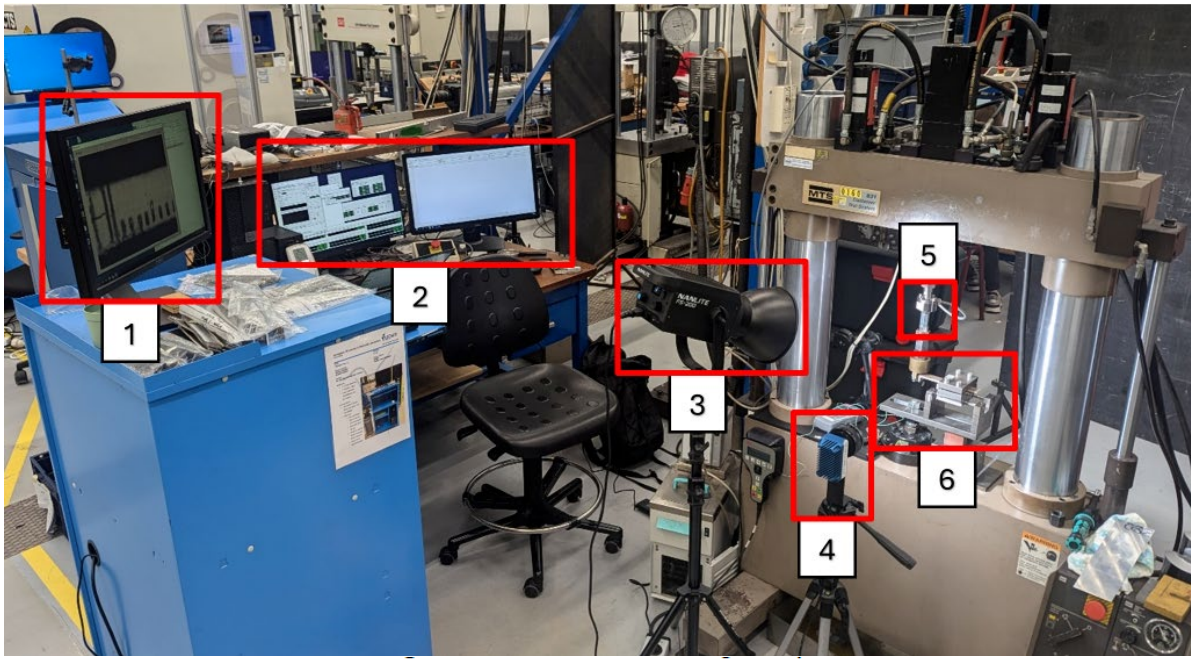

1. Camera car computer
2. Test control
3. LED light
4. Camera
5. 1 kN load cell
6. ELS fixture with specimen

3. Raw Data		
3.1	**Raw Data**	*Displacement in mm and force in Newton are stored in the files named specimens combined, with individual specimen data in each sheet of the excel named according to the specimen nomenclature, Photographs are stored as .jpg files named SPECIMENID_yyyy.jpg, where yyyy corresponds to the timestamp*
3.2	**Data acquisition rate**	*Displacement and force were recorded at a frequency of 20 Hz photographs for crack length measurements were acquired every 5-10 seconds*

4. Data Processing		
4.1	**Data filtering processes**	*Crack length is measured from the images at least once every 1 mm in the first 10 mm of propagation after which the length is measured at least once every 2 mm.* *Camera car was connected to the test bench capturing force displacement data for each image. These datapoints for each image were aligned and the data from the test bench (force and displacement) together with crack length was used in the analysis*
4.2	**Properties or relationships of interest**	*Fracture toughness (G_{IIc}) and (J_{IIc})*
4.2	**Data analysis procedures**	*Specimens exhibited significant plastic deformation, therefore both G_{IIc} and $J_{IIc.}$ GIC fracture toughness was calculated following ISO 15114 and using the ECM method, correcting for load block and large displacement. J_{IIc} was calculated following the procedure laid out in the paper below the table, applying the equation for large displacements. The strain at section S-S' was estimated using SBT as described in the paper. E11 and G12 were taken from test previous tests. The required angels were measured using image J.*

M. Pérez-Galmés et al. "A data reduction method based on the J-integral to obtain the interlaminar fracture toughness in a mode II end-loaded split (ELS) test". In: Composites Part A: Applied Science and Manufacturing 90 (Nov. 2016), pp. 670–677. ISSN: 1359-835X. DOI: 10.1016/J.COMPOSITESA.2016.08.020.

CHADA

Characterization Data and description of a characterization experiment

Fatigue mode I fracture toughness testing of aged & unaged samples

Used in *Hygrothermal effects on fracture toughness of flax fiber epoxy*

Template filled by: *Luca Baak*

Overview of the Characterization

1	**Specimen**	*Unidirectional DCB Flax fiber (FlaxTape Ecotechnilin) reinforced with Epoxy (SWANCOR 2511-1ALBL)*
2	**Chain of methods**	*Test method(s) used:*
		1. Aging of samples following ASTM D5229
		2 Fatigue loading to measure delamination growth
3	**Data publication**	*10.4121/ecc4e249-43b3-49c4-b9ba-8a430493fb0f*
4	**Access conditions**	*Data may be publicly shared*
5	**Workflow**	*The effect of hygrothermal aging on mode I, delamination growth resistance has been determined through the following experimental procedures. Specimens have been tested in the unaged condition and after 1 aging cycle.* *Sample weight and thicknesses were measured initially and periodically to determine moisture absorption while aging. Samples were placed in climate chamber at 50C and 90% RH until reaching equilibrium after which conditions changed to 50C and 30% RH until reaching equilibrium. Finally, conditions are changed to 50C and 50% RH prior to testing and unaged samples are also placed in the climate chamber to ensure equal testing conditions.*

1. Sample		
1.1	**Material**	*Flax fiber (FlaxTape Ecotechnilin) reinforced with Epoxy (SWANCOR 2511-1ALBL)*
1.2	**Specimen specifications and nomenclature**	*Specimen dimensions:* *W = 25 mm* *L = 210 mm* *T = 3.2-3.8 mm* *a_0 = 50 mm* *Specimen F1-U-XXX (Fatigue, mode I, unaged)* *Specimen F1-A1-XXX (Fatigue, mode I, 1 aging cycle)*
1.3	**Manufacturing & preparation**	***Manufacturing:*** *1. Hand lay-up was used to create laminate plates.* *2. The laminate was vacuum-infused and cured at room temperature for at least 12 hours* *3. The plates were cured in the autoclave at 70 ^{o}C and 7 bar for 18 hours* *4. The plates were cut to final dimensions using a waterjet cutter.* ***Aging:*** *1. Aged samples were placed in climate chamber for one or two cycles at 50 degrees and then saturated at 90%RH, down to 30%RH and back up to 50%, with unaged samples being placed in the climate chamber at 50%RH to ensure equal conditions* ***After aging:*** *1. Both edges of the specimen were covered with white paint.* *2. Load blocks were bonded to the specimen* *3. One side of the specimen was marked with lines every 1 or 2 mm to be able to track crack growth.*
1.4	**Test environment**	*Room temperature – laboratory environment*

2. Method		
2.1	**Probe**	*MTS 10 kN fatigue testing machine*
2.2	**Test set-up**	*500 N loadcell, Digital camera, Spotlight*
2.3	**Signal**	*Force, displacement, crack length*
2.4	**Detectors**	*1. MTS machine crosshead displacement for displacement measurement, 2. MTS machine 500 N capacity load cell for force measurement* *3. Digital camera type Optomotive with 4 MP resolution for crack length measurements*
2.5	**Test procedure**	*Specimens widths and thicknesses were measured 50 mm from each end and in the middle. Insert crack length was measured. Test lab temperature and humidity were measured prior to each test.* *Camera was focussed on the crack front, with the spotlight providing extra light.* *Then fatigue loading was applied under displacement control. Every 100 cycles the load was held at 0.8 times the maximum displacement and a picture was taken with the digital camera, after the first 10000 cycles images were captured every 1000 cycles. The fatigue cycle was continued for 200000 cycles*
2.6	**Input parameters**	*Fatigue testing was conducted at 5 Hz and R = 0.2* *Max displacement was 17 mm* *Min displacement was 3.4 mm* *Spotlight 6%* *Images captured at 0.8 max displacement every 100 cycles for the first 10000 cycles and every 1000 cycles thereafter.*

Test set-up images

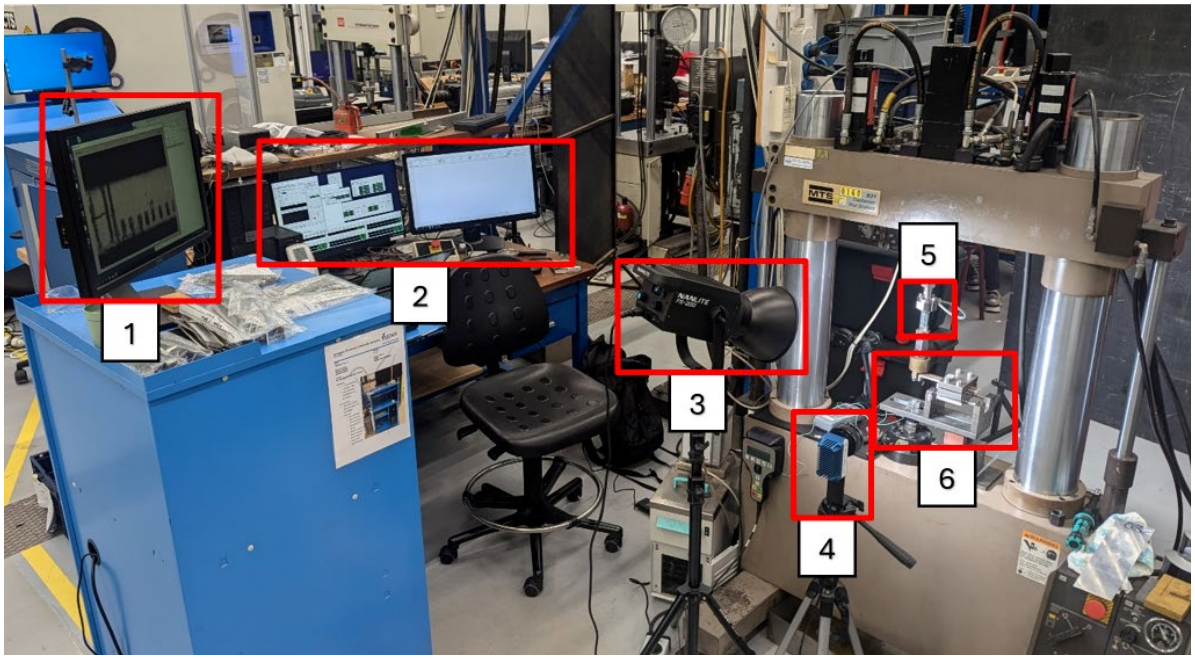

1. Camera car computer
2. Test control
3. LED light
4. Camera
5. 1 kN load cell
6. *Fixture replaced with Mode I setup

3. Raw Data		
3.1	**Raw Data**	*Displacement in mm, force in N, Count and Time in seconds are stored inside a folder (F1- U or A1 – Specimen nr.). Raw data is stored in file specimen.dat* *Photographs are stored as .jpg files named SPECIMENID_xx_yyyy.jpg, where xx and yyyy correspond to the image nr. and timestamp*
3.2	**Data acquisition rate**	*Maximum and minimum displacement and force were recorded every cycle, photographs for crack length measurements were acquired every 100 cycles for the first 10,000 cycles, and every 1,000 cycles thereafter*

4. Data Processing		
4.1	**Data filtering processes**	*The raw data, was filtered such that the minimum and maximum force displacement values were stored in an excel sheet for every 100 cycles in the first 10000 cycles and every 1000 cycles thereafter.*
4.2	**Properties or relationships of interest**	*Fracture toughness (G_{Ic} and J_{Ic}) and Relationship between crack growth rate (da/dN) and strain energy release rate range (G_{max} and J_{max})*
4.2	**Data analysis procedures**	*Specimens exhibited significant plastic deformation, therefore both G_{Ic} and $J_{Ic.}$ Crack growth and angles were measured for a subset of images, and the relative crack length and angles were determined using compliance. The mode I fracture toughness, GIc, was calculated using the Modified Compliance Calibration (MCC) method, with corrections applied for load block effects and large displacements. For JIc, the angle of the load blocks were measured from the obtained images using ImageJ, and fracture toughness was determined using the expression (2P)/b * sin(theta/2) following the methodology described by Joshua Gunderson in "Large Displacement J-Integral Double Cantilever Beam (DCB) Test Method for Mode I Fracture Toughness". The crack growth rate, da/dN, was obtained from the derivative of a power-law function fitted to the relationship between the number of cycles and relative crack length.*

TU Delft

CHADA

Characterization Data and description of a characterization experiment

Fatigue mode II fracture toughness testing of aged & unaged samples

Used in *Hygrothermal effects on fracture toughness of flax fiber epoxy*

Template filled by: *Luca Baak*

Overview of the Characterization

1	**Specimen**	*Unidirectional ELS Flax fiber (FlaxTape Ecotechnilin) reinforced with Epoxy (SWANCOR 2511-1ALBL)*
2	**Chain of methods**	*Test method(s) used:* *1. Aging of samples following ASTM D5229* *2 Fatigue loading to measure delamination growth*
3	**Data publication**	*10.4121/ecc4e249-43b3-49c4-b9ba-8a430493fb0f*
4	**Access conditions**	*Data may be publicly shared*
5	**Workflow**	*The effect of hygrothermal aging on mode II, delamination growth resistance has been determined through the following experimental procedures. Specimens have been tested in the unaged condition and after 1 aging cycle.* *Sample weight and thicknesses were measured initially and periodically to determine moisture absorption while aging. Samples were placed in climate chamber at 50C and 90% RH until reaching equilibrium after which conditions changed to 50C and 30% RH until reaching equilibrium. Finally, conditions are changed to 50C and 50% RH prior to testing and unaged samples are also placed in the climate chamber to ensure equal testing conditions.*

1. Sample		
1.1	**Material**	*Flax fiber (FlaxTape Ecotechnilin) reinforced with Epoxy (SWANCOR 2511-1ALBL)*
1.2	**Specimen specifications and nomenclature**	*Specimen dimensions:* *W = 25 mm* *L = 170 mm* *T = 3.2-3.8 mm* *a_0 = 50 mm* *Specimen F2-U-XXX (Fatigue, mode II, unaged)* *Specimen F2-A1-XXX (Fatigue, mode II, 1 aging cycle)*
1.3	**Manufacturing & preparation**	***Manufacturing:*** *1. Hand lay-up was used to create laminate plates.* *2. The laminate was vacuum-infused and cured at room temperature for at least 12 hours* *3. The plates were cured in the autoclave at 70 °C and 7 bar for 18 hours* *4. The plates were cut to final dimensions using a waterjet cutter.* ***Aging:*** *1. Aged samples were placed in climate chamber for one or two cycles at 50 degrees and then saturated at 90%RH, down to 30%RH and back up to 50%, with unaged samples being placed in the climate chamber at 50%RH to ensure equal conditions* ***After aging:*** *1. Both edges of the specimen were covered with white paint.* *2. Load blocks were bonded to the specimen using Loctite 3430* *3. One side of the specimen was marked with lines every 1 or 2 mm to be able to track crack growth. Another mark was made 7 mm from the clamp* *4. Specimens were precracked 3 mm by hand*
1.4	**Test environment**	*Room temperature – laboratory environment*

TU Delft

Specimen and manufacturing drawings

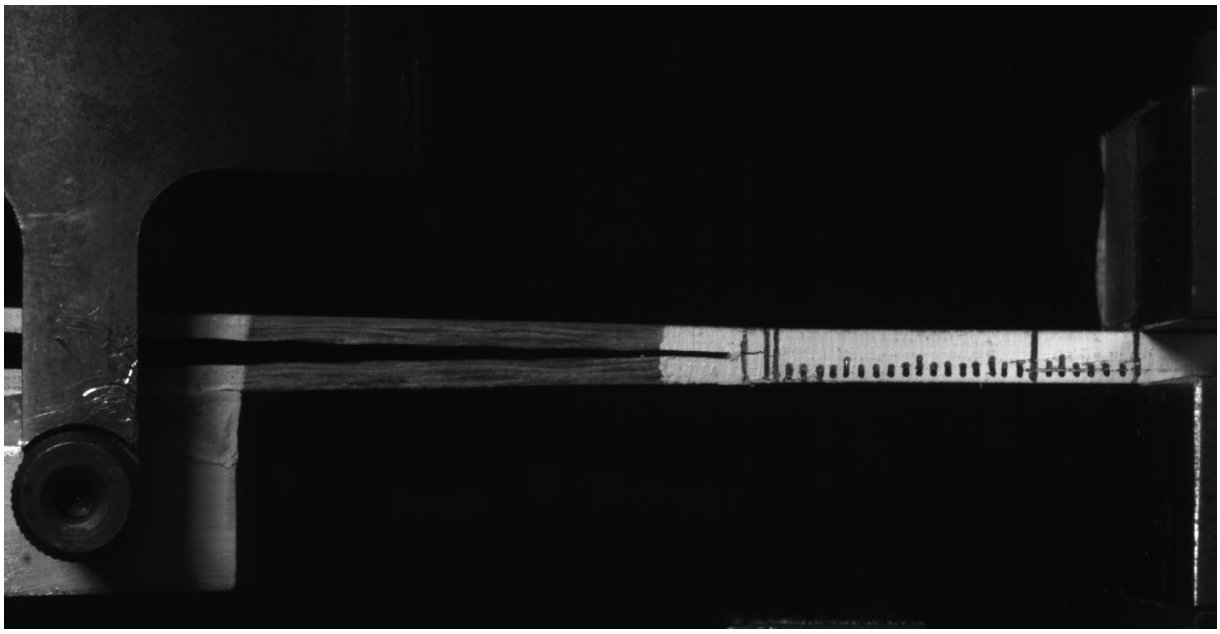

2. Method		
2.1	**Probe**	*MTS 10 kN fatigue testing machine*
2.2	**Test set-up**	*ELS test fixture & camera setup to record crack propagation*
2.3	**Signal**	*Force, displacement, crack length*
2.4	**Detectors**	*1. 10 kN MTS machine crosshead displacement for displacement measurement* *2. 1 kN capacity load cell for force measurement* *3. Digital camera type Optomotive with 4 MP resolution for crack length measurements*
2.5	**Test procedure**	*Prior to testing, samples were pre-cracked 2-5 mm by hand. Specimens widths and thicknesses were measured 50 mm from each end and in the middle. Insert crack length was measured. Test lab temperature and humidity were measured prior to each test. Specimen was loaded into the fixture applying a 5Nm torque to the bolts* *Camera was focussed on the crack front, with the spotlight providing extra light.* *Then fatigue loading was applied under displacement control. Every 100 cycles the load was held at 0.8 times the maximum displacement and a picture was taken with the digital camera, after the first 10000 cycles images were captured every 1000 cycles. The fatigue cycle was continued for 200000 cycles*
2.6	**Input parameters**	*Fatigue testing was conducted at 3 Hz and R = 0.2* *Max displacement was 21 mm* *Min displacement was 4.2 mm* *Spotlight 6%* *Free-length 75 mm to reduce required displacement to propagate crack* *Bolts tightened 5 Nm using torque wrench* *Images captured at 0.8 max displacement every 100 cycles for the first 10000 cycles and every 1000 cycles thereafter.*

Test set-up images

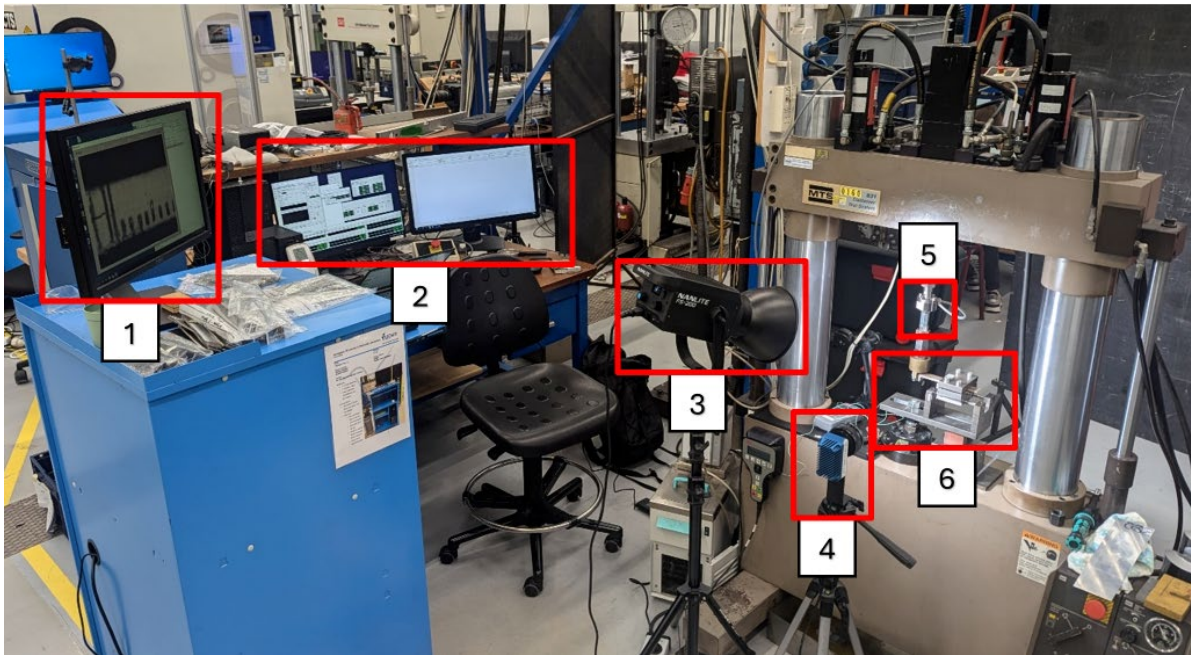

1. Camera car computer
2. Test control
3. LED light
4. Camera
5. 1 kN load cell
6. ELS fixture with specimen

3. Raw Data		
3.1	**Raw Data**	*Displacement in mm, force in N, Count and Time in seconds are stored inside a folder (F2- U or A1 – Specimen nr.). Raw data is stored in file specimen.dat* *Photographs are stored as .jpg files named SPECIMENID_xx_yyyy.jpg, where xx and yyyy correspond to the image nr. and timestamp*
3.2	**Data acquisition rate**	*Maximum and minimum displacement and force were recorded every cycle, photographs for crack length measurements were acquired every 100 cycles for the first 10,000 cycles, and every 1,000 cycles thereafter*

4. Data Processing		
4.1	**Data filtering processes**	*The raw data, was filtered such that the minimum and maximum force displacement values were stored in an excel sheet for every 100 cycles in the first 10000 cycles and every 1000 cycles thereafter.*
4.2	**Properties or relationships of interest**	*Fracture toughness (G_{IIc} and J_{IIc}) and Relationship between crack growth rate (da/dN) and strain energy release rate range (G_{max} and J_{max})*
4.2	**Data analysis procedures**	*Specimens exhibited significant plastic deformation, therefore both G_{IIc} and $J_{IIc.}$ Crack growth and angles were measured for a subset of images, and the relative crack length and angles were determined using compliance. The mode II fracture toughness, G_{IIc}, was calculated using the ECM method, with corrections applied for load block effects and large displacements. For J_{IIc}, the angle of the load blocks were measured from the obtained images using ImageJ, and fracture toughness was calculated following the procedure laid out in the paper below the table, applying the equation for large displacements. The crack growth rate, da/dN, was obtained from the derivative of a power-law function fitted to the relationship between the number of cycles and relative crack length.*

M. Pérez-Galmés et al. "A data reduction method based on the J-integral to obtain the interlaminar fracture toughness in a mode II end-loaded split (ELS) test". In: Composites Part A: Applied Science and Manufacturing 90 (Nov. 2016), pp. 670–677. ISSN: 1359-835X. DOI: 10.1016/J. COMPOSITESA.2016.08.020.